Patient-Specific Cerebral Vessel Segmentation with Application in Hemodynamic Simulation

Patientenindividuelle zerebrale Gefäßsegmentierung mit Anwendung in der Blutflusssimulation

Der Technischen Fakultät der
Universität Erlangen-Nürnberg

zur Erlangung des Grades

DOKTOR-INGENIEUR

vorgelegt von

Martin Spiegel

Erlangen — 2011

Als Dissertation genehmigt von der
Technischen Fakultät der
Universität Erlangen-Nürnberg

Tag der Einreichung:	02.05.2011
Tag der Promotion:	04.07.2011
Dekan:	Prof. Dr.-Ing. R. German
Berichterstatter:	Prof. Dr.-Ing. J. Hornegger
	Prof. Dr. rer. nat. C. Pflaum

Abstract

Cerebral 3-D rotational angiography has become the state-of-the-art imaging modality in modern angio suites for diagnosis and treatment planning of cerebrovascular diseases, e. g. intracranial aneurysms. Among other reasons, it is believed that the incidence of aneurysms is due to the local prevalent hemodynamic pattern. To study such a hemodynamic behavior, the 3-D vessel geometry has to be extracted from 3-D DSA data. Since 3-D DSA data may be influenced by beam hardening, inhomogeneous contrast agent distribution, patient movement or the applied reconstruction kernel, this thesis describes a novel vessel segmentation framework seamlessly combining 2-D and 3-D vessel information to overcome the aforementioned factors of influence. The main purpose of this framework is to validate 3-D segmentation results based on 2-D information and to increase the accuracy of 3-D vessel geometries by incorporating additional 2-D vessel information into the 3-D segmentation process. Three major algorithmic contributions are given within this framework: (1) a classification-based summation algorithm of 2-D DSA series such that 2-D vessel segmentation becomes feasible, (2) a 3-D ellipsoid-based vessel segmentation method which allows for local adaptations driven by 2-D vessel segmentations and (3) a mesh size evaluation study investigating the influence of different mesh type elements and resolutions w. r. t. hemodynamic simulation results. Moreover, this work is chamfered by a simulation study which evaluates the impact of different vessel geometries on the simulation result. The vessel geometries are computed by different segmentation techniques working on the same patient dataset. The evaluation of each framework component revealed high accuracy and algorithmic stability to be applied in a clinical environment.

Kurzübersicht

Zerebrale 3-D Rotationsangiographie ist seit einigen Jahren eine anerkannte Bildgebungsmodalität, die in modernen Neuroradiologieabteilungen zur Diagnose und Therapieplanung von zerebralen Gefäßerkrankungen, wie zum Beispiel von intrakraniellen Aneurysmen, bevorzugt eingesetzt wird. Neben vielen anderen Gründen, nimmt man an, dass die Ursache für das Auftreten von Aneurysmen mit den lokal vorherrschenden Druck- und Flussmustern zusammenhängt. Um solche Flussmuster virtuell simulieren und untersuchen zu können, muss die entsprechende 3-D Gefäßgeometrie aus dem 3-D DSA Datensatz so genau wie möglich extrahiert werden. Dabei kann die Qualität von 3-D DSA Datensätzen von unterschiedlichen Faktoren (Aufhärtungsartefakte, heterogene Kontrastmittelverteilung, Patientenbewegung, Rekonstruktionskern) beeinträchtigt sein, was eine exakte 3-D Segmentierung der Gefäße erschwert. Diese Arbeit beschreibt ein neues System zur Gefäßsegmentierung, das 2-D und 3-D Gefäßdaten geschickt miteinander kombiniert, um den Einfluss der vorher genannten Faktoren zu minimieren. Der Hauptzweck dieses Systems besteht darin, 3-D Segmentierungsergebnisse anhand von 2-D DSA Daten zu validieren sowie die Genauigkeit von 3-D Gefäßgeometrien mittels zusätzlicher Einbindung von 2-D Gefäßinformation im 3-D Segmentierungsprozess zu erhöhen. Der wissenschaftliche Beitrag dieses Systems ist dabei dreigeteilt: (1) ein klassifikationsbasierender Algorithmus zur Aufsummierung von DSA Serien, wodurch eine einfache 2-D Gefäßsegmentierung durchführbar wird; (2) eine 3-D Gefäßsegmentierung basierend auf ineinander gesteckter Ellipsoiden, die eine lokale Anpassung aufgrund von 2-D Segmentierungen erlaubt und (3) eine Bewertungsstudie zur Netzunabhängigkeitsanalyse, die den Einfluss von unterschiedlichen Netzgrößen und Typen auf die Blutflusssimulationsergebnisse untersucht. Eine Simulationsstudie, die die Auswirkungen von unterschiedlichen Gefäßsegmentierungen auf das Simulationsergebnis zeigt, rundet die Arbeit ab. Die Segmentierungen basieren dabei auf den gleichen Datensätzen. Jede Komponente des Segmentierungssystems wurde ausgiebig evaluiert und getestet, damit eine hohe Genauigkeit sowie algorithmische Stabilität für einen Klinikeinsatz gewährleistet sind.

Acknowledgment

To successfully accomplish a Ph.D. project, four things are required: great ideas, discipline, endurance and a creative working environment. This page is dedicated to the people who supported my work and made this creative working environment possible.

First of all, I would like to thank Prof. Dr.-Ing. Joachim Hornegger for his enduring support, trust and all the fruitful discussions since my student thesis at his lab. He gave me the excellent opportunity to take part and contribute in a demanding and challenging research field and to develop myself.

I am very grateful to Prof. Dr. med. Arnd Dörfler for co-supervising my thesis, sharing his medical expertise, his great support and his willingness to consider myself as a team member at the Department of Neuroradiology Erlangen.

Many thanks go to Dr. Thomas Redel (Siemens AG, Healthcare Sector, AX Forchheim) who enthusiastically supported this work with helpful comments and critical proof-reading. I also wish to thank Dr. med. Tobias Struffert who qualitatively evaluated my results from the perspective of a physician and gave me a close insight into medical workflows. Prof. Dr. rer. nat. Christoph Pflaum thank you for reviewing my work.

I enjoyed my time with Dr. Christof Karmonik who provided me the opportunity to stay in Houston, TX, USA at the Methodist Hospital Research Institute and taught me in performing blood flow simulation experiments. My special thanks go to my fellow colleagues at the Pattern Recognition Lab particularly with regard to Eva Kollorz, Sebastian Bauer, Benjamin Keck, Christopher Rohkohl and Christian Riess. I want to thank my students for their work - especially Dominik Schuldhaus and Thomas Kluge for writing our publications.

Last but not least, I am very grateful to my girlfriend Bettina. Thank you so much for your encouragement and patience over the last four years.

Erlangen, 2. May 2011 Martin Spiegel

Contents

CHAPTER 1

Introduction

The human brain is one of the most complex systems in nature coordinating all physical motions and being the origin of all our ideas, thoughts, fantasy and creativity. To keep this system running, it diligently needs oxygen and sugar such that the cells stay alive. This is provided via the cerebral arterial vessel system carrying oxygenated blood to the brain cells. The human brain is nurished by vessel branches forming a complex vessel tree. Cerebrovascular disease, specifically a sudden interruption of cerebral blood flow imply serious danger for human life usually necessitating further clinical clarification and if necessary an intervention. Three different imaging devices are available to work-up such a clinical event in vivo, e. g. computed tomography (CT), X-ray based 3-D rotational angiography (3-D DSA) and magnetic resonance imaging (MRI), respectively. Each of these image modalities has its specific indication. Patients with an acute cerebrovascular event are usually undergoing cross-sectional imaging of the brain, i. e. first a CT or a MRI, in selected cases followed by subsequent conventional angiography using DSA. If available, MRI is preferred and most often used for routine clarifications or as follow up examination because it is free of radiation.

This thesis deals with the segmentation of cerebral vessels in 2-D and 3-D angiographic images and its subsequent blood flow simulation. X-ray based 2-D and 3-D angiography images denote the image modality on which the methods of this thesis are working on. The purpose of this introduction is to shortly make its readers familiar with the medical background and the characteristics of the applied imaging modality.

The outline is as follows: First, an overview about major cerebral vessels together with cerebrovascular pathologies and endovascular therapeutic options, respectively. Second, 2-D and 3-D angiography is introduced and the challenges are described making accurate 3-D vessel segmentation a difficult task. The third part details the hemodynamic simulation workflow which denotes one future post-

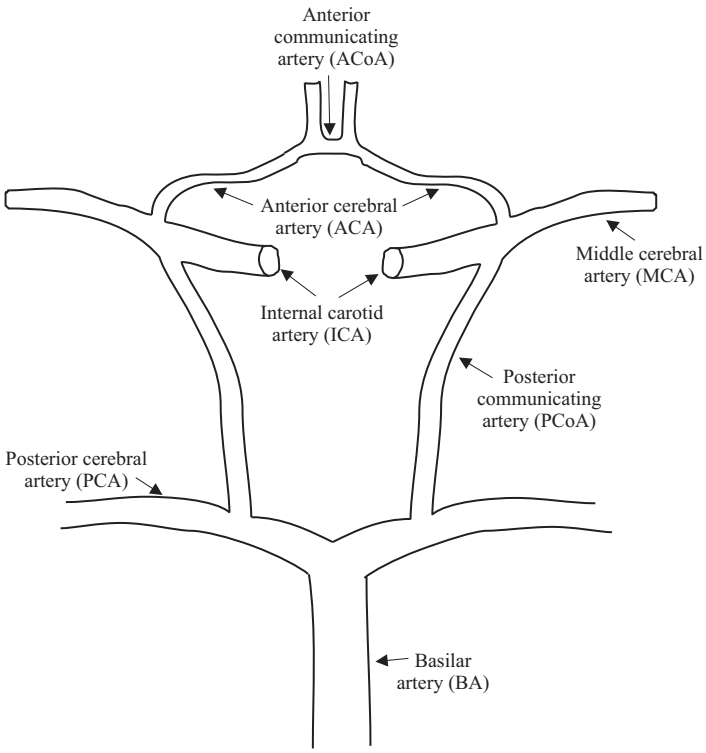

Figure 1.1: Schematic illustration of the circle of Willis together with its major cerebral vessel branches.

processing application of 3-D vessel segmentation results based on 3-D angiography. The introduction concludes with the scientific focus and the outline of this thesis.

1.1 Cerebrovascular Anatomy, Pathology and Interventional Therapy

The Circle of Willis comprises the major hub within the human cerebrovascular system [Osbo 99] as depicted in Figure 1.1. It is the connection between both anterior circulations and concatenates to the vertebral-basilar system. The major artery of the circle of Willis denotes the left and right internal carotid artery (ICA) which branches to the corresponding left and right anterior cerebral arteries (ACA). Both ACAs are connected by the anterior communicating artery (ACoA). The circle is closed by the posterior circulation exhibiting the posterior communicating arteries (PCoA) which connect to the posterior cerebral artery (PCA). The middle cerebral arteries (MCA) and the basilar artery (BA) are not part of the circle of Willis, however, they provide a major contribution of the blood supply of the human brain.

In general, there are several cerebrovascular diseases which lead to serious pathologies of the vessels, e. g. intracranial aneurysms, stenoses, and arteriovenous malformations. Intracranial aneurysms are balloon-like bulges of vessels which are categorized according to (a) saccular aneurysms, (b) fusiform aneurysms

Table 1.1: DSA acquisition protocols for 2-D DSA series and 3-D DSA performed on Artis dBA system (Siemens AG, Healthcare Sector, Forchheim, Germany).

DSA protocol	Contrast agent [ml]	Injection [ml/sec]	Frame rate [1/sec]	Scan time [sec.]	Image size [pixels]	Pixel size [mm]
2-D DSA	5-6	5	0.5-2	≤ 25	512×512-1440×1440	0.154
3-D DSA	15-20	3.5-4	26.6	5	1240×960	0.321

and (c) dissecting aneurysms. A stenosis denotes an abnormal narrowing of a vessel and an arteriovenous malformation describes a pathologic connection between veins and arteries. The focus of this work is on intracranial aneurysm.

Cerebral aneurysms may arise at any location within the cerebrovascular system. There are locations, however, which show a higher prevalence like the Circle of Willis [Osbo 99]. The anterior circulation exhibits approximately 90% of all aneurysms whereas the vertebrobasilar system indicates only 10%. 30% of aneurysms occur at the ACoA and the PCA. 20% rise at the MCA bi- or trifurcation. Among other reasons like drug abuse or infection, it is assumed that the etiology of aneurysms is flow-related with high probability.

Most of these aneurysms, however, are accidently detected during MRI examinations if patients show up in the clinic with specific symptoms. A much more critical event denotes the rupture of an aneurysm implying a subarachnoid hemorrhage (SAH) which immediately requires a clinical clarification and especially therapeutic intervention if possible. Annually, about 28,000 intracranial aneurysms rupture in North America and 8% of these patients die before reaching the hospital [Atla 09]. There are two different types of therapies available to handle such an event, i. e. the clipping approach and the endovascular procedure, also called coiling. The therapy type is chosen depending on the aneurysm shape, location and local institutional factors such as physician availability.

Within the past, the clipping approach was considered as the standard treatment where neurosurgeons open the skull of the patient and approach the aneurysm directly. The blood flow into the aneurysm sac is interrupted by the placement of a small clip across the aneurysm neck. Although this approach is highly effective, it implies a risk for patients morbidity and mortality.

Modern imaging devices allow endovascular procedure using guide wires to prevent blood flow into the aneurysm [Wank 02, Doer 06]. A micro catheter is used for the coiling procedure which is placed inside the patient's arterial system for both diagnosis and treatment. Again, the positioning of the micro catheter all the way up through the vessel system and inside the aneurysm is done by guide wires. After the approach, tiny helical-shaped platinum coils are passed through the micro catheter into the aneurysm to fill and effectively seal it off. The entire procedure is guided by X-ray imaging. This procedure significantly reduces the number of complications, shortens the time for therapy and accelerated convalescence. That is why it is nowadays considered as the state-of-the-art treatment

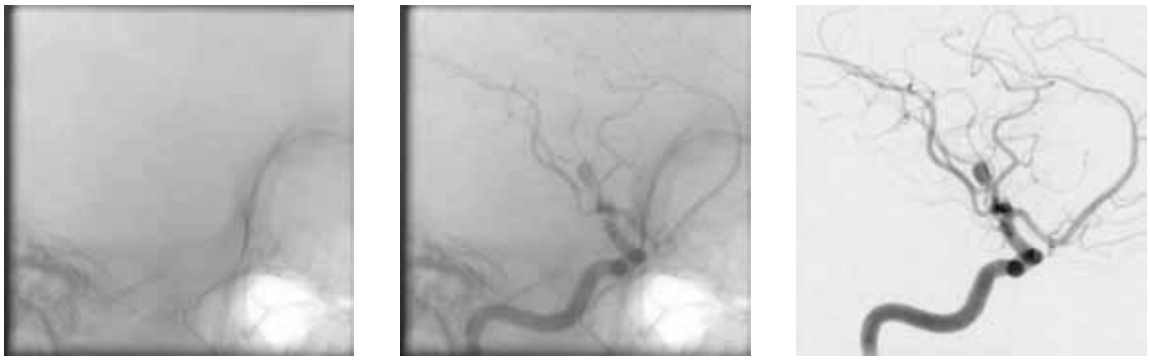

(a) Mask image (b) Contrast image (c) DSA image

Figure 1.2: Example of digital subtraction angiography: (a) mask image, (b) contrast filled image and (c) DSA image.

method.
Concerning endovascular procedures, 2-D and 3-D angiography represent the essential imaging technique to plan and perform this kind of interventional therapies. Within the next two sections, this imaging modality is shortly described together with its challenges when performing accurate vessel segmentation.

1.2 2-D Angiography

X-ray based 2-D angiography was first described in 1935 by Ziedses des Plantes [Plan 35] which is an approach to visualize vessel structures on X-ray images using intravascular contrast agent. The contrast agent is an iodine fluid with a higher density than blood. Once injected into the arterial system, vessels are visible on X-ray images due to its increased absorption rate.

This is especially utilized by subtraction angiography for objects which do not move during the acquisition. The basic principle relies on three steps, i. e. (1) a mask image is acquired depicting the region of interest for the examination, (2) contrast agent is injected through a catheter making the vessels visible within X-ray images and (3) the mask image is subsequently subtracted from the contrasted images such that only the vessels remain on the image while the background is removed. Figure 1.2 gives a qualitative insight how this method works and Table 1.1 (first row) shows typical acquisition protocol parameters. This provides the fundamental basis for a variety of therapies particulary within the field of interventional procedures would not be imaginable. At the beginning, the performance of this method was very time consuming since all X-ray images were saved on films and its processing was slow. The advent of computers simplified the computation of this method a lot by using digital subtraction angiography (DSA) [Krug 78]. Besides CT and MRI, 2-D angiography is one of the most important modalities particularly within interventional laboratories.

Nowadays, 2-D DSA images are acquired using C-arm systems where the angulation of the C-arm is kept fixed while performing the 2-D DSA series. C-arm systems are especially designed to support interventional procedures, e. g.

Figure 1.3: Modern C-arm system at the Department of Neuroradiology (University Hospital Erlangen, Germany) Siemens AXIOM Artis, Forchheim, Germany.

minimal invasive treatments like coil embolization. The X-ray tube and detector are mounted on a mechanical C-arm allowing the acquisition of X-ray images from various directions (see Figure 1.3). Within the last two decades, substantial progress has been made concerning both hardware and software, e. g. image intensifier are more and more replaced by flat-panel detectors [Vano 05], various types of algorithms have been implemented to perform motion correction, image enhancement etc. [Meij 99a, Meij 99b, Bent 02].
Modern C-arm systems like Siemens AXIOM Artis deliver such 2-D X-ray images in real-time with a spatial resolution of up to 0.25 mm [Brun 05]. This allows to visualize vessel structures in a very high quality with clear vessel contours. Due to the sharp vessel boundaries, these 2-D images are used to measure vessel diameters, neck size of aneurysms or to determine the degree of a stenosis. These are the reasons why 2-D DSA is still considered as „gold standard“ image modality [Brin 09] if it comes to treatment planning and therapy performance concerning cerebral vessel pathologies.

1.3 C-arm CT and 3-D Rotational Angiography

Since the early seventies, 3-D imaging has been known within the medical community due to the invention of computed tomography (CT) [Buzu 02, Kale 06]. CT captures a set of X-ray projection images around the object which are used to reconstruct a 3-D volume. It took over 25 years, however, until 3-D imaging has found its way into interventional rooms. Comparable to CT, the C-arm rotates around the patient acquiring projection images from various directions to compute a 3-D volume using cone-beam reconstruction algorithms [Hopp 09]. This interventional CT is also called C-arm CT which was first described by [Roug 93, Sain 94, Kopp 95].

Its first application was found for cerebrovascular imaging where the C-arm performs two rotations around the patient. X-ray projections are captured at predefined positions during both rotations. The first run differs from the second one in using contrast agent to make vessels on X-ray images visible as depicted in Figure 1.4 (a). The corresponding projections of both runs are subtracted from each other such that the irrelevant background structures are removed. The reconstructed data clearly visualizes the cerebral vessel tree of the human brain as depicted in Figure 1.4 (b). Table 1.1 (second row) details the parameters of the typical acquisition protocol used. This image modality is called 3-D rotational angiography and denotes a major breakthrough within the field of neuroradiology concerning diagnosis and treatment of vascular pathologies, e. g. cerebral aneurysm.

The tremendous improvement of the image quality and the availability of such 3-D information during interventions have prepared the ground for many other clinical applications. C-arm CT delivers indispensable information for abdominal applications like liver lesion treatment. Motion compensated cardiac C-arm CT allows to reconstruct the beating heart providing accurate morphological information before, during and after an interventional suite [Rohk 09, Rohk 10b]. Traditionally, catheter guidance was restricted to 2-D X-ray fluoroscopic images. C-arm CT upgrades this guidance by 3-D information being integrated into 2-D images. Further information can be found in [Stro 09].

The acquisiton time requires some seconds depending on the protocol and due to the low rotation speed of the C-arm. This is rather slow compared to a modern CT scanner. This, however, is more than compensated by the spatial resolution a C-arm CT offers, i. e. regular CT reconstructed volume exhibits an isotropic resolution of up to 0.5 mm whereas a C-arm CT volume typically has a resolution of 0.1 mm [Brun 05]. C-arm CT has the advantage against CT that it is able to preserve small anatomical structures like cochlear implant electrode at petrosal bones [Stru 10] or vessel morphologies in much more detail due to bone removal and intra-arterial contrast agent injection. Moreover, C-arm CT and cerebral blood volume imaging with intravenous contrast medium compares favorably with multislice perfusion CT such that the assessment of cerebral perfusion within the angiographic suite may improve the management of ischaemic stroke [Stru 11].

That is the reason why 3-D DSA modality are the preferred image volumes when it comes to cerebral vessel segmentation. 3-D DSA volumes, however, are subject to certain ambiguities in determining the exact position of the vessel bound-

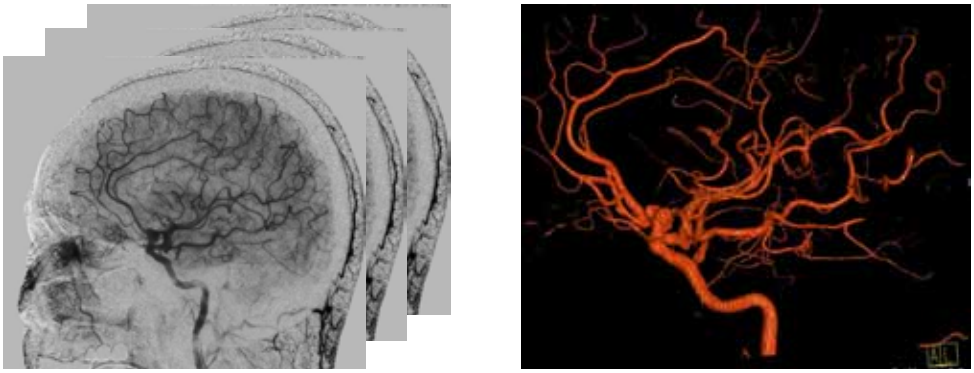

(a) 2-D DSA projections (b) Reconstructed vessel tree

Figure 1.4: Figure (a) shows a 3-D DSA volume and (b) the corresponding X-ray projections used for reconstruction.

aries. This circumstance is caused by the factors of influence which characterize the acquisition of a 3-D DSA volume, i. e. the amount of injected contrast agent, injection timing, patient movement, vessel movement and the applied reconstruction algorithm with its kernel. That makes accurate 3-D vessel segmentation to come up with quantitative measurements like diameter or aneurysm neck size a challenging task because the vessel boundary exhibit a wide edge ramp such that the exact position of the vessel boundary is not well-defined.

The focus of this thesis is on the development of a 3-D vessel segmentation approach which is able to correctly determine the exact vessel boundary position by incorporating corresponding 2-D DSA vessel information. As mentioned within Section 1.2, 2-D DSA images offer a higher spatial resolution together with a clearer position of the vessel boundary. The 2-D driven 3-D segmentation result is then used to perform quantitative vessel measurements and to compute cerebral hemodynamic simulations describing one future post-processing application of 3-D DSA.

1.4 Hemodynamic Simulation and Factors of Influence

Hemodynamic simulation describes the forces and physical measurements associated with blood flow and circulation. It is assumed that hemodynamic effects such as flow separation, certain circulation patterns or wall shear stress play a major role in the development of cerebral aneurysms. Hence, the simulation of such gains important information concerning a better understanding and treatment of these vessel pathologies. The following enumeration gives a brief insight into the constraints of such simulations describing influencing factors which illustrate its diverse complexity. These factors can be categorized according to dedicated steps within a common simulation workflow as illustrated in Figure 1.5.

1. The acquisition of vessel morphologies marks the base before one can even think about hemodynamic simulations. Within this thesis, 3-D DSA volumes are used to deliver cerebral vascular datasets because 3-D DSA offers the

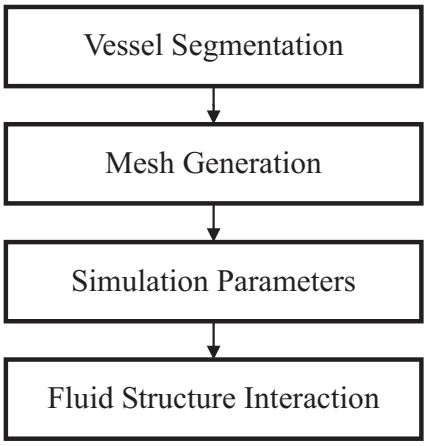

Figure 1.5: Four factors having a substantial influence on the result of hemodynamic simulations.

highest spatial resolution such that even small vessel structures are visible. Several segmentation techniques are available to extract the vessel tree. The segmentation results depend on the applied segmentation method because of deviating vessel boundary determination. Hence, different vessel segmentation results lead to different vessel geometries which heavily influences the simulation results.

2. The conversion of a voxel-based vessel segmentation result into a surface representation denotes the second step. This surface is usually created by a set of triangles. The number and size of these triangles decide about the accuracy of the surface approximation. Hence, regions with high curvature need higher triangle mesh density to accurately model such areas. The interior of the vessel geometry also requires a proper approximation which can be done by either tetrahedral or polyhedral elements. The decision about the final number of surface triangles and tetrahedral/polyhedral elements is crucial concerning the simulation result.

3. The third step represents the simulation parameters which steer the simulation process. Blood denotes one parameter which is a complex composition of fluid and solid components [Gano 01], i. e. blood plasma represents the major fluid medium whereas several kinds of cells (erythrocytes, leukocytes and thrombocytes) are solid particles. Velocity inflow curves describe the oscillating blood flow which can be either measured using MRI time-of-flight imaging [Karm 08] or Doppler ultrasound [Fitz 82]. This flow curve has a strong impact on the resulting flow pattern, pressure and wall shear stress distributions. The blood modeling complexity is usually reduced by representing blood as a Newtonian fluid specified by two parameters, i. e. density and viscosity.

4. The last step within this simulation workflow denotes fluid structure interaction. The human heart mechanically pumps the blood through the vascular system inducing an oscillatory blood flow. This oscillation leads to an inter-

action between the moving blood and the vessel wall resulting in a certain coupling. The vessel wall itself is a living tissue able to grow or re-model depending on external stimulations. This interaction is called fluid structure interaction and, hence, has to be properly modeled within an ideal simulation case.

All steps together make hemodynamic simulation one of the most complex simulation challenges because most of the constraints remain unknown and only a few can be measured in vivo - not to forget the challenges which are behind the implementation of such a solver.

The scientific direction of hemodynamic simulations within this thesis is explicitly on vessel geometry related issues, i. e. the first and second step. An evaluation has been performed regarding the influence of small vessel geometry changes on the simulation result due to different segmentation techniques. Furthermore, the usage of varying mesh sizes with different mesh elements has shed light on the impact on the simulation. All simulation experiments were conducted using Gambit and Fluent (ANSYS Inc.)[1] as meshing and simulation software.

1.5 Scientific Focus and Contributions

The previous sections have introduced the framework in which this thesis is embedded. In summary, the scientific focus of this thesis lies especially in the development of a novel 3-D DSA vessel segmentation algorithm incorporating 2-D DSA images to overcome the uncertainty of vessel boundary positions in 3-D. The clear vessel contours within 2-D DSA images are used to locally control the 3-D vessel segmentation method such that ambiguous 3-D vessel boundaries are enriched by 2-D information. The combination of innovative 2-D and 3-D related vessel segmentation algorithms form a framework providing 3-D DSA vessel segmentation results of highest accuracy.

This thesis provides scientific progress within the mentioned research fields contributing to the community of medical image segmentation as well as to the hemodynamic simulation community. Below, the list summarizes the major scientific contributions:

- A novel summation algorithm for 2-D DSA series has been developed separating DSA series into three parts automatically and provides one final sum image showing all major vessel branches of the series. This summation is based on strong features allowing a complete automatic classification. This algorithm is detailed within Chapter 2 and published in [Schu 11a].

- 2-D DSA images are segmented by a local adaptive contrast enhancement method which is a simple but effective approach overcoming the heterogeneous contrast agent distribution. This algorithm is described in Chapter 3 and has been already presented in [Schu 11b].

[1] www.ansys.com

- A centerline method for 3-D rotational angiography data is presented within this thesis which encodes a novel regularization to handle vessel artifacts like inhomogeneous contrast distribution, large and elliptical-shaped vessels. This regularizer keeps the centerline at the actual vessel center axis even for vessel branches afflicted with such artifacts by using statistical thresholding and distance map computation. Chapter 4 describes this methodology in detail.

- Chapter 5 introduces a novel 2-D driven 3-D vessel segmentation algorithm to overcome the uncertainty of the vessel boundary position in 3-D. The 3-D segmentation is done by interleaved ellipsoids ensuring local adaptivity in a parametric way. 2-D DSA edge information can be used and incorporated to drive the 3-D parametric segmentation towards the 2-D vessel boundary position.

- Chapter 6 and 7 outline one future application of the 3-D vessel segmentation result, i. e. performance of blood flow simulation. Chapter 6 shows for the first time a comparison between different meshing elements and a corresponding mesh independence analysis for cerebral vessel geometries [Spie 11c]. Chapter 7 illustrates the effects of different patient-specifc vessel geometries w.r.t. blood flow simulation.

1.6 Outline

The outline of this thesis is structured according to the individual steps of the hemodynamic simulation workflow. The main focus of this work is on vessel segmentation in 2-D and 3-D DSA images covered by the first two parts. The third part describes the impact of mesh accuracy and vessel geometry variations on hemodynamic simulation results. An overview of the overall organization of this thesis together with the interdigitation of the specific chapters is given in Figure 1.6.

Part I of this thesis describes the 2-D pre-processing and segmentation steps which are necessary to perform the 2-D driven 3-D vessel segmentation approach introduced in **Part II** of this thesis.

Chapter 2 details a novel classification-based summation algorithm for 2-D DSA series. Since the vessel information is usually depicted within a few images, the proposed method automatically splits such DSA series into three parts, i.e. mask, arterial and parenchymal phase to provide one *final image* showing all important vessels. The phase border detection regarding mask/arterial phase is done by classification methods like Perceptron, SVM etc. and for the arterial/parenchymal phase, a simple but effective threshold-based method is applied. The evaluation shows that the *final image* exhibits less noise. The signal-to-noise ratio (SNR) increased by up to 182%. The phase borders have been correctly determined with a detection rate of 93% and 50% respectively. This *final image* partially delivers the input for the 2-D vessel segmentation approach illustrated in Chapter 3.

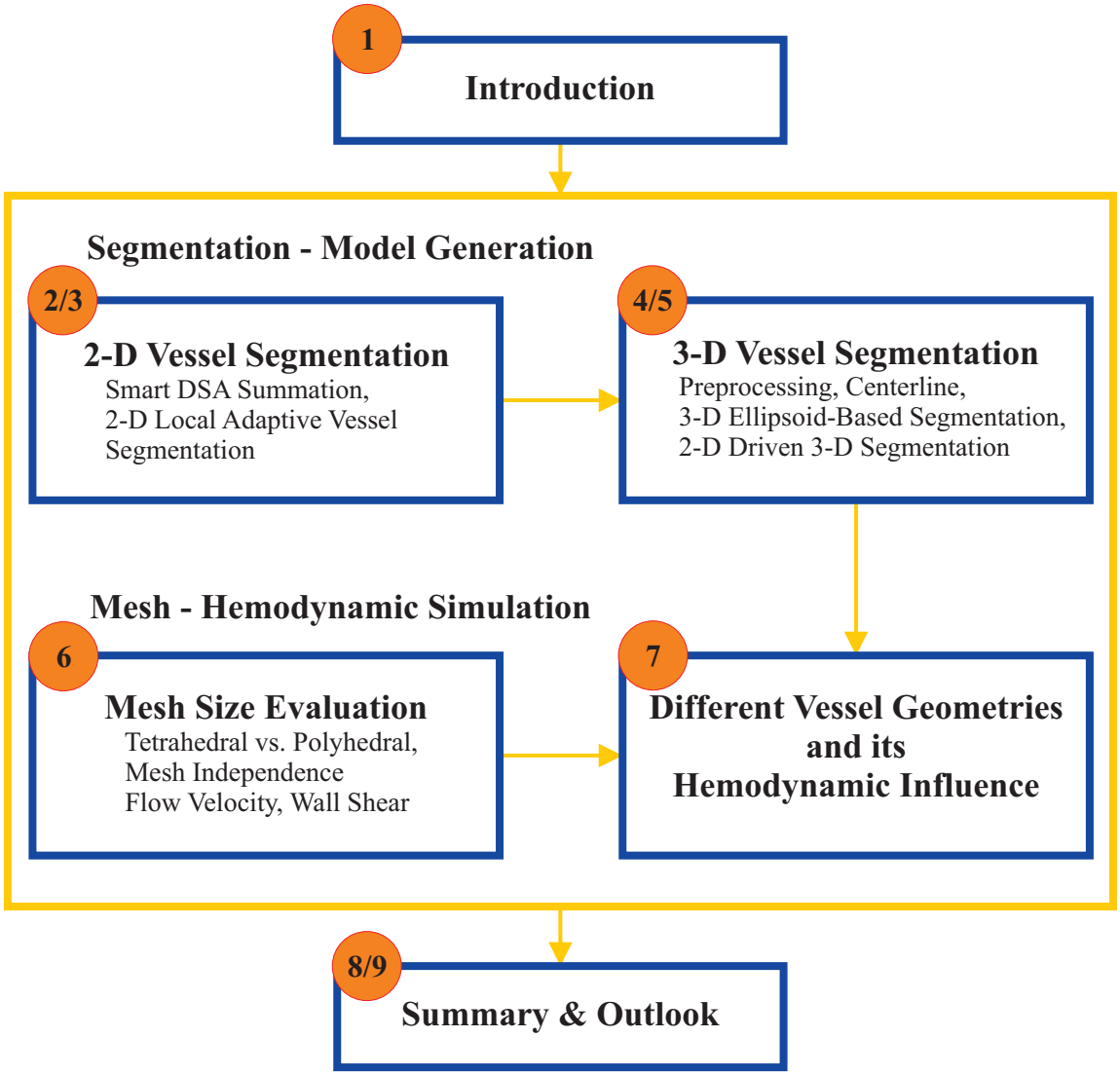

Figure 1.6: Thesis structure. The core part of this thesis is highlighted by the yellow box where each blue box represents one chapter numbered by the orange circle.

Chapter 3 introduces a novel semi-automatic vessel segmentation method based on local adaptive contrast enhancement. Its input is either the *final image* from Chapter 2 or the 2-D X-ray projection images which were acquired during the acquisition of the 3-D DSA image as illustrated in Figure 1.4 (b). The vessel branches to be segmented on the image are selected by the forward projected 3-D centerline or by a set of manual selected seed points. The algorithm uses bilateral filtering followed by local contrast enhancement to eliminate intensity inhomogeneity that is caused by unequal contrast agent distributions within the vessels. The segmentation algorithm is extensively evaluated on 45 different DSA images and exhibits a mean Hausdorff distance of 22 pixels and sensitivity of 89%.

Part II describes the key contribution of this thesis which denotes the development of a 3-D vessel segmentation algorithm which is driven by 2-D vessel infor-

mation being clinically considered as gold standard regarding vessel diameters or neck size of aneurysms.

Chapter 4 describes two pre-processing steps for the 3-D vessel segmentation, i. e. a statistical threshold segmentation method using prior knowledge regarding the specific intensity composition of 3-D DSA datasets and a graph-based vessel centerline computation approach. 3-D DSA volumes usually exhibit three intensity categories, i. e. high (vessel structures), medium (artifacts) and low (background) intensity values. The intensity distribution is modeled within a set of small boxes using a 3-component *Gaussian mixture model* (GMM). The boxes are centered at randomly chosen voxel positions showing the highest intensity values. The two highest mean values are averaged yielding the final statistical threshold which is used as pre-segmentation step. The centerline computation approach is based on the work of [Guel 08] but extended by adaptations to handle intensity inhomogeneity within vessel branches which appear in 3-D DSA volumes. The extensions are the skeletonization of the pre-segmented volume together with a distance map. Both steps are evaluated on ten different patient datasets.

Chapter 5 outlines a novel vessel segmentation approach for 3-D DSA datasets which seamlessly combines 2-D and 3-D image information. 3-D segmentation is a crucial step concerning vessel geometry analysis which often lacks a method to validate the results for the individual patient. This chapter proposes a novel 2-D DSA driven 3-D vessel segmentation and validation framework. An ellipsoid vessel model is applied to deliver the initial 3-D segmentation. To assess the accuracy of 3-D vessel segmentation, its forward projections are iteratively overlaid with the corresponding 2-D DSA projections. Local vessel discrepancies are back-projected to adjust the 3-D vessel segmentation. Our framework has been evaluated on phantom data as well as on ten patient datasets.

Part III of this thesis details the influence of varying mesh sizes and mesh element types on the simulation result. Moreover, small vessel geometry changes caused by different segmentation approaches have been evaluated w. r. t. hemodynamic simulations.

Chapter 6 describes on computation parameters such as volume element type, mesh size and mesh composition to gain a better understanding of the validity regarding computational fluid dynamic (CFD) simulations. CFD results for the two most common aneurysm types (saccular and terminal) are compared for polyhedral vs. tetrahedral-based meshes and discussed regarding future clinical applications. For this purpose, a set of models were constructed for each aneurysm with spatially varying surface and volume mesh configurations (mesh size range: 5,119-258,481 volume elements). Wall shear stress (WSS) distribution on the model wall and point-based velocity measurements were compared for each configuration model. Our results indicate a benefit of polyhedral meshes in respect to convergence speed and more homogeneous WSS patterns. Computational variations of WSS values and blood velocities are between 0.84% and 6.3% from the simplest mesh and the most advanced mesh design investigated.

A hemodynamic evaluation study has been performed in **Chapter 7** to investigate different vessel geometries that originate from the same patient dataset and its impact on the simulation result. The vessel geometries are computed by three

different segmentation approaches which can be distinguished as intensity and model-based techniques. The geometries show two major dissimilarities: (1) vessel bifurcation angle variance and (2) discrepancies regarding vessel diameters. In total, five patient datasets are taken in this study which were also used in Chapter 5. The hemodynamic results revealed that small geometric changes at neuralgic points may have a major impact on the flow pattern and WSS distribution.

Chapter 8 summarizes the key contribution of this thesis and concludes this thesis by a discussion on the technological and methodological aspects of this work. Moreover, an outlook is given for future research directions within the proposed simulation workflow.

Part I

2-D Vessel Segmentation

CHAPTER 2

Classification-based Summation of 2-D DSA Series

Within a modern neuro interventional lab, there are generally two types of 2-D DSA images available, i. e. 2-D DSA series showing the blood flow through the vessels and 2-D DSA images which are used for 3-D reconstruction. The proposed methodology within this chapter focuses on the first DSA type and denotes a mandatory pre-processing step for the 2-D vessel segmentation which is described within the next chapter 3.

Before 2-D vessel segmentation can be performed on 2-D DSA series, the vessel information which is distributed over the series has to be collected and presented within one DSA image. Here, a fully automatic method is introduced summarizing a DSA series such that all major and medium vessel branches are depicted within one *final image*. This summation is done by classification which categorizes the DSA series into three distinct phases. Three strong features are proposed to perform this classification which is based on Rosenblatt's perceptron, support vector machine etc. [Duda 01]. Eight DSA series are taken to do the training of the classifier and the entire algorithm is evaluated using 14 different patient datasets. Compared to the naive approach (summation over the whole DSA series), our *final image* shows an increased signal-to-noise ratio (SNR) of up to 182%. The results of this chapter have been published in [Schu 11a] and patented [Spie 10].

2.1 Motivation

2-D DSA represents the state-of-the-art imaging modality for cerebrovascular diseases (aneurysms or stenosis) in terms of vessel analysis in diagnosis, interventional treatment planning and to assess the success of an intervention [Brod 82]. 2-D DSA series are of particular interest during diagnosis and follow up examinations because they deliver a very good impression about the blood flow together

with the highest spatial resolution available with modern C-Arm systems. This flow information denotes one of the key features in order to judge the degree of stenosis or the sealing of a coil embolization. Figure 2.1 gives an impression how such DSA series typically look like.

Due to its high image quality and spatial resolution, 2-D DSA series have become more and more important concerning post-processing applications as the literature shows, e.g. vessel segmentation [Sang 07, Boua 07, Fran 08, Fran 09], vessel type classification [Kang 09], registration of patient images acquired at different times [Meij 99b] and catheter tracking [Baer 03, Spie 09]. Not only segmentation or registration tasks have been addressed, also the flow information itself has attracted the development of algorithms to detect bolus propagation and tracking in real-time [Wu 98, Cheo 03, Lu 06].

The aforementioned flow is the reason for the distribution of the vessel information over the DSA series leading to three different image phases within a DSA series, i.e. *mask*, *arterial* and *parenchymal* phase. While the contrast agent injection starts, the image acquisition is already running. Images of the *mask* phase contain no information about the vessel tree since the contrast agent has not reached the region of interest. The *arterial* phase images usually depict the most important information to analyze aneurysms or stenosis because the contrast medium flows through the major vessel branches. This phase reveals information about vessel diameters, dome size of aneurysms and degree of stenosis which is of particular interest for post-processing algorithms like vessel segmentation, registration or comparison between DSA acquired hemodynamic information and CFD blood flow results. Unfortunately, this information is often split up in several images because of its dynamic nature. This makes it difficult for post-processing applications to handle vessel segmentation or registration. Thus, the complexity of such kind of methods rapidly increases while computing satisfying results. Finally, the *parenchymal* phase consists of images showing capillary or the beginning of venous blood flow. Consequently, the borders between vessels and background are rather blurred out. One *final image* covering all major vessel branches without parenchymal filling would make segmentation and registration tasks easier to perform. This can be done by either manual selection of the *arterial* phase images or by simple summation over all images of the DSA series. However, the summation over all series images will lead to a final image that is blurred by the *parenchymal* phase images and contains more noise. We propose a novel DSA image summation algorithm which is based on a classification method to compute one *final image* given a DSA series. This *final image* only consists of images belonging to the *arterial* phase and it is computed either by the sum or by taking the minimum intensity of all these images. Hence, the borders of the aforementioned phases are automatically detected. Our approach is experimentally evaluated on 14 real data image series from six different patients.

2.2 Methods

The algorithm starts with a DSA series $\mathcal{K}$ as input and computes a *final image* $\mathcal{K}_{\text{final}}$ which contains all major vessels. Our approach is divided into two main steps:

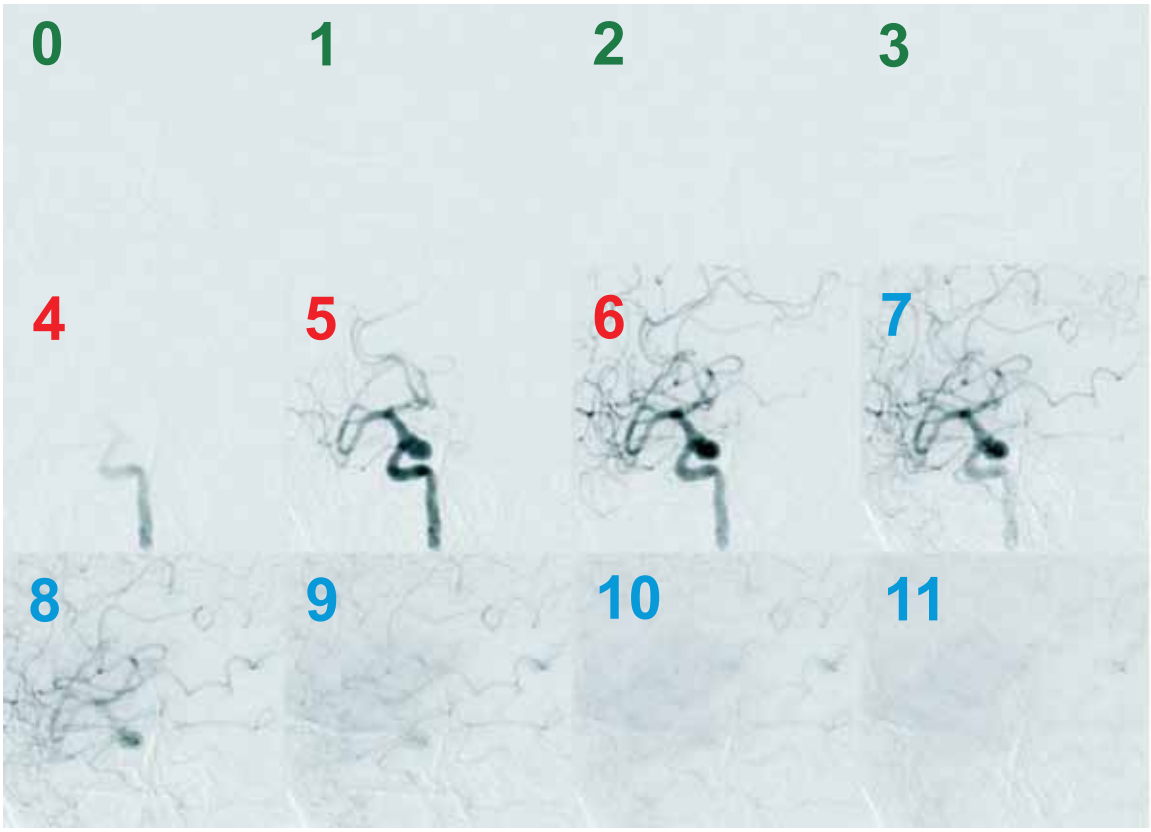

$\mathcal{K}_6$

Figure 2.1: Phase classification results for DSA series $\mathcal{K}_6$. The color of the image number shows the phase association computed by the classification-based separation method, i.e. green, red and blue denote mask, arterial and parenchymal phase respectively.

1) automatic separation of the series $\mathcal{K}$ into the three predefined phases (mask, arterial and parenchymal) and 2) combination of all DSA images corresponding to the arterial phase by summation or minimum intensity. The mask/arterial phase border is determined by a classifier based on three features (see Figure 2.2 (a) and Figure 2.4) and the arterial/parenchymal phase border is found by a threshold-based method working on the *change images* (see Figure 2.5).

The method section is organized as follows: Subsection 2.2.1 describes the main idea of our method followed by subsection 2.2.2 that introduces the applied features for the phase separation in detail. The remaining sections 2.2.3 and 2.2.4 delineate the classification methods applied to detect the mask/arterial and arterial/parenchymal phase border.

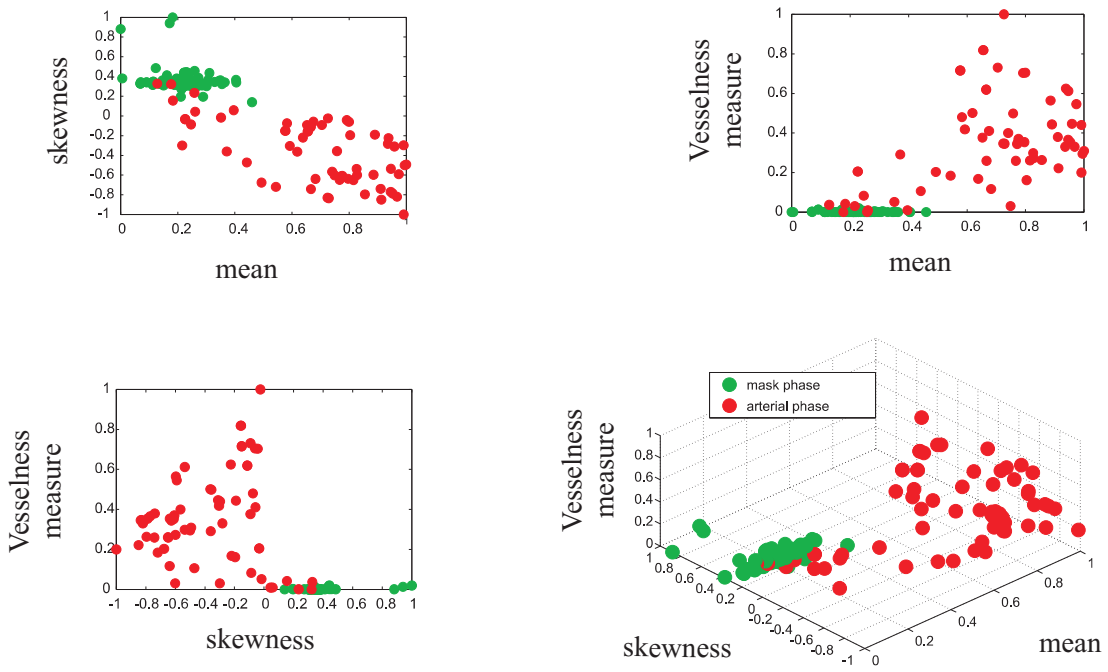

Figure 2.2: Illustration of the feature space of the training data in 2-D and 3-D. The 2-D images (top row) depict orthogonal projections of the 3-D feature space on the three planes.

2.2.1 Basic Idea

A DSA series comprises a set of DSA frames $\mathcal{K}_i = \langle s_{i,j} \rangle_{j=0}^{N-1}$ where N denotes the total number of frames within the i^{th} series. Given series $\mathcal{K}_i$, one *final image* $\mathcal{K}_{i,\text{final}}$ denotes the combination of all images of $\mathcal{K}_i$ belonging to the arterial phase, i.e. it depicts all major vessel structures. The combination of this arterial phase can be performed by either taking the pixelwise sum of these images

$$\mathcal{K}_{i,\text{F,SUM}} = \sum_{j=L}^{U} \mathcal{K}_{i,j} \tag{2.1}$$

or by computing the minimum intensity of all arterial phase images:

$$\mathcal{K}_{i,\text{F,MIN}} = v_{\text{MIN}}(\mathcal{K}_i, \boldsymbol{u}) = \min_{j \in [L \ldots U]} v(\mathcal{K}_{i,j,\boldsymbol{u}}) \tag{2.2}$$

$\mathcal{K}_{i,\text{F,SUM}}$ and $\mathcal{K}_{i,\text{F,MIN}}$ are the sum and the minimum image of the arterial phase. The elements of the sum belong to a fixed interval which is a subsequence of the acquired series $\mathcal{K}_i$. L and U denote the frame indices of the lower and upper bound of the sum respectively which mark mask/arterial and arterial/parenchymal phase border. $v(j, \boldsymbol{u})$ is the pixel intensity on the j^{th} image at position $\boldsymbol{u} \in \mathbb{R}^2$. The bounds, L and U, can usually be found by two approaches: 1) manual selection and summation or 2) L and U are simply set to zero and $N-1$ respectively such

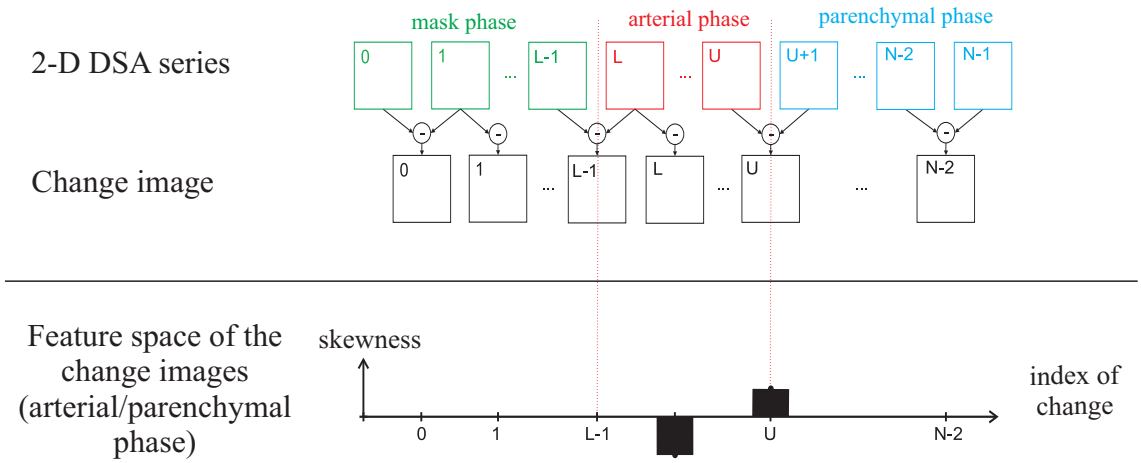

Figure 2.3: It shows a schematic illustration of the automatic phase separation together with the computation of the change images. Bottom row depicts the skewness of change images. The border between arterial and parenchymal phase is detected by a switch of the skewness from negative to positive range.

that the sum covers all images within the series. This naive summation can be written in terms of phases as follows:

$$\mathcal{K}_{i,\text{NaSum}} = \underbrace{\sum_{j=0}^{L-1} \mathcal{K}_{i,j}}_{\textit{Mask}} + \underbrace{\sum_{j=L}^{U} \mathcal{K}_{i,j}}_{\textit{Arterial}} + \underbrace{\sum_{j=U+1}^{N-1} \mathcal{K}_{i,j}}_{\textit{Parenchymal}} \tag{2.3}$$

where NaSum denotes naive summation. Now, the feature-based classification of these two borders is addressed such that $\mathcal{K}_i$ can be automatically divided into the three aforementioned phases.

2.2.2 Feature Selection

The features are computed on two regions of interest (ROI) as illustrated in Figure 2.4 (upper left corner). The ROIs can be defined due to the prior knowledge about the position of the patient on the table of the C-Arm system, i.e. the inflow of the contrast agent (intra-arterial injected) on the image is from the bottom to the top. The border L is computed on region Ω_L covering the lower 20% of a DSA frame. Ω_L is indicated by the red and green boxes in Figure 2.4 (upper left).
The first frame of the arterial phase $\mathcal{K}_{i,L}$ is characterized by the very first appearance of contrast agent inflow on the image. The following three features are chosen to quantify this observation:

1. the mean of intensities μ
2. the skewness γ of the intensity histogram
3. the vesselness measure ψ

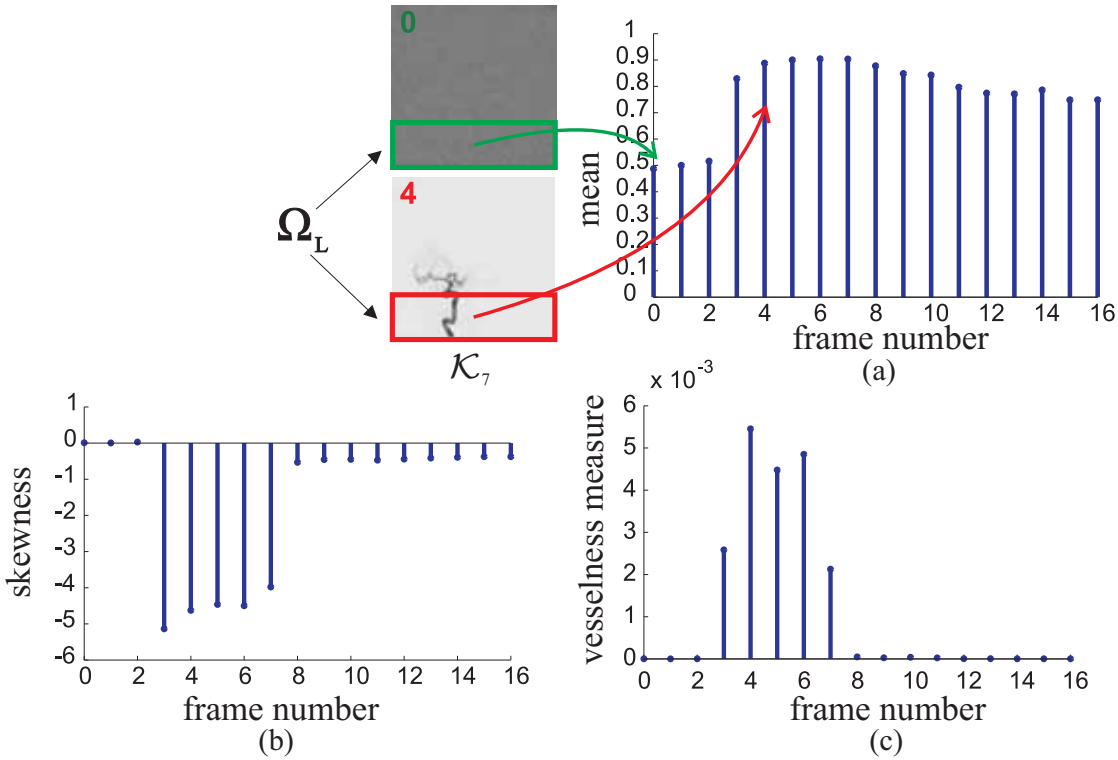

Figure 2.4: Behavior of the selected features over an entire DSA series with 16 frames. The border between mask and arterial images is clearly indicated by the mean μ (a), skewness γ (b) and the vesselness measure ψ (c) at frame 3. These features are computed within the box Ω_L which is illustrated in the upper left.

Figure 2.2 gives an overview about the feature space. To perform the feature extraction, the intensities of a DSA series are normalized in two ways resulting in two different DSA series, i.e. $\mathcal{K}_{fs,i}$ and $\mathcal{K}_{ss,i}$. The intensities of $\mathcal{K}_{fs,i}$ are normalized to $[0,1]$ per frame. Within series $\mathcal{K}_{ss,i}$ the entire intensity range of the series is considered for normalization of the intensities between zero and one. $\mathcal{K}_{fs,i}$ is used to amplify the shift of the intensity mean between images of the mask and arterial phase. This shift can be visualized by comparing the black intensities of mask and arterial images. The black intensities of arterial images are much lower than those within images of the mask phase due to the inflowing contrast agent. Consequently, the background intensities covering 90% of the image are shifted to higher intensities inducing an entire shift of the intensity mean. The skewness γ and the vesselness measure ψ are computed on $\mathcal{K}_{ss,i}$. ψ is based on the Hessian matrix and the corresponding eigenvalues λ_0 and λ_1 [Fran 98]. ψ is defined as

$$\psi = \sum_{\boldsymbol{u} \in \Omega_L} |\lambda_{\boldsymbol{u},1} - \lambda_{\boldsymbol{u},0}| \,, \tag{2.4}$$

where $\boldsymbol{u} \in \mathbb{R}^2$ denotes a pixel of region Ω_L. The behavior of the three features concerning a DSA series is depicted in Figure 2.4. The inflowing contrast agent leads to a rapid change of the values of the features. The intensity mean regarding ROI Ω_L computed on $\mathcal{K}_{fs,i}$ is shifted in positive direction (see Figure 2.4 (a)). As

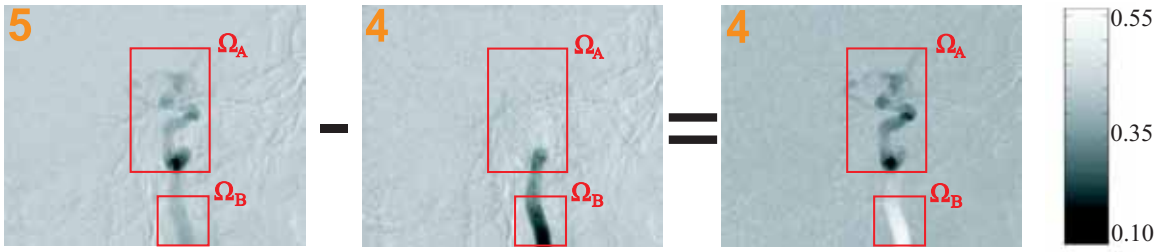

(a) DSA frame (b) DSA frame (c) Change image

Figure 2.5: This shows an example for the computation of a change image. Only the upper 80% of the images are shown. Within region Ω_A of DSA frame 5 there is additional vessel information which is not present in DSA frame 4 and in region Ω_B vice versa.

illustrated in Figure 2.4 (b), the skewness becomes highly negative and the vesselness measure value ψ is rapidly increasing. These features are concatenated to the feature vector $\boldsymbol{w}_L$:

$$\boldsymbol{w}_L = \begin{pmatrix} m \\ \gamma \\ \psi \end{pmatrix}. \tag{2.5}$$

The upper border U (arterial/parenchymal phase) is determined using the so called *change image*. A *change image* denotes the subtraction of two subsequent images within the series $\mathcal{K}_{ss,i}$:

$$\mathcal{K}_{i,j,\text{change}} = \mathcal{K}_{ss,i,j+1} - \mathcal{K}_{ss,i,j} \quad j = L, ..., N-2. \tag{2.6}$$

Here, the upper 80% of $\mathcal{K}_{i,j,\text{change}}$ denotes the region Ω_U that is used to detect the upper border U. $\mathcal{K}_{i,j,\text{change}}$ is normalized to $[0,1]$. Vessels which are not present within $\mathcal{K}_{ss,i}$ but within $\mathcal{K}_{ss,i,j+1}$ will appear darker in $\mathcal{K}_{i,j,\text{change}}$ than those that have been already depicted in $\mathcal{K}_{ss,i}$. An example of a *change image* is shown in Figure 2.5. The region A of DSA frame 5 contains vessel information that is not present in DSA frame 4 and appears darker in the corresponding *change image*. Region B shows the opposite. The transition between the arterial and parenchymal phase is characterized by the absence of major additional vessels meaning that the *change image* becomes more and more brighter. Again, this behavior can be simply observed by the skewness γ of region Ω_U. Negative skewness means darker structure on brighter background and positive skewness vice versa. Thus, the border between arterial and parenchymal phase is distinguished by one single feature.

2.2.3 Learning-based Classification of the Lower Border

Let us consider the classification of the lower border L as a two class problem, i.e. the separation of images into mask and arterial phase. A supervised training of our classifier is performed by manual selection of M frames of the mask and arterial phase of different DSA series. The set Λ contains the feature vectors, $\boldsymbol{w}_{L,i}$,

of the training data together with a class label ω_i , i.e. zero equals mask phase and one denotes arterial phase:

$$\Lambda = \{(\boldsymbol{w}_{L,i}, \omega_i)\}_{i=0}^{M-1}. \tag{2.7}$$

The feature vectors are normalized w.r.t. zero empirical mean. The goal now is to set up a linear discriminant function $g(\boldsymbol{w}_L)$, i.e. a plane E which separates the features of the mask phase from those of the arterial phase. H is defined as:

$$H: \; g(\boldsymbol{w}_L) = \boldsymbol{n}^T \boldsymbol{w}_L - d, \tag{2.8}$$

where $\boldsymbol{n} \in \mathbb{R}^3$ is the normal vector and $d \in \mathbb{R}$ the perpendicular distance to the origin. The principal component analysis (PCA) without dimension reduction performed on the 3-D feature space yields three eigenvectors $\{\boldsymbol{e}_j\}_{j=0,1,2} \in \mathbb{R}^3$ with three eigenvalues λ_0, λ_1 and λ_2 ($\lambda_0 \leq \lambda_1 \leq \lambda_2$) that are used as an initial estimation of H. $\boldsymbol{e}_0$ and $\boldsymbol{e}_1$ span the initial plane H with its normal vector $\boldsymbol{e}_2$, i.e. $\boldsymbol{n}$ is initialized with $\boldsymbol{e}_2$. The perceptron algorithm [Duda 01] is applied to iteratively optimize the position and orientation of H such that the misclassification becomes minimal. The perceptron criterion function is the sum of distances of misclassified features:

$$D_p(\boldsymbol{n}, d) = -\sum_{\boldsymbol{w}_{L,i} \in \mathrm{Y}} \omega_i g(\boldsymbol{n}^T \boldsymbol{w}_L - d) \tag{2.9}$$

where Y is the set of misclassified feature vectors and ω_i is defined as:

$$\omega_i = \begin{cases} 1 & ; \text{ class 1 i.e. mask images} \\ -1 & ; \text{ class 2 i.e. arterial images} \end{cases} \tag{2.10}$$

The response function δ_L of the classifier which separates the DSA frames of the mask phase and the arterial phase is now defined as

$$\delta_L(\boldsymbol{w}_L) = \begin{cases} 0 & ; \text{if} \quad g(\boldsymbol{w}_L) < 0 \\ 1 & ; \text{if} \quad g(\boldsymbol{w}_L) \geq 0, \end{cases} \tag{2.11}$$

where $\delta_L = 0$ and $\delta_L = 1$ means that the DSA frame belongs to the mask and arterial phase, respectively. The pseudo code of this classification algorithm is illustrated in Program 2.1.

2.2.4 Threshold-based Classification of the Upper Border

As illustrated in Figure 2.3, the upper border U is determined by the skewness of the *change image* $\mathcal{K}_{i,U,\text{change}}$. When the arterial phase fades to the parenchymal phase the skewness of the *change image* switches from negative values to positive ones. This change of sign is considered as the feature indicating the beginning of the parenchymal phase.

Program 2.1: Classification-based summation of DSA series

Input: $\mathcal{K}_{\text{Train}}, \mathcal{K}_{\text{Work}}$
Output: $\mathcal{K}_{\text{F,SUM}}, \mathcal{K}_{\text{F,MIN}}$
begin
  `// Training phase for mask/arterial phase border`
  $\Lambda \longleftarrow \emptyset$
  foreach $\mathcal{K}_{Train}$ **do**
    feature computation for each frame i in $\mathcal{K}$
    $\boldsymbol{w}_{L,i} \longleftarrow (\mu, \gamma, \psi)^T)$
    $\Lambda \longleftarrow \Lambda + (\boldsymbol{w}_{L,i}, \omega_i)$
  end
  train chosen classifier, e. g. Perceptron, SVM etc.
  `// Working phase`
  $MP, AP \longleftarrow \emptyset$ `// MP: mask phase, AP: arterial phase`
  `// Mask/arterial phase border detection`
  foreach $\mathcal{K}_{Work}$ **do**
    feature computation for each frame i in $\mathcal{K}$
    $\boldsymbol{w}_{L,i} \longleftarrow (\mu, \gamma, \psi)^T$
    if $\delta_{L,i}(\boldsymbol{w}_L) < 0$ **then**
      $MP \longleftarrow MP + i$
    else
      $AP \longleftarrow AP + i$
    end
  end
  `// Create final DSA image`
  $\mathcal{K}_{\text{F,SUM}} \longleftarrow \sum AP$ `// Pixelwise summation`
  $\mathcal{K}_{\text{F,MIN}} \longleftarrow \min AP$ `// Pixelwise minimum`
end

2.3 Evaluation and Results

Our automatic summation method is evaluated on 14 different 2-D DSA series with a length varying from 12 to 32 frames. The series were acquired during endovascular interventions at the Department of Neuroradiology (University Hospital Erlangen, Germany) using Siemens C-Arm System (AXIOM Artis dBA, Siemens AG Healthcare Sector, Forchheim, Germany). The x/y dimension of the series ranges between 512×512 and 1440×1440. The pixel spacing in x/y direction is 0.154/0.154 mm for all series. The injection protocol exhibits 5 ml of contrast agent (concentration 300) with a flow rate of 2-3 ml/sec. The frame rate is two images per second during the arterial phase and is lowered to 0.5 frames per second during parenchymal phase. The training of the classifier was done with eight DSA series which were not part of the evaluation set.

2.3.1 Methods of Evaluation

Automatic Phase Selection

In order to evaluate the automatic phase selection a gold standard was built by a medical expert who manually partitioned each series of the evaluation set into the three phases. The labeling of the training set was approved by Dr. T. Struffert (Department of Neuroradiology, University Hospital Erlangen). The main focus was on categorizing those images into the arterial phase which depict major vessel branches concerning endovascular intervention planning, i.e. coil embolization of aneurysms or stent placement. The partitioning results of our automatic summation method are compared to this gold standard evaluation set.

Final Image

This evaluation exhibits three *final images*. The first one is created by summing up the entire DSA series. The second denotes the sum of all arterial phase images, $\mathcal{K}_{\mathrm{F,SUM}}$, and the third one represents the minimum intensity image of all arterial phase images $\mathcal{K}_{\mathrm{F,MIN}}$. Furthermore, a mask image is established defining two regions. For the first region all major vessel branches within the vicinity of the pathology were manually segmented by a medical expert in order to evaluate the quality of the *final image* with respect to foreground. For the second region areas in the background were manually segmented by a medical expert in order to evaluate the quality of the *final image* with respect to background. These background areas do not show any vessel structures within the *final images*. The signal-to-noise-ratio (SNR) on background regions and the sum of gradient magnitudes on foreground regions are used for quantitative comparison. Unlike multimedia communication, the original input signal of the *final image* is not known. For quality assessment, however, we consider the signal to be the intensity mean and noise as the intensity standard deviation concerning selected background regions. We would ideally expect a high mean and a rather low standard deviation because of image sum-

mation and the absence of structural changes within these regions. The SNR is accordingly determined as

$$SNR_{\mathcal{B}} = \frac{\mu_{\mathcal{B}}}{\sigma_{\mathcal{B}}} \tag{2.12}$$

where $\mu_{\mathcal{B}}$ and $\sigma_{\mathcal{B}}$ are the intensity mean and the standard deviation of the background region $\mathcal{B}$, respectively. The shapes of the background regions were chosen arbitrarily because it is difficult to define a box region that is big enough and contains no vessel structure within all *final images* (see Figure 2.6 yellow boxes compared to the green regions).

Considering a perfect 2-D DSA acquisition, the contrast agent will be uniformly distributed within the vessels. Thus, the gradient magnitudes within the vessel branches should be very small in an ideal case. The sum of gradient magnitudes ζ_{sum} is used to analyze the image quality within the manual segmented vessel branches (Figure 2.6 red regions) defined as

$$\zeta_{\text{sum}} = \frac{1}{M} \sum_{i=0}^{M-1} \|\nabla \boldsymbol{u}\|_2 \tag{2.13}$$

where M denotes the number of pixels of the image.

2.3.2 Experimental Results

All experiments were conducted on an AMD Athlon 7750 Dual-Core, 1.38 GHz with 3 GB of main memory. Our approach is implemented in C++. The computation time of this method is on average one second. The first column of Figure 2.6 shows the result of the third *final image* where only the minimum intensities of all arterial phase images are taken. The second column illustrates the second *final image* after summing up the arterial phase images and the third column after summing over the entire DSA series. In the last column, the mask image is depicted. The red regions correspond to foreground areas and the green regions to background areas.

Table 2.1 and 2.2 give a quantitative insight on all experimental results. According to table 2.2, the detection result of the lower and upper border of the arterial phase yields a correspondence of 93% and 50% comparing to the expert-based border selection. The maximum shift between the expert-based and our automatic phase separation method is one image. Considering the feature space for the separation of the mask and arterial phase, however, there might be other classification methods suitable like support vector machine (SVM) etc. delivering similar results. The WEKA machine learning software [Hall 09] has been applied to explore different kinds of classifier working on the entire feature space and evaluated in a 30-fold cross-validation. Table 2.3 summerizes the classification results.

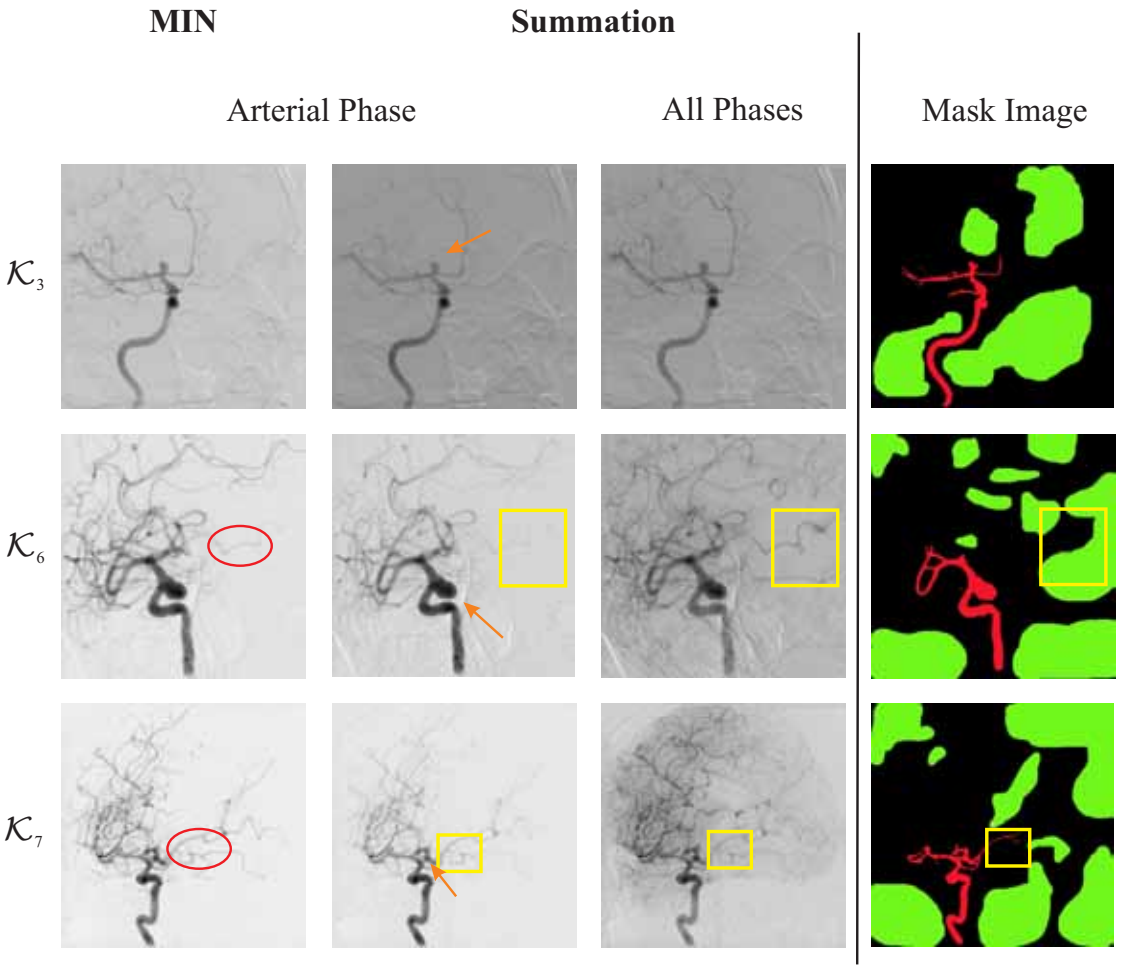

Figure 2.6: This set of images shows the *final image* concerning the DSA series s3, s6, and s7: first and second left column automatic method covering only arterial phase images (minimum intensity/summation); third left column summation over all phases. The right column illustrates the two different regions used to quantitatively evaluate the *final sum images* regarding SNR and ζ_{sum}. Green and red colors denote the selected background (SNR) and foreground (ζ_{sum}) regions respectively.

Table 2.1: Summary of the evaluation results. AP appreviates Arterial Phase. SUM and MIN denotes summation and minimum intensity respectively.

	Vessel Region - ζ_{sum}				Background Region - SNR			
Study (#Frames)	$\mathcal{K}_{F,MIN}$	$\mathcal{K}_{F,SUM}$	All Phases	$\mathcal{K}_{F,MIN}$vs. All / $\mathcal{K}_{F,SUM}$vs. All [%]	$\mathcal{K}_{F,MIN}$	$\mathcal{K}_{F,SUM}$	All Phases	$\mathcal{K}_{F,MIN}$vs. All / $\mathcal{K}_{F,SUM}$vs. All [%]
$\mathcal{K}_1$ (32)	0.0208	0.0199	0.0210	-0.9/-5.5	73.3431	57.9115	14.8013	395.5/291.26
$\mathcal{K}_2$ (15)	0.0221	0.0202	0.0239	-7.3/-15.5	36.0246	27.6717	21.1786	70.1/30.66
$\mathcal{K}_3$ (13)	0.0155	0.0126	0.0192	-19.1/-34.6	37.7886	27.0608	22.1141	70.9/22.37
$\mathcal{K}_4$ (13)	0.0144	0.0165	0.0186	-22.3/-10.9	42.5421	35.7652	12.1529	250.1/194.29
$\mathcal{K}_5$ (13)	0.0202	0.0182	0.0229	-11.4/-20.6	34.1857	41.6519	12.2046	180.1/241.28
$\mathcal{K}_6$ (12)	0.0222	0.0223	0.0230	-3.5/-3.2	49.9320	37.7822	17.0831	192.3/121.17
$\mathcal{K}_7$ (17)	0.0235	0.0226	0.0293	-19.6/-22.9	67.9300	57.0660	17.1421	296.3/232.90
$\mathcal{K}_8$ (14)	0.0162	0.0146	0.0188	-13.7/-22.4	70.8132	80.5706	35.6433	98.7/126.05
$\mathcal{K}_9$ (19)	0.0194	0.0152	0.0236	-17.5/-35.6	75.7862	79.4825	25.3266	199.2/213.83
$\mathcal{K}_{10}$ (26)	0.0184	0.0175	0.0239	-22.8/-27.0	47,3056	59.9722	15.7078	201.2/281.80
$\mathcal{K}_{11}$ (25)	0.0145	0.0113	0.0131	11.1/-13.6	91.0556	108.3851	47.1789	93.0/129.73
$\mathcal{K}_{12}$ (16)	0.0194	0.0198	0.0208	-6.7/-5.2	70.4309	60.6687	23.5206	199.4/157.94
$\mathcal{K}_{13}$ (16)	0.0164	0.0157	0.0213	-22.5/-26.2	63.7816	46.3237	19.2673	231.0/140.43
$\mathcal{K}_{14}$ (18)	0.0193	0.0207	0.0216	-10.7/-4.3	58.5047	50.7174	33.2975	75.7/52.32
Mean	0.0187	0.0176	0.0215	**-11.9/-17.7**	58.5303	55.0735	22.6156	**182.4/159.72**
σ	0.0029	0.0035	0.0037	**9.8/11.0**	17.4718	22.5975	9.9849	**91.7/87.39**

The SNR of the background regions is increased concerning both *final images* (see table 2.1), i. e. the summation and the minimum intensity image concerning all arterial phase images show an average increase of 160% (87 standard deviation) and 182% (92 standard deviation) respectively. Within both final images, the vessel regions appear much smoother and homogeneous which could be quantitatively shown by the results of the ζ_{sum}, e.g. its value could be reduced on average by -18% (11 standard deviation) for the arterial summation image and by -12% (10 standard deviation) for the minimum intensity image. The improvement of the image quality can be clearly seen by Figure 2.6. The *final images*, covering only arterial phase images, appear clearer with less moving artifacts. Moreover, all major vessel branches within the vicinity of the aneurysms (indicated by the orange arrows in Figure 2.6) are evidently illustrated allowing the physician to perform diagnosis and treatment planning.

2.4 Discussion

The proposed method provides an efficient way to perform phase separation on 2-D X-ray DSA image series. To the best of our knowledge, there is no comparable method out in the field handling phase separation on DSA series. The major contribution of this work states a classification-based DSA image summation method which separates the DSA series into three phases and finally provides one *final image* summarizing all arterial phase images. The experimental results are promising for clinical application. The lower border of the *arterial* phase was detected with a classification rate of 93%. The upper border yields a detection result of 50%. This is because of the smooth transition between the *arterial* and *parenchymal* phase as illustrated in Figure 2.1 ($\mathcal{K}_3$: images 8,9; $\mathcal{K}_6$: images 6,7; $\mathcal{K}_7$: images 6,7). Hence, the position of the upper border would be differently determined. Figure 2.7 illustrates two examples where the lower and upper bound of the *arterial* phase are not properly detected. The upper bound of $\mathcal{K}_1$ may even be handled differently by a medical expert (compare image 8 with image 9). The lower bound of $\mathcal{K}_{14}$ was not correctly recognized due to the fact that only a small area shows an inflow of contrast agent as highlighted with the yellow circles. A test on inter observer variability, however, was not performed during this initial evaluation because the impact on the *final image* is low. If one *parenchymal* image was spuriously added as *arterial* phase image the quality of the *final image* would not be significantly influenced.

In this work, we used a classification technique that is based on PCA and Rosenblatt perceptron because it is easy to be implemented and worked well in our case. A comparison against other classification methods (see Table 2.3) has shown that they achieved similar results as Rosenblatt's perceptron. Our classification method is robust regarding motion from the patient or the vessels. In fact, the internal carotid artery shows some motion during the acquisition when comparing successive images. The impact on the *final image*, however, is negligible because our features are independent from motion.

Overall, the automatic summation of *arterial* phase images leads to a *final image* which exhibits less noise and moving artifacts, i.e. the SNR could be increased on

Table 2.2: Summary of the evaluation results. L and U denote lower and upper border of the arterial phase respectively. Regarding column 4, one indicates a perfect match for the border detection between our classifier and the medical expert.

	Arterial Phase Classification		
Study (#Frames)	Expert	Automatic	Borders(L/U)
$\mathcal{K}_1$ (32)	5-9	5-8	1/0
$\mathcal{K}_2$ (15)	6-10	6-9	1/0
$\mathcal{K}_3$ (13)	5-9	5-8	1/0
$\mathcal{K}_4$ (13)	5-7	5-6	1/0
$\mathcal{K}_5$ (13)	5-7	5-6	1/0
$\mathcal{K}_6$ (12)	4-6	4-6	1/1
$\mathcal{K}_7$ (17)	3-6	3-6	1/1
$\mathcal{K}_8$ (14)	4-5	4-6	1/0
$\mathcal{K}_9$ (19)	5-8	5-8	1/1
$\mathcal{K}_{10}$ (26)	5-7	5-7	1/1
$\mathcal{K}_{11}$ (25)	4-12	4-12	1/1
$\mathcal{K}_{12}$ (16)	4-8	4-8	1/1
$\mathcal{K}_{13}$ (16)	4-7	4-8	1/0
$\mathcal{K}_{14}$ (18)	4-5	3-5	0/1
Mean			93%/50%

average up to 182%. When comparing the final images based on the arterial phase, it turns out that the minimum intensity image shows slightly superior results regarding the visibility of small vessel branches. This is highlighted with red circles in Figure 2.6. Concerning medium and large vessels both final images reveal similar results.
Such *final images* deliver various advantages during the diagnosis, treatment planning and image post-processing. It may supersede browsing through image series to get an overview about the vessel tree. The complexity of post-processing algorithms like vessel segmentation or registration is decreased since all information is given at once and not distributed over several images. This can be considered as an initialization step for the vessel segmentation approaches described in [Sang 07, Fran 08].

Table 2.3: Separation of the mask and arterial phase using different classifiers.

Classifier	Mask/Arterial Phase Separation Result [%]
Naive Bayes	93.2
SVM	93.2
AdaBoost	90.9
KStar	95.1
Multilayer perceptron	95.4
Voted perceptron	93.9

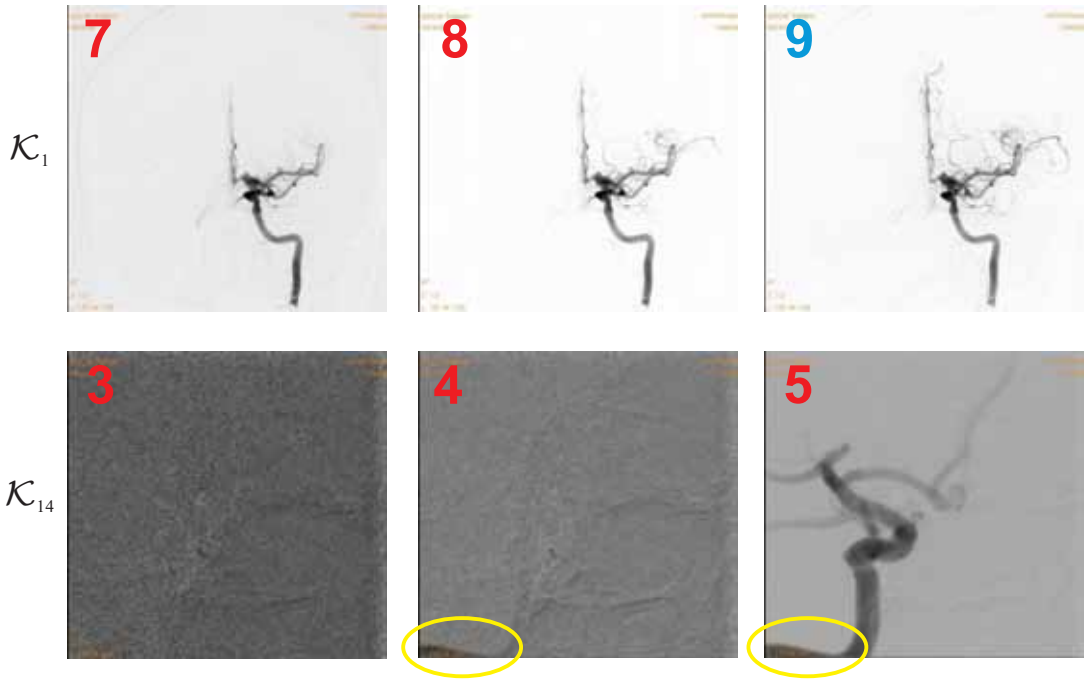

Figure 2.7: Examples of misclassifications regarding the lower and upper bound of the *arterial* phase. The upper row shows the smooth transition between *arterial* (image 8) and *parenchymal* (image 9) phase where even medical experts may decide differently. The lower row depicts an example of misclassification concerning the *mask* and *arterial* phase which is due to the small areas showing the contrast agent inflow (yellow circles).

2.5 Conclusion

The contribution of this chapter represents the smart extraction of major vessel information which is distributed over several images within a 2-D DSA series. The extraction is performed by splitting the DSA series into three phases using three strong features, i. e. mean intensity, skewness of the histogram and vesselness indicator. Based on a training set, a perceptron based classifier is trained to automatically split DSA series and to combine the arterial phase images to one *final sum* DSA image using minimum intensity projection. This *final sum* DSA image delivers the input for the next chapter where the vessel structure is segmented in a local adaptive manner.

CHAPTER 3

2-D Vessel Segmentation using Local Contrast Enhancement

This chapter describes a vessel segmentation approach for 2-D DSA images that is able to operate either as a stand-alone version in a semiautomatic way or as a fully automatic segmentation algorithm in cooperation with the 3-D vessel segmentation approach (Chapter 5). In case of stand-alone application, manual seed points have to be placed to select the vessel branches for segmentation. In fully automatic mode, the vessel branches are chosen by the forward projection of the 3-D vessel centerline. The input of this algorithm is either the *final image* from Chapter 1 or calibrated 2-D DSA images which are acquired during a 3-D DSA run. Due to inhomogeneous contrast agent distribution leading to sometimes smooth transitions between vessel contours and background, the 2-D DSA images are preprocessed by local contrast enhancement. The entire methodology is evaluated on 45 different DSA images of both input types showing a mean sensitivity of 88% and Hausdorff distance of 22 pixels. Parts of this chapter are published in [Schu 11b].

3.1 Motivation

2-D DSA images play a major role in diagnosis, treatment planning and assessment of cerebrovascular diseases, i. e. aneurysms, arteriovenous malformations and intracranial stenosis. Although 3-D DSA volumes are widely used within modern neuro interventional labs, 2-D DSA is still considered as gold standard image modality [Brin 09] especially concerning diagnosis and treatment planning, e. g. stent selection and placement. Hence, 2-D vessel segmentation will provide an important support for analyzing complex vessels, i. e. measuring vessel diameter, length or aneurysm neck and dome size. In the literature, there are various kinds of vessel detection and segmentation methods [Kirb 04, Lesa 09] available.

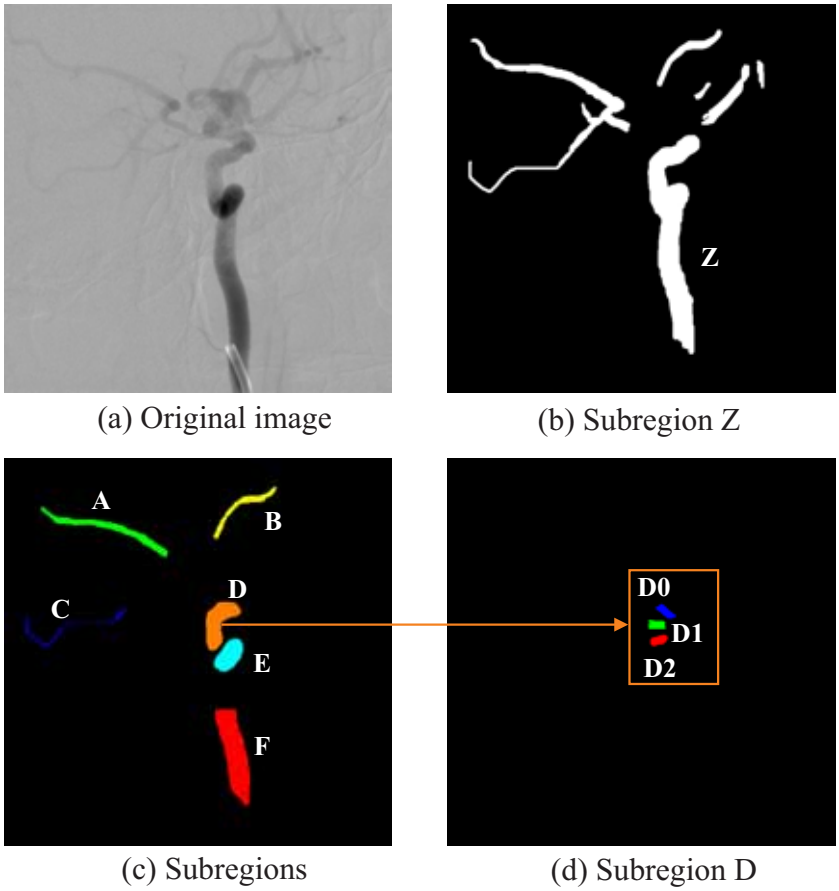

(a) Original image (b) Subregion Z

(c) Subregions (d) Subregion D

Figure 3.1: This set of images shows the inhomogeneous contrast distribution and its variation concerning different region sizes. Subfigure (a) depicts a *final sum image* and (b) illustrates the vessel region Z (white mask). This region is subsequently subdivided into smaller regions as shown in (c) and (d).

However, 2-D vessel segmentation techniques applied on 2-D DSA images are rarely described [Sang 07].

At first glance, the segmentation of such kind of vessels seems to be straightforward, however, there are factors of influcence making it a challenging task: Different vessel regions exhibit different statistical information due to inhomogeneous mixture of the contrast agent flowing through the arteries. This leads to heavily varying intensity values within the vessel regions as illustrated in Figure 3.1. In Figure 3.1 (a), a *final image* from Chapter 2 is shown which is partitioned into several mask regions (Figure 3.1 (b), (c) and (d)). The regions depicted in Figure 3.1 (c) and (d) are subregions of (b) and (c) respectively. For each region, the intensity mean and standard deviation are computed as statistical properties to mathematical describe the region dependent contrast agent concentration. Table 3.1 summerizes this statistical information and reveals that larger vessel regions exhibit larger deviations concerning mean and standard deviation than its corresponding smaller subregions. This varying contrast within the vessel regions may lead to wider edge ramps between vessel contour and background.

Table 3.1: Statistical overview about the individual vessel regions which are illustrated in Figure 3.1 (b), (c) and (d).

Level	Regions (Intensity mean$\pm\sigma$)					
1	Z					
	0.53± 0.013					
2	A	B	C	D	E	F
	0.62± 0.0004	0.61± 0.0001	0.63± 0.0001	0.54± 0.0012	0.22± 0.01	0.35± 0.005
3	D0	D1	D2			
	0.53± 0.0006	0.56± 0.0007	0.54± 0.0008			

Patient movement is another influence factor which often occurs during 2-D DSA acquisitions. This may lead to striking artifacts within vessel regions. Hence, global threshold segmentation will fail because it will not handle the heterogeneous intensity distribution within the vessel regions.

This chapter introduces a semi-automatic 2-D vessel segmentation technique based on local adaptive contrast enhancement. Hereby, the statistical stability within small vessel regions is utilized such that the intensity inhomogeneity can be equalized over the entire image. The algorithm is extensively evaluated using a database of 45 different DSA images.

3.2 Methods

The core idea of this segmentation approach is to place small boxes along the selected vessel branches and perform an intensity mapping of the pixel intensities within each box. Figure 3.2 schematically illustrates this approach. This is done because it is assumed that the local statistical properties within a box do not change significantly. The methodology part is composed as follows: first, a rudimental centerline computation approach is proposed that can handle cases where no 3-D centerline is available to be overlaid with the 2-D image. Second, the parameters are described to properly align the boxes along the centerline. The third part delineates the final segmentation step using the fast marching algorithm [Seth 99].

3.2.1 Centerline Generation for Semi-Automatic Application

If there is no centerline provided from a 3-D vessel segmentation method, manually selected seed points are placed along the vessel branches that should be segmented. Figure 3.2 (a) shows an example. These seed points are then connected by using a minimum-cost path approach where the 2-D DSA image is considered as a graph. Each pixel position denotes a node within this graph which is connected to its eight neighbors. Each node is associated with costs defined by the intensity value of the pixel position, i. e. pixels associated with darker intensities ex-

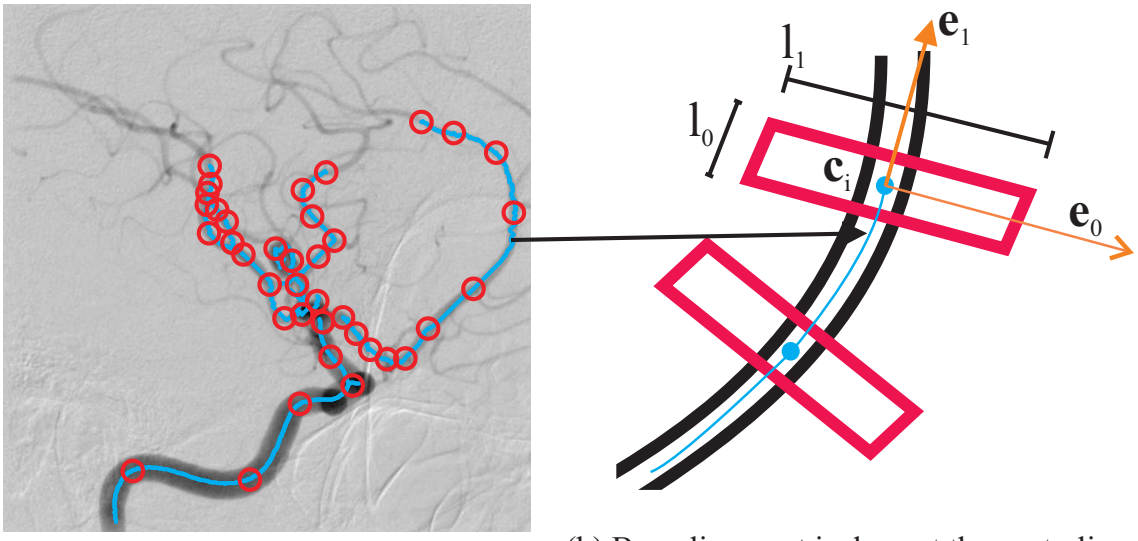

(a) Manually selected seed points illustrated in red.

(b) Box alignment is done at the centerline point c_i utilizing the Hessian-based eigenvectors $\mathbf{e}_0$ and $\mathbf{e}_1$. l_0 and l_1 denote the box length

Figure 3.2: (a) shows a set of manual placed seed points in order to compute the vessel centerline using a minimum cost path approach. (b) schematically illustrates the alignment of the boxes along the centerline together with its parameters.

hibit lower costs than brighter ones. Since all seed points are located within vessel branches, the minimum-cost path between two neighboring seed points proceeds within the vessel structure. Dijkstra's algorithm [Dijk 59] is used to compute this minimum-cost path resulting in a set of points $\boldsymbol{C}$ which is defined as follows:

$$\boldsymbol{C} = \{\boldsymbol{c}_i\}_{i=0}^{N-1} \tag{3.1}$$

where $\boldsymbol{c}_i \in \mathbb{R}^2$ denotes a point on the centerline path. This set forms the centerlines of the selected vessel branches. After centerline computation the noise within the 2-D DSA image is reduced in an edge-preserving manner. For that purpose, bilateral filtering [Toma 98] is applied.

3.2.2 Parameter Estimation for Local Box Alignment

For each centerline point $\boldsymbol{c}_i$, the following parameters have to be estimated such that the boxes can be placed in a perpendicular manner along the centerline:

- box orientation $\{(\boldsymbol{e}_{0,i}, \boldsymbol{e}_{1,i})\}_{i=0}^{N-1}$
- box length $\{(l_{0,i}, l_{1,i})\}_{i=0}^{1}$

where $\boldsymbol{e}_{0,i}$ and $\boldsymbol{e}_{1,i}$ denote the eigenvectors of the Hessian matrix. The first eigenvector $\boldsymbol{e}_{0,i}$ corresponding to the larger eigenvalue points across the vessel branch. The second eigenvector $\boldsymbol{e}_{1,i}$ is aligned in the direction of the centerline $\boldsymbol{e}_{0,i} \perp \boldsymbol{e}_{1,i}$. Figure 3.2 (b) illustrates the box related parameters together with the centerline.

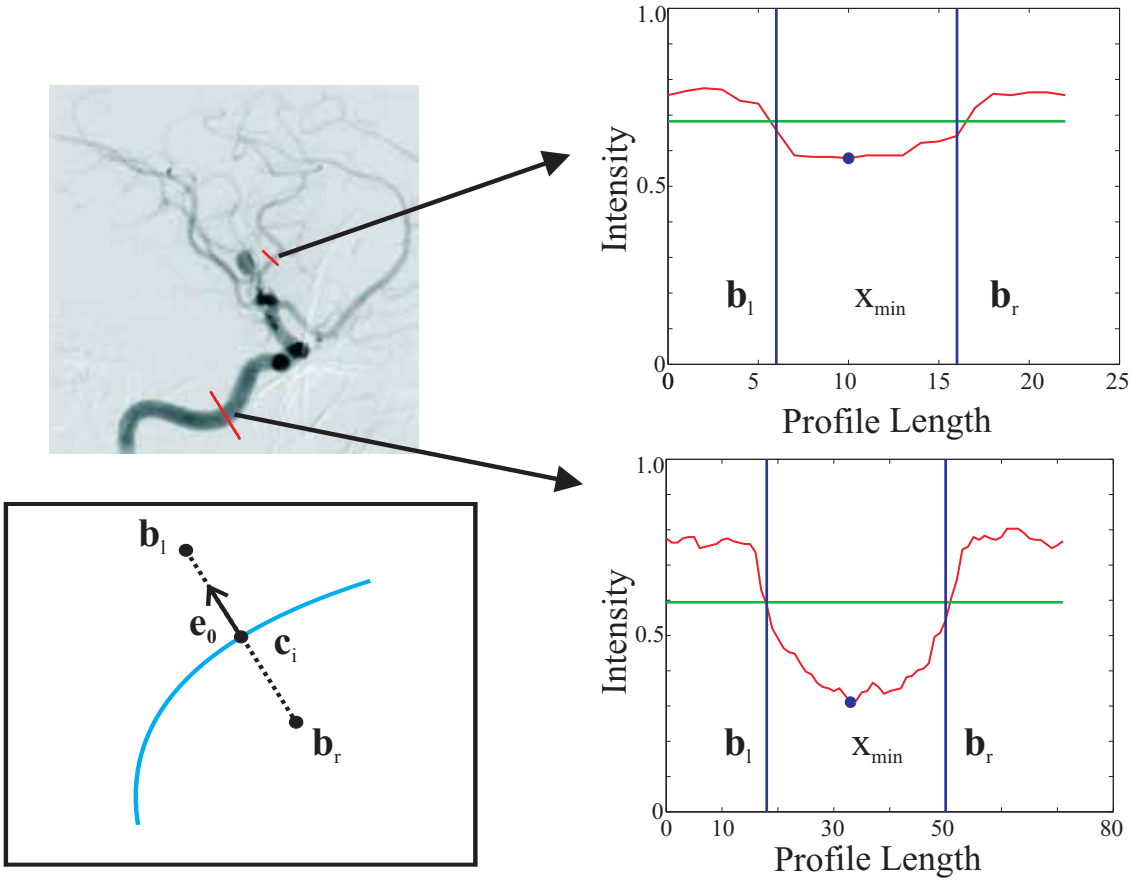

Figure 3.3: Vessel diameter estimation: top left shows a typical *final sum image* with 1-D intensity profiles (right column) measured at different vessel branches. The green line depicts the mean intensity value of the profile. The bottom left image schematically depicts a vessel centerline (blue) together with the vessel diameter estimation approach using the eigenvector $\boldsymbol{e}_0$.

Cross-sectional intensity profiles along $\boldsymbol{e}_{0,i}$ are used to determine the vessel diameter ξ and the box length $l_{1,i}$ as depicted in Figure 3.3. For each point $\boldsymbol{c}_i$ on the centerline, an intensity profile is computed in the direction of $\boldsymbol{e}_{0,i}$ using Bresenhams algorithm [Bres 65] to estimate the vessel diameter. Typical shapes of such intensity profiles are shown on the right of Figure 3.3 where the valley denotes the vessel and the two outer parts represent the image background. The mean intensity value of a profile (see Figure 3.3 green lines) defines the left and right border of the vessel branch, i. e. b_l and b_r. The vessel diameter ξ is now given as follows:

$$\xi = \begin{cases} 2(b_r - x_{\min}) & \text{, if } x_{\min} - b_l < b_r - x_{\min} \\ 2(x_{\min} - b_l) & \text{, otherwise} \end{cases} \tag{3.2}$$

where $x_{\min}$ denotes the lowest intensity value of the profile illustrated as blue dot in Figure 3.3. Hence, the box length $l_{1,i}$ across the vessel is the vessel diameter plus a certain offset such that the box certainly covers the underlying vessel branch. The box length $l_{0,i}$ in vessel direction is kept constant.

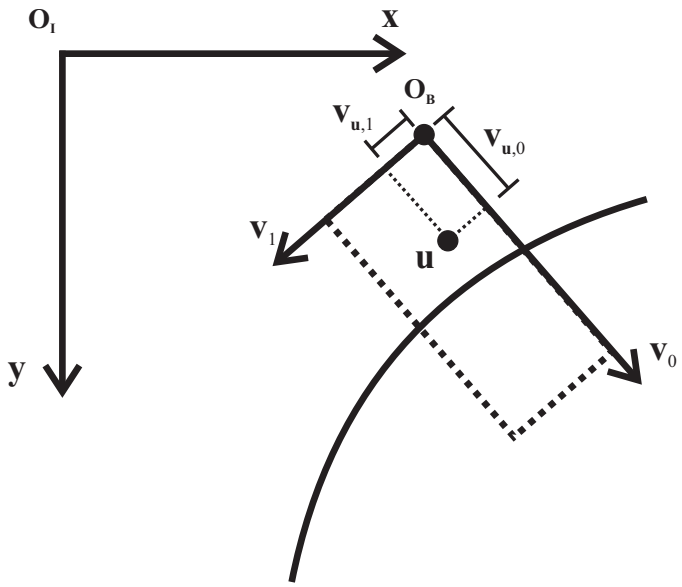

Figure 3.4: Each box coordinate system is aligned with the image coordinate system by an efficient coordinate transformation such that the pixel position belonging to the boxes can be easily computed.

3.2.3 Local Adaptive Contrast Enhancement

Since all box parameters are estimated properly, each box can now be associated with one sigmoid function S that is applied to perform the contrast enhancement by intensity mapping. S is defined as follows:

$$S(v(\boldsymbol{u}), \alpha, \beta) = \frac{1}{1 + e^{-\left(\frac{v(\boldsymbol{u}) - \beta}{\alpha}\right)}} \quad \alpha, \beta \in \mathbb{R}, \tag{3.3}$$

α and β denote the slope and translation of the sigmoid function, respectively. In our case, α is kept constant and β is controlled by the intensity mean of each box, i. e. a higher mean results in vessel segmentation showing thicker vessel diameters.

Since the boxes are perpendicularly aligned along the centerline, a coordinate transformation is applied to all boxes (see Figure 3.4) such that the box coordinate system becomes parallel to the image coordinate system. This coordinate transformation can be performed with matrix multiplications using homogeneous coordinates [Fole 97]. The origin of the box coordinate system $\boldsymbol{o}_B \in \mathbb{R}^2$ has to be translated into the origin of the image coordinate system $\boldsymbol{o}_I \in \mathbb{R}^2$ followed by a rotation such that both coordinate systems are aligned. The entire transformation can be expressed in matrix notation:

$$\begin{pmatrix} u_{I,1} \\ u_{I,2} \\ 1 \end{pmatrix} \cong \begin{pmatrix} \cos\eta & -\sin\eta & 0 \\ \sin\eta & \cos\eta & 0 \\ 0 & 0 & 1 \end{pmatrix} \cdot \begin{pmatrix} 1 & 0 & o_{I,1} - o_{B,1} \\ 0 & 1 & o_{I,2} - o_{B,2} \\ 0 & 0 & 1 \end{pmatrix} \cdot \begin{pmatrix} u_{B,1} \\ u_{B,2} \\ 1 \end{pmatrix} \tag{3.4}$$

where η denotes the rotation angle between the base vectors of the coordinate systems. This simplifies and accelerates the computation of the sigmoid function

(a) Enhanced vessel tree

(b) Top: original zoomed regions
Bottom: local adaptive enhancement

Figure 3.5: Examples of local contrast enhancement.

because the check whether a pixel position is inside a certain box can be described as:

$$\text{box}(\boldsymbol{u}_{O_I}) = \begin{cases} 1 & \text{, if } u_{o_I,1} \leq l_1 \wedge u_{o_I,2} \leq l_2 \\ 0 & \text{, otherwise} \end{cases} \tag{3.5}$$

3.2.4 Segmentation and Postprocessing

The local adaptive contrast enhancement has compensated almost the majority of all inhomogenity originating from the unequal mixture of the contrast agent as illustrated in Figure 3.5. However, there might still be a few areas where the local contrast enhancement led to inadequate results (see the circle in Figure 3.5 (a)). Therefore, the final segmentation result is computed by combining the contrast enhanced image with the bilateral filtered image using the minimum operator, i. e.

$$v_{\text{seg}}(\boldsymbol{u}) = \begin{cases} 0 & \text{, if } \min(v_{\text{contrast}}(\boldsymbol{u}), v_{\text{bilateral}}(\boldsymbol{u})) < 0.5 \\ 1 & \text{, otherwise} \end{cases} \tag{3.6}$$

where $v_{\text{seg}}(\boldsymbol{u})$, $v_{\text{contrast}}(\boldsymbol{u})$ and $v_{\text{bilateral}}(\boldsymbol{u})$ denote the intensity value at position $\boldsymbol{u}$ of the segmentation, contrast enhanced and bilateral filtered image respectively. Since our contrast enhancement is based on boxes, small isolated artifacts appear in the vicinity of the vessels. To remove these artifacts the binary image is skeletonized. Each skeleton part has to exhibit a minimum number of points. Otherwise they are removed. The entire algorithm (Program 3.1) is presented in pseudo code below.

3.3 Evaluation and Results

This semi-automatic 2-D vessel segmentation approach is extensively evaluated using a database of 45 studies ($\{\mathcal{K}_i\}_{i=1}^{45}$). This database splits up into two subsets,

Program 3.1: 2-D vessel segmentation algorithm

Input: $\mathcal{K}_{\text{F,SUM}}$, $\mathcal{K}_{\text{F,MIN}}$ or $\mathcal{K}_{RE}$
Output: Binary vessel segmentation image
begin
  $I_{\text{BF}} \longleftarrow$ perform bilateral filtering
  `// Initialization`
  if *3-D centerline available* **then**
    perform forward projection
  else
    place manual seed points along the vessels to be segmented
    seed point are connected to centerline using Dijkstra's algorithm
  end
  `// Box parameter estimation for each centerline point`
  $\boldsymbol{P} \longleftarrow \emptyset$ `// holds all box parameters`
  while $\boldsymbol{C} \neq \emptyset$ **do**
    take centerline point $\boldsymbol{c}_i$ and remove it from $\boldsymbol{C}$
    compute Hessian matrix at position $\boldsymbol{c}_i$ and estimate vessel diameter
    $\boldsymbol{p}_i \longleftarrow (\boldsymbol{e}_{0,i}^T, \boldsymbol{e}_{1,i}^T, l_{0,i}, l_{1,i})$
    align box according to $\boldsymbol{e}_{0,i}$ and $\boldsymbol{e}_{1,i}$)
    $\boldsymbol{P} \longleftarrow \boldsymbol{P} + \boldsymbol{p}_i$
  end
  `// Local adaptive contrast enhancement`
  foreach $\boldsymbol{p}_i \in \boldsymbol{P}$ **do**
    $\beta \longleftarrow$ mean intensity of box $\boldsymbol{p}_i$
    $\alpha \longleftarrow$ constant value
    setup sigmoid function $S(v(\boldsymbol{u}), \alpha, \beta)$
    contrast enhancement within box $\boldsymbol{p}_i$ by applying sigmoid function S
  end
  $I_{\text{LE}} \longleftarrow$ store local contrast enhanced image
  `// Segmentation`
  $I_{\text{Final}} \longleftarrow \min(I_{\text{LE}}, I_{\text{BF}})$
  apply fast marching algorithm on I_{Final}
end

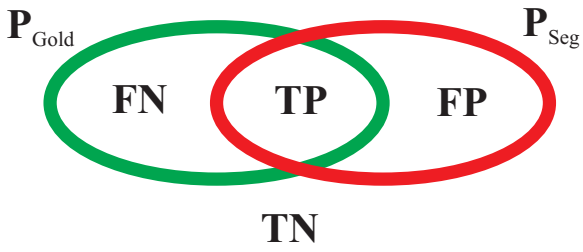

Figure 3.6: Illustration of TP, TN, FP and FN; green set: goldstandard vessel pixels, red set: vessel pixels of the 2-D DSA segmentation result.

i. e. 18 DSA images were generated using the classification-based DSA summation method introduced in Chapter 2 and 27 DSA images originate from three sets of DSA projections which are used for 3-D DSA reconstruction called $\mathcal{K}_{RE}$. Per set, nine 2-D DSA images were extracted. The entire database was acquired at the Department of Neuroradiology (University Hospital Erlangen, Germany) using a Siemens C-arm system (AXIOM Artis dBA, Siemens Healthcare Sector, Forchheim, Germany). The x/y dimension of the images varied between 512×512 and 1440×1440. The pixel spacing in x/y was $0.154/0.154$ mm concerning the studies $\mathcal{K}_1$ to $\mathcal{K}_{18}$ and $0.308/0.308$ mm for $\mathcal{K}_{19}$ to $\mathcal{K}_{45}$. Gold standard vessel segmentations were performed for each study by manual outlining of the selected vessel branches. These gold standard segmentations were approved by a neuroradiologist.

3.3.1 Methods of Evaluation

Two measurements are used to quantitatively evaluate the proposed 2-D vessel segmentation algorithm, i. e. the Hausdorff distance and the sensitivity.

There are two sets of binary images during the evaluation, i. e. the gold standard $\boldsymbol{P}_{\text{Gold}}$ and the computed segmentation result $\boldsymbol{P}_{\text{Seg}}$. The Hausdorff distance between two sets is defined as:

$$d_{\text{H}}(\boldsymbol{P}_{\text{Gold}}, \boldsymbol{P}_{\text{Seg}}) = \max(h(\boldsymbol{P}_{\text{Gold}}, \boldsymbol{P}_{\text{Seg}}), h(\boldsymbol{P}_{\text{Seg}}, \boldsymbol{P}_{\text{Gold}})) \tag{3.7}$$

$$\text{where } h(\boldsymbol{P}_{\text{Gold}}, \boldsymbol{P}_{\text{Seg}}) = \max_{\text{u}\in\text{P}_{\text{Gold}}} \min_{\text{u}\in\text{P}_{\text{Seg}}} \left\| \boldsymbol{u}_{\boldsymbol{P}_{\text{Gold}}} - \boldsymbol{u}_{\boldsymbol{P}_{\text{Seg}}} \right\|_2 \tag{3.8}$$

where $h(\boldsymbol{P}_{\text{Gold}}, \boldsymbol{P}_{\text{Seg}})$ represents the directed Hausdorff distance. The Hausdorff distance is a good indicator in terms of whether there are outliers within the segmentation result. Comparing two sets of pixels, it takes the furthest point of a set which one can be to the closest of the other set. The lower the Hausdorff distance gets, the better the segmentation result will be.

The sensitivity denotes the second evaluation measurement which is categorized as a statistical measure of a binary classification test. It requires to count the following numbers given the vessel segmentation result and the gold standard segmentation:

- True positive (TP): vessel pixels being correctly classified as vessels

- True negative (TN): background pixels being correctly classified as background
- False positive (FP): background pixels being falsely classified as vessels
- False negative (FN): vessel pixels being falsely classified as background

The relationship of these number are schematically illustrated in Figure 3.6. The sensitivity is defined as:

$$d_{\mathrm{SE}} = \frac{\#\mathrm{TP}}{\#\mathrm{TP} + \#\mathrm{FN}} \tag{3.9}$$

This measurement gives a good impression about the overall fit of the computed segmentation result with the gold standard segmentation set. The sensitivity becomes maximum, i. e. $d_{\mathrm{SE}} = 1$ if all actual vessel pixels are correctly segmented within the segmentation result.

3.3.2 Experimental Results

This section describes the segmentation results concerning two different types of DSA images, i. e. 2-D DSA series showing the blood flow through the arteries which were preprocessed leading to a *final image* in Chapter 2 and 2-D DSA images taken for 3-D vessel reconstruction purposes. All experiments were conducted on an AMD Athlon 7750 Dual-Core, 1.38 GHz with 3 GB of main memory. Our approach is implemented in C++. On average, the segmentation takes 5 seconds. The number of manual selected seed points varied from 10 to 30 depending on the number, length and shape of the vessel branches in case there was no 3-D projected centerline given.

Table 3.2 gives a quantitative insight of the segmentation results concerning both types of 2-D DSA images. A mean Hausdorff distance and sensitivity of 22 pixels $\pm$5.6 and 0.89$\pm$0.02 could be respectively achieved regarding the *final sum images* (see Table 3.2 left columns). The segmentation results for the DSA images taken from the reconstruction set revealed an average Hausdorff distance of 22 pixels $\pm$6.4 and sensitivity of 0.90$\pm$0.05. The sensitivity values indicate promising segmentation results.

Figures 3.7, 3.8 and 3.9 illustrate qualitative segmentation results. Figure 3.7 shows the segmentation results for the *final sum images* and Figure 3.8 depicts the results concerning DSA images acquired for reconstruction. In both Figures, the difference images reveal that this segmentation approach slightly underestimates the vessel diameters. In Figure 3.9, centerlines are shown in red on 2-D DSA images which were forward projected from a corresponding 3-D segmentation. This centerline forward projection automatically selects the vessel branches to be segmented and initializes the entire segmentation approach.

3.4 Discussion

Our local adaptive contrast enhanced vessel segmentation algorithm has shown to properly handle the intensity variation within vessel regions to perform a smooth

Table 3.2: The left three columns depict the results regarding the *final sum images* and the three right columns show the results of the segmentation algorithm concerning DSA images taken from the set of projections $\mathcal{K}_{RE}$ used for 3-D DSA reconstruction.

Final Sum Images			DSA Images from Recon. Set		
$\mathcal{K}_{\mathrm{F,SUM}}$[index]	d_{H} [pixels]	d_{SE}	$\mathcal{K}_{RE}$ [index]	d_{H} [pixels]	d_{SE}
1	12.0	0.892	0 - 0	21.9	0.823
2	24.0	0.873	0 - 1	22.0	0.839
3	32.2	0.868	0 - 2	18.7	0.868
4	23.6	0.874	0 - 70	15.8	0.867
5	20.0	0.891	0 - 71	20.1	0.885
6	22.3	0.917	0 - 72	17.3	0.798
7	20.2	0.872	0 - 130	43.6	0.882
8	18.0	0.899	0 - 131	16.3	0.901
9	15.8	0.880	0 - 132	19.0	0.897
10	26.1	0.916	1 - 0	32.7	0.797
11	22.8	0.860	1 - 1	19.0	0.798
12	20.1	0.919	1 - 2	13.5	0.865
13	32.2	0.900	1 - 70	17.3	0.910
14	23.2	0.910	1 - 71	22.0	0.919
15	18.0	0.875	1 - 72	18.4	0.919
16	32.6	0.837	1 - 130	19.0	0.947
17	22.2	0.908	1 - 131	18.8	0.964
18	18.6	0.898	1 - 132	32.0	0.980
			2 - 0	17.0	0.937
			2 - 1	23.4	0.957
			2 - 2	25.5	0.962
			2 - 42	21.0	0.913
			2 - 43	22.0	0.912
			2 - 44	17.0	0.910
			2 - 98	23.0	0.892
			2 - 99	29.2	0.967
			2 - 100	22.8	0.907
Mean	22.5	0.888		21.8	0.897
σ	5.6	0.022		6.4	0.053

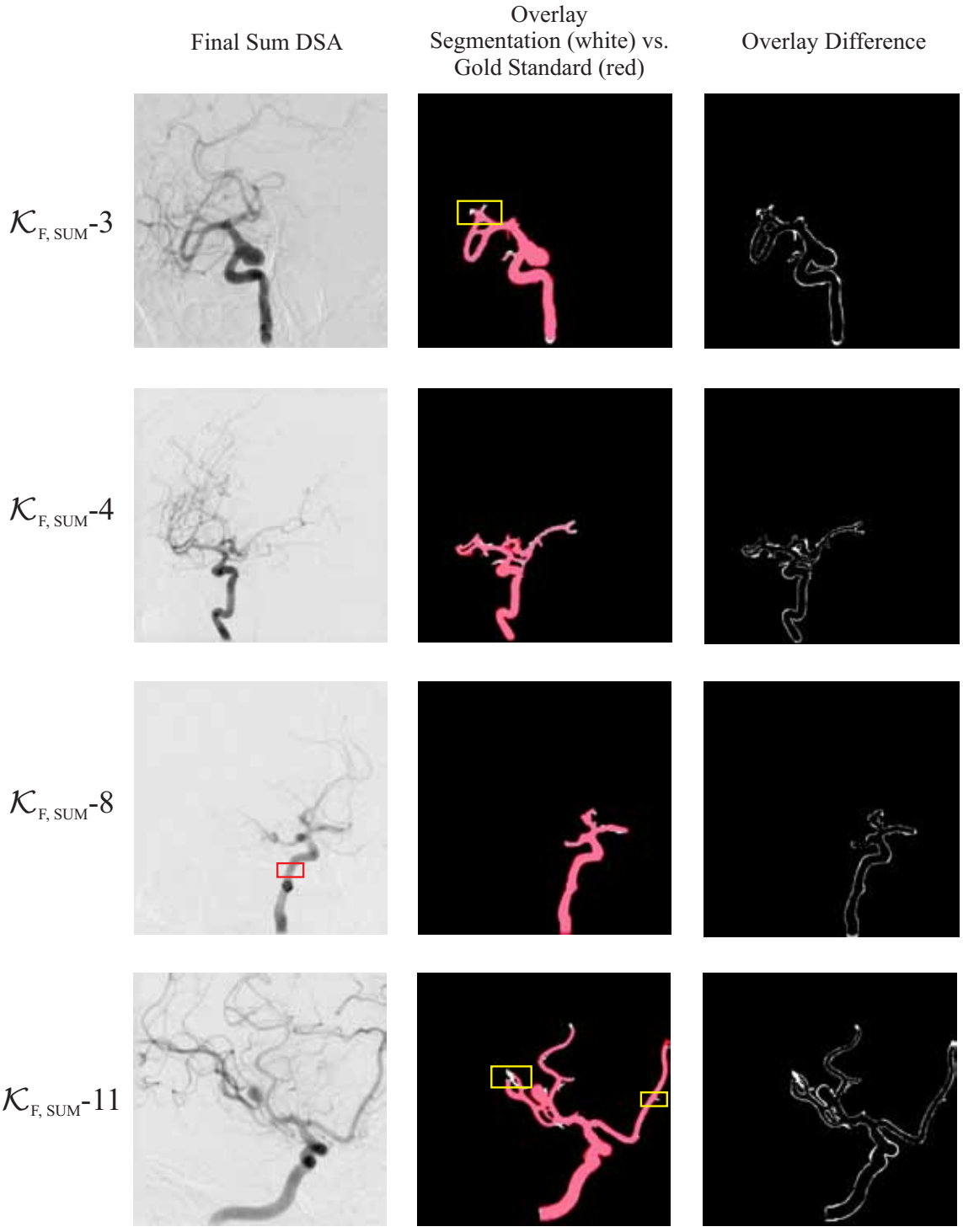

Figure 3.7: Qualitative evaluation results concerning *final sum* DSA images. Left column represents the input image and the middle column depicts the overlay between segmentation (white) and gold standard (red). The right column shows the difference between segmentation and gold standard.

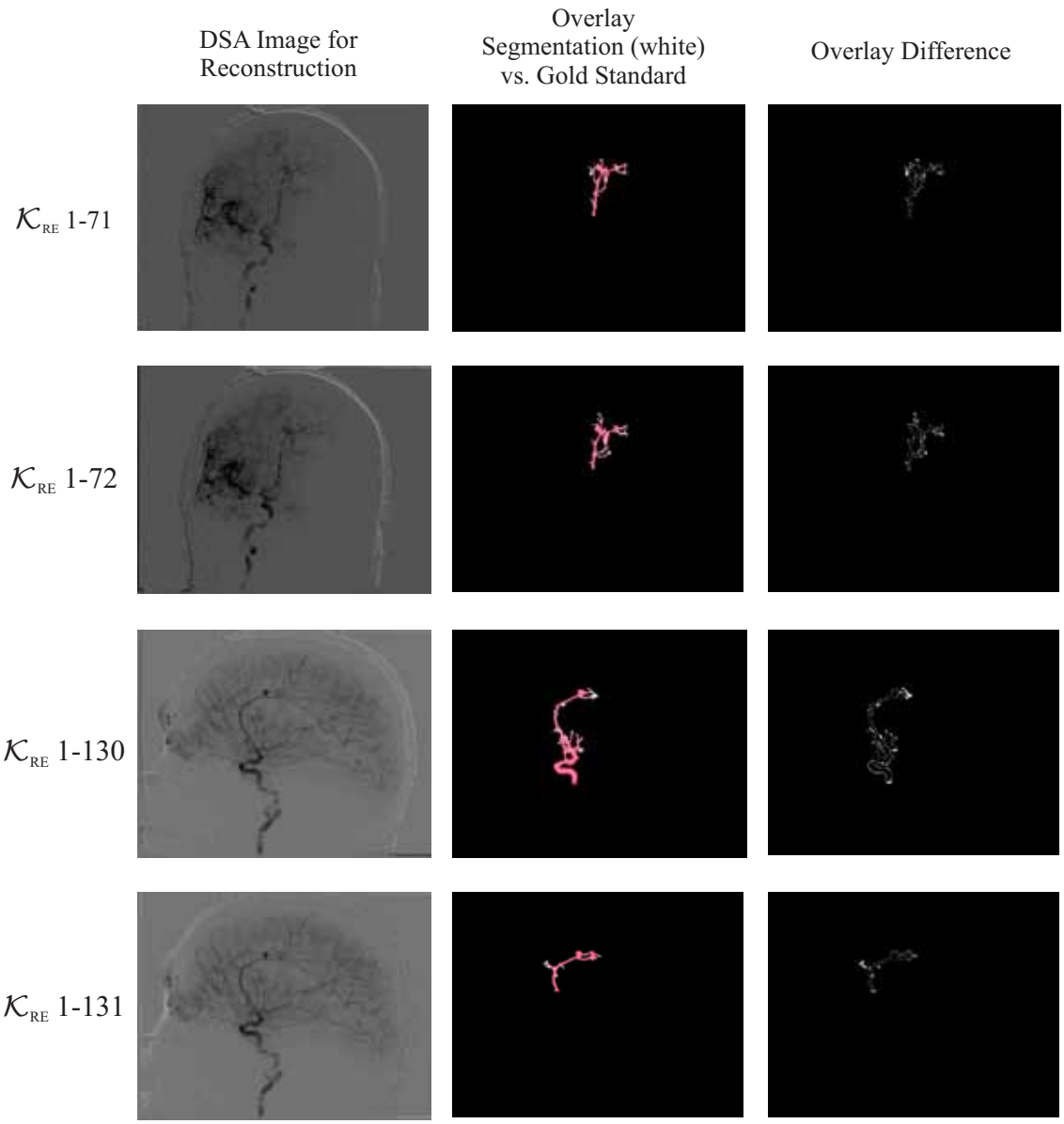

Figure 3.8: Qualitative evaluation results concerning DSA images acquired for reconstruction. Left column represents the input image and the middle column depicts the overlay between segmentation (white) and gold standard (red). The right column shows the difference between segmentation and gold standard.

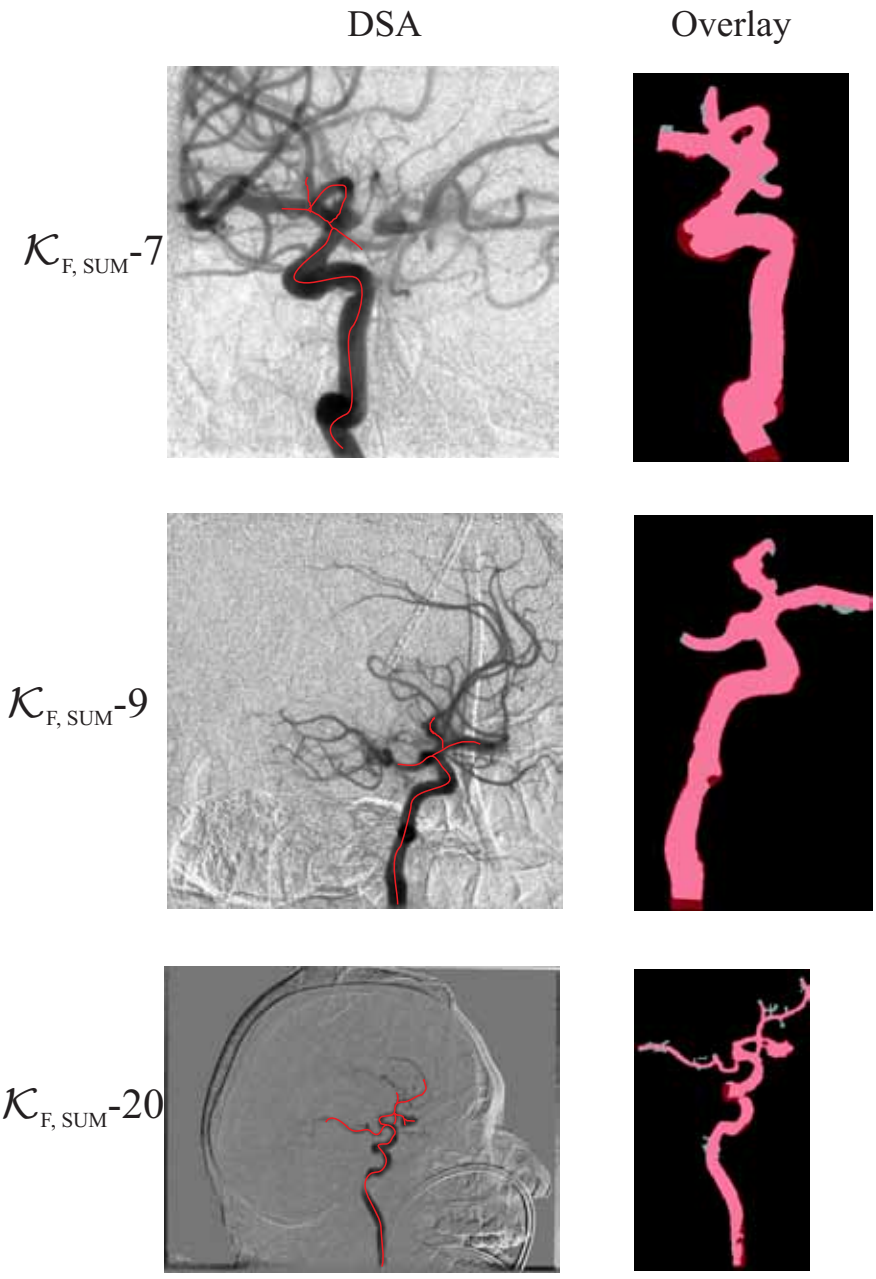

Figure 3.9: Segmentation results for study number 7, 9 and 20. Left column depicts the original 2-D DSA images. Right column shows the corresponding gold standard segmentations (red) and our segmentation results (gray) as overlay. The red line represents the centerline defining the vessels of interest.

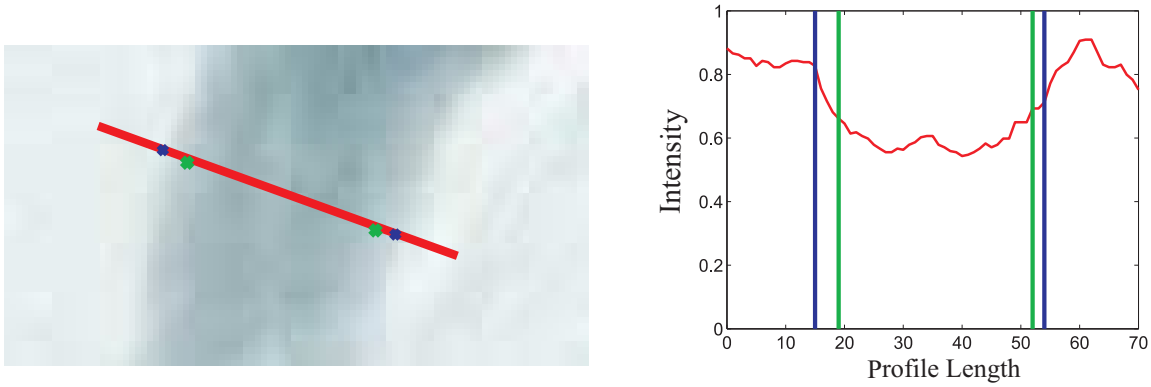

(a) Profile line (b) Intensity profile

Figure 3.10: Comparison of segmentation result and goldstandard segmentation; (a) region of interest of a smoothed DSA image, red line: profile, blue crosses: goldstandard segmentation border, green crosses: segmentation result border; (b) profile of the red line in (a); borders of the segmentations are denoted by the lines (same color mapping as in (a)).

segmentation using threshold image filtering. The extensive evaluation demonstrates that our approach is clinical applicable and able to come up with quantitative measurements during diagnosis and treatment planning.

When taking a closer look at the qualitative segmentation results (see Figure 3.7 and 3.8), there are two drawbacks concerning this segmentation methodology which are discussed below: 1) vessel diameter underestimation and 2) segmentation of the beginning of vessel branches.
The reason why this approach underestimates the vessel diameter can be easily explained using Figure 3.10 which shows a zoomed vessel region of $\mathcal{K}_{\text{F,SUM}}$-8 (see yellow box in Figure 3.7). An intensity profile (see Figure 3.10 (b)) is taken along the red line in Figure 3.10 (a) which is perpendicular to the vessel. The blue points denote the border of the gold standard segmentation and the green points indicate the segmentation boundary computed by our segmentation approach. The discrepancy originates from the gradient of the intensity values near the edge between vessel structure and background. This is illustrated by the blue and green bars in Figure 3.10 (b). The vessel boundary detection is heavily influenced by the mean intensity value of the current box as depicted in Figure 3.3 which controls the sigmoid function mapping the intensities to bright and dark pixels respectively. Two approaches might be possible to handle this issue: The first would be to adaptivly enlarge the box size l_0 and l_1 such that more brighter background pixels are covered and the mean intensity of the box is increased. This makes a right shift to the corresponding box sigmoid function mapping more intensities to darker pixel values. The second approach would be to simply take the mean intensity plus a certain offset. Both approaches will lead to a final segmentation result showing the vessels being segmented in thicker way.

The mean Hausdorff distance concerning both DSA image types revealed 22 pixels. This number indicates that the segmentation results exhibit a few outliers. The reason of these outliers is the box-based contrast enhancement along the ves-

sel centerline. At locations where small vessels are branching, these boxes cover the area of bifurcation. Hence, the beginning of these small vessels are contrast enhanced as well such that they are segmented in the end. The yellow boxes in Figure 3.10 highlights this phenomenon. To remove these outliers, one possible approach would be to perform a skeletonization of the segmentation result and compare it with the 2-D centerlines. Branches which are not part of the centerlines will be deleted.

3.5 Conclusion

This chapter has presented a 2-D vessel segmentation approach which overcomes the challenge of inhomogenous contrast agent distribution. The major contribution of this work denotes the local adaptive contrast enhancement performed by a set of individual boxes along a given centerline. The clinical applicability of this segmentation approach is ensured by the evaluation of 45 different 2-D DSA patient datasets. Within the next two chapters, we will see how this 2-D vessel information is incorporated into the 3-D vessel segmentation methodology based on 3-D DSA volumes. The 2-D segmentation results will serve as gold standard to validate and adapt initial 3-D vessel segmentation results.

Part II

3-D Vessel Segmentation

CHAPTER 4

Statistical Thresholding for Centerline Computation using Prior Knowledge

This chapter introduces two pre-processing steps which are necessary for the subsequent 3-D vessel segmentation method introduced in Chapter 5. The first step proposes a local adaptive statistical threshold segmentation approach utilizing the prior knowledge about the intensity composition of cerebral and cardiac 3-D rotational angiography data (3-DRA), i. e. three intensity classes: background (low intensities), artifacts (middle to high intensities) and vessel structures (highest intensities). Voxel positions associated with the highest intensity values are randomly drawn to locally model the intensity distribution within small boxes using GMMs. The mean value of all box histogram estimations is taken as statistical threshold value which results in a thresholded volume exhibiting medium and large vessels.

The second step denotes the computation of vessel centerlines which is a challenging task due to various imaging artifacts like inhomogeneous contrast agent distribution, beam hardening and vessel movement. This partially leads to an uncertainty about the actual centerline path. The centerline method, introduced in this Chapter, is mainly based on graph related multi-scale medialness measure (MM) costs [Guel 08] combined with an extension which regularizes the centerline path within uncertain vessel regions. The extension is an additional cost term computed from the distance map of the skeletonized thresholded volume. The centerline algorithm has shown to be powerful within a clinical setup and is extensively evaluated on 15 cerebral and 13 coronary 3-DRA datasets. The quantitative evaluation shows a mean distance of 0.42 mm against a pure MM driven centerline

approach. The qualitative assessment performed by medical experts reveals that our centerline paths better fit the actual vessel center-axis.

4.1 Motivation

Vessel quantification represents a key step in an interventional angio suite within neuroradiology and cardiology to perform diagnosis and treatment planning. The extraction of vessel centerlines delivers a major support for endovascular interventions [Subr 04] by enabling clinicians to browse through vessel branches with a plane which is perpendiculary aligned to the centerline axis. Quantitative vessel measurements like diameters, stenosis degree or aneurysm neck sizes may be fade in on this plane to provide instant information for the therapy planning, e. g. stent placement or coil embolization.

Since motion-compensated interventional cardiac reconstruction [Rohk 10a], [Rohk 10b] delivers 3-D volumes exhibiting vessel branches of high quality, vessel related post-processing algorithms come into a feasible range for cardiac applications. Nevertheless, accurate centerline modeling still denotes a challenging task due to inhomogeneous distribution of contrast agent, kissing vessels, vessel motion, interrupted and multi-scale vessel branches and the presence of pathologies like stenosis or aneurysms. This chapter proposes an integrated clinical method to compute vessel centerlines of 3-DRA concerning cerebral and coronary vessels obtained from motion compensated cardiac reconstructions as shown in Figure 4.1 (left column). GMMs are applied to locally model the a priori known intensity classes (background, artifacts and vessel structure) of 3-DRA yielding a thresholded 3-D volume (Figure 4.1, middle column). This volume is skeletonized to compute a distance map which extends the MM-based cost function [Tyrr 07], [Guel 08] such that the minimum-cost driven centerline algorithm becomes more robust against imaging artifacts and motion corrupted elliptical-shaped vessel structures. The evaluation of our centerline algorithm comprises a quantitative comparison against the pure MM approach from [Guel 08]. The qualitative assessment reveals that our approach matches better the actual vessel center-axis especially for large vessel branches with heterogeneous contrast agent distributions or motion influence. The clinical applicability is ensured by an evaluation database of 28 different 3-DRA datasets, i.e. 15 cerebral vessel and 13 coronary datasets.

4.2 Related Work

During the last decade, various approaches have been developed to extract the vessel centerline. In [Lesa 09], the centerline techniques are divided into three major methodology categories, i. e. (1) direct centerline tracking, (2) model-based optimization and (3) minimal path techniques. Almost all approaches have in common that they work as semi-automatic algorithms requiring one or two seed points in between the vessel centerline will be computed.

Direct centerline tracking methods often make use of estimating the vessel direction using a Hessian-based optimization to get local geometric features [Aylw 02].

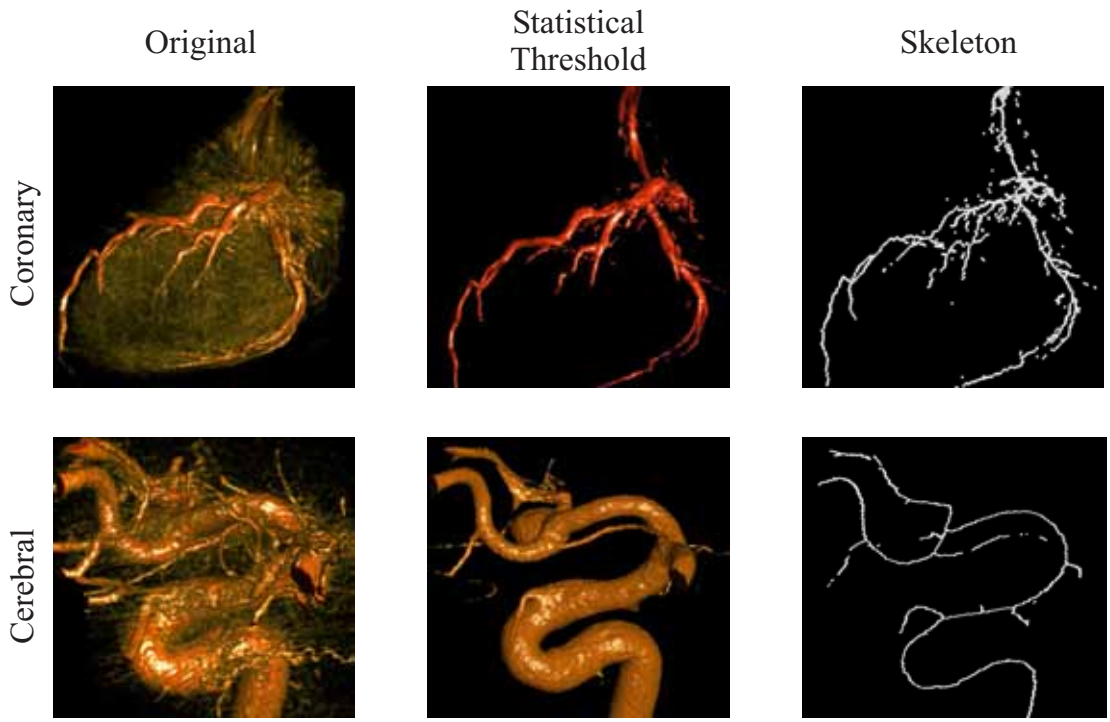

Figure 4.1: Reconstructed 3-D images (left) are segmented using statistical thresholding (middle) and skeletonized (right).

Kalman filtering has been applied by [Gong 03, Woer 07] to predict the pass of vessel branches. Another direct tracking approach uses sphere-based geometric recentering techniques combined with local thresholding [Hern 06]. Also 2-D cross-sectional planes have been computed to predict the centerline direction and path [Tek 01].

Model-based centerline optimization denotes a small category within the centerline literature. In [Fran 99, Wong 06], B-spline and cardinal spline deformable models have been applied to balance between data and model-related energy optimization.

Minimum-path related techniques represent the most popular centerline computation technology because of its computational efficiency. The image is considered as a graph which allows to associate costs to each pixel or voxel. Path optimizations w.r.t. different norms (L_1, L_2 or L_∞) have been developed. Dijkstra related path findings denotes one example for L_1 path optimization [Olab 03, Guel 08]. The centerline computation regarding L_2 is associated with slightly higher computational efforts using fast marching algorithms [Law 00, Desc 01]. The fuzzy connectness technique [Udup 02] and region growing methods [Yim 03] are used to optimize the vessel centerline according to the L_∞ norm. L_∞ means that the total costs of a path corresponds to its worst edge, i. e. lowest degree of connectivity. Complete vessel tree extraction with one seed point, however, has not been extensively evaluated yet. A proper choice is the usage of termination criterions [Guel 08] which are controlled by heuristical thresholds such that first the entire

vessel tree is explored and second multiple paths are backtraced towards one root seed point.

4.3 Methods

4.3.1 Statistical Thresholding using Prior Knowledge

3-D rotational angiography is based on the direct intra-arterial injection of contrast agent. Due to the high contrastation, it can be assumed a priori that the vessels appear in the highest intensity bins of the histogram. Thus, 3-DRA datasets consist of three different types of intensity classes ω_i , i.e. foreground (vessels), artifacts and background which are locally modeled by GMMs [Huan 08]. The concept of locality is obtained by taking a set of voxel positions $\boldsymbol{B} = (\boldsymbol{b}_0, \boldsymbol{b}_1, ..., \boldsymbol{b}_{N-1}) \in \mathbb{R}^{3\times N}$ associated with the highest intensity values, i.e. the probability is very high to be at or nearby the vessels of interest. Each box is defined as set of neighboring voxels being defined as : $\boldsymbol{V}(\boldsymbol{b}_j) = \left\{ \boldsymbol{x} \in \mathbb{R}^3 : \left\| \boldsymbol{x} - \boldsymbol{b}_j \right\|_\infty < s \right\}$ where s denotes the box size. $M < N$ positions $\boldsymbol{b}_j$ are randomly drawn which are used as centers for local vessel histogram boxes. The intensities $f(\boldsymbol{x})$ at voxel positions $\boldsymbol{x}$ within j^{th} box are characterized by the probability density function $p(f(\boldsymbol{x})|\Theta_j)$ being a convex combination of K Gaussians:

$$p(f(\boldsymbol{x})|\Theta_j) = \sum_{i=0}^{K-1} p(f(\boldsymbol{x}), \mu_i, \sigma_i^2) P(\omega_i) \tag{4.1}$$

where $P(\omega_i) > 0$ denotes the class prior probability with the constraint $\sum_{i=0}^{K-1} P(\omega_i) = 1$. $\Theta_j \in \mathbb{R}^{3\times K}$ represents the box related parameter vector holding $P(\omega_i)$, μ_i and σ_i. All box parameters are concatenated within a matrix $\Theta = (\Theta_0, \Theta_1, ..., \Theta_{M-1}) \in \mathbb{R}^{3\times K\times M}$. The intensities are assumed to be independent and the joint density becomes maximum if the product of the probabilities of finding an intensity at each observed voxel position $\boldsymbol{x}$ is maximum. The optimization covering all box estimations is given by

$$\begin{aligned} \widehat{\Theta}_j &= \arg\max_{\Theta_j} \sum_{\boldsymbol{x}\in\boldsymbol{V}(\boldsymbol{b}_j)} \ln p(f(\boldsymbol{x})|\Theta_j) + \lambda \left(\sum_{i=0}^{K-1} P(\omega_i) = 1 \right) \\ \forall \Theta_j : j &= \{0, 1, ..., M-1\} \\ \overline{\Theta}_{\text{mean}} &= \frac{1}{M} \sum_{j=0}^{M-1} \widehat{\Theta}_j \end{aligned} \tag{4.2}$$

$\overline{\Theta}_{\text{mean}}$ represents the mean parameter vector for all boxes. The parameter estimation is performed by the Expectation-Maximization-Algorithm [Demp 77]. K is set to three because of the three different intensity classes. We set the final statistical threshold to the average of the two largest mean values because we want to remove the background and preserve the medium and major vessel structures. Figure 4.1 (middle and right column) depicts the thresholded results and the subsequently performed skeletonization [Lee 94].

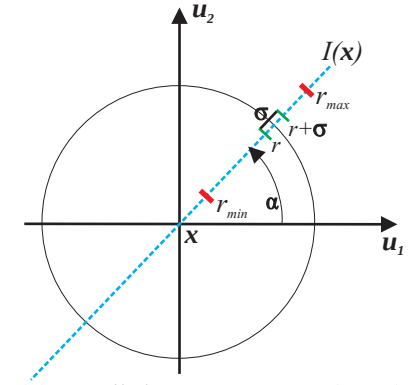

(a) Medialness measure (MM) principal

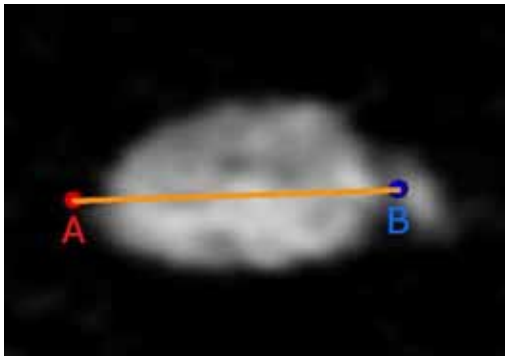

(b) Elliptical-shaped vessel

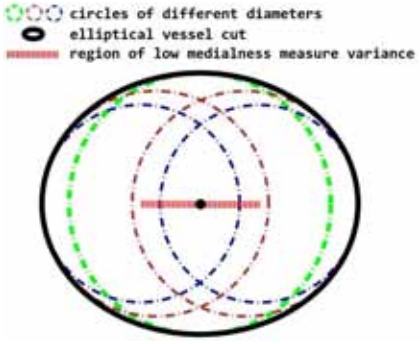

(c) Different circles fit to an elliptical-shaped vessel delivering similar MM responses

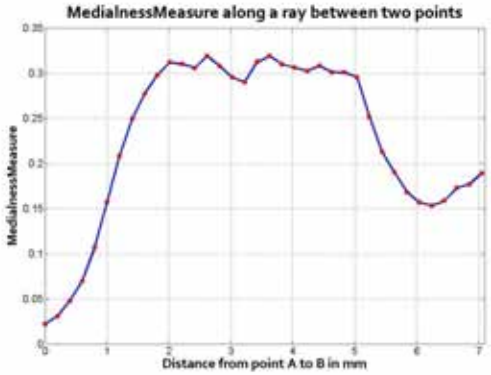

(d) MM profile acquired for points between A and B

Figure 4.2: (a) shows the principal of the medialness measure (MM). (b), (c) and (d) illustrate the behavior of the MM filter response for elliptical-shaped vessels.

4.3.2 Medialness Measure

This part gives a short overview about the medialness measure (MM) introduced by [Guel 08] describing a well established filtering technique to judge about the circularity of the underlying structure. For the remainder of the paper, the intensities of the 3-DRA datasets are normalized between zero and one. As illustrated in Figure 4.2 (a), it works with rotating rays and 1-D intensity profiles to determine the vessel boundary w.r.t different radii. The total MM function is defined as

$$M(\boldsymbol{x}) = \max_{r \in \{r_{\min},\ldots,r_{\max}\}} \frac{1}{Q} \sum_{i=0}^{Q-1} E(\boldsymbol{x} + r \cdot \boldsymbol{z}(2\pi i/Q)) \tag{4.3}$$

where Q denotes the number of rays and r limits the elongation of the ray. $\boldsymbol{z}(\alpha) = \cos\alpha \cdot \boldsymbol{z}_1 + \sin\alpha \cdot \boldsymbol{z}_2$ describes the normalized direction vector of the ray. As follows, we discuss this concept for a single ray $I_{r,\alpha} = I(\boldsymbol{x} + r \cdot \boldsymbol{z}(\alpha))$ which returns

the intensity value $I_{r,\alpha}$ at all positions r along the ray. The concept of a ray is utilized to compute a vessel boundary measure along a ray given by

$$A(t) = \max \left\{ \left| \frac{\partial}{\partial r} \left(g_\sigma \star I_{r,\alpha} \right) \right| \right\}_{r=t} \cdot \operatorname{sign} \left(\frac{\partial}{\partial r} \left(g_\sigma \star I_{r,\alpha} \right) \right) \tag{4.4}$$

where σ denotes the standard deviation of the Gaussian convolution. The sign function becomes negative if the current gradient indicates a falling edge, i.e. from high intensity values to low intensity values and vice versa. The entire edge response for a certain ray $I_{r,\alpha}(\boldsymbol{x})$ is now computed by

$$E(\boldsymbol{x} + r \cdot \boldsymbol{z}(\alpha)) = \max \left[-A(r) - A_{\mathrm{SR}}, \epsilon \right] \tag{4.5}$$

where A_{SR} describes the strongest rising edge observed along the ray. ϵ denotes a constant which is almost zero to avoid the singularity effect in voxel-based cost function e. g. 4.6. The MM function Eq. 4.3 becomes maximum if the position $\boldsymbol{x}$ is at the center of a vessel and r is chosen such that it exactly hits the vessel boundary position, i.e. A_{SR} reveals a small value since only one falling edge has been observed along the rays. The MM value represents one part of the voxel-based cost function. Section 4.3.3 introduces the second part of the cost function regularizing the MM function.

4.3.3 Distance Map as Regularizer

Although the medialness filtering is a robust technique to effectively compute the circularity of objects, there are several factors like unequal contrast agent distribution particularly within thick vessel branches or elliptical shaped vessel structures limiting the filter response of the MM. Especially elliptical shaped vessels lead to a MM response which exhibits a wide plateau due to the fact that the edge response from Eq. 4.5 delivers similar results regarding different vessel radii as illustrated in Figure 4.2 (b), (c) and (d). Based on pure MM costs, Dijkstra's shortest path algorithm [Dijk 59] may not pass through the actual vessel center axis. We propose to regularize the MM cost function with the incorporation of the distance map computed from the statistical thresholding result (section 4.3.1) to overcome these limitations. Our cost function per voxel is now defined as follows:

$$\Gamma(\boldsymbol{x}) = \frac{1}{(M(\boldsymbol{x}))^2} + \alpha \cdot \mathrm{dist}(\boldsymbol{x}) \tag{4.6}$$

where $\mathrm{dist}(\boldsymbol{x})$ denotes the skeleton-based Euclidian distance function and α a weighting factor. A polynomial cost function is used because the range of values are within a certain bandwidth and the computation time is reduced w.r.t. interventional applicability. Figure 4.3 shows an example of a distance map and the differences between the pure MM and distance map regularized costs. The lowest costs are clearly concentrated within the center of the vessels (Figure 4.3 compare yellow circles) where the pure MM reveals a blurred cost distribution. Hence, our proposed regularization attracts the minimum-cost path algorithm towards the actual vessel center axis. The impact of the distance function, however, has to be limited

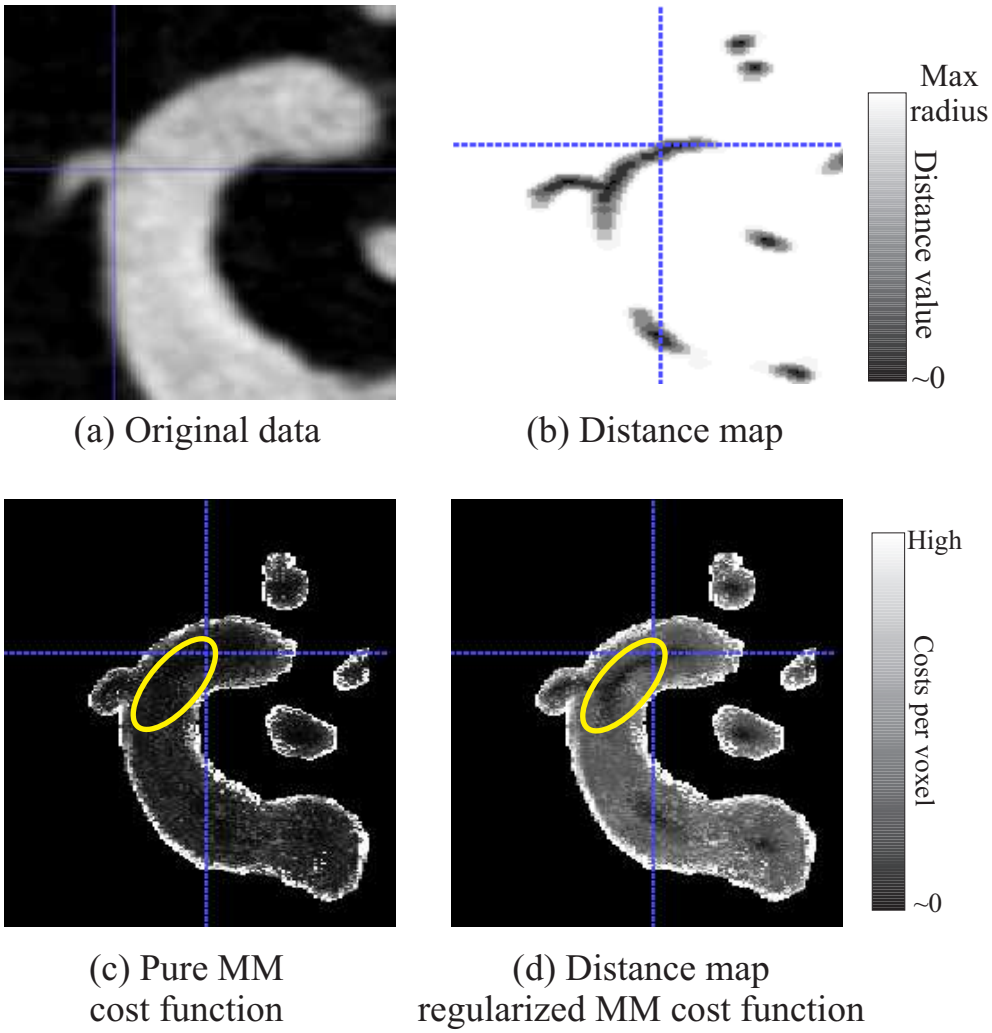

(a) Original data (b) Distance map

(c) Pure MM cost function (d) Distance map regularized MM cost function

Figure 4.3: (a) shows the internal carotid artery of a cerebral 3-DRA dataset and the corresponding skeleton-based distance map (b) limited up to the maximum vessel radius. (c) and (d) compares the pure MM based cost function with our proposed distance map regularized MM cost function.

because it would otherwise corrupt the cost function behavior for vessel branches which are not present within the statistical threshold result. Therefore, the distance function is limited to a maximum value, i.e. $\text{dist}(\boldsymbol{x}) = \min(\text{dist}(\boldsymbol{x}), \text{dist}_{\text{max}})$. dist_{max} denotes the maximum vessel radius observed within the thresholded volume (section 4.3.1).

4.3.4 Centerline Extraction using Minimum-cost Path

Each voxel is now associated with its dedicated costs $\Gamma(\boldsymbol{x})$ which is used to compute the vessel centerline via minimum-cost path approach. The entire vessel tree is extracted with one seed point $\boldsymbol{s}_0$ which is placed at the root location of the vessel tree. Dijkstra's algorithm processes the entire volume on the fly where only those voxel positions are considered whose MM response is above a certain

threshold value t_{MM} . When the MM value is below t_{MM}, the current voxel position is excluded from Dijkstra processing and added to the boundary set $\boldsymbol{y} = (\boldsymbol{y}_0, \boldsymbol{y}_1, ..., \boldsymbol{y}_{N-1}) \in \mathbb{R}^{5\times N}$. Each vector $\boldsymbol{y}_j = (\boldsymbol{x}, l_c, r_{\text{mean}}) \in \mathbb{R}^5$ consists of the position, its centerline length l_c and average radius r_{mean}. Each $\boldsymbol{y}_j$ represents one possible centerline path connected to the root seed point due to Dijkstra's shortest path algorithm computation. The centerline computation stops automatically once there is no voxel position delivering MM values above t_{MM}. The actual centerline extraction approach is depicted below in an algorithmic manner. t_{val} denotes a

Program 4.1: Centerline extraction

```
Input: y, t_val
Output: P_F set of final centerline paths.
begin
    P_F ⟵ ∅
    t_val ⟵ 2.0
    y sort all centerline paths according to its length w.r.t costs (longest first)
    while y ≠ ∅ do
        take boundary position y_0 and remove it from y
        p_tmp ⟵ trace back y_0 until root seed point s_0
        mark each node passed while performing back tracing
        if back tracing hits an existing path then
            recompute l_c and r_mean of y_0 for the corresponding path until hit
            y_tmp ⟵ update centerline path
        end
        if l_c / r_mean > t_val then
            P_F ⟵ P_F + y_tmp
        end
    end
end
```

validity centerline threshold, i. e. every centerline path should be t_{val} times longer than its mean radius. Figure 4.4 illustrates the mechanism of the algorithm. First, the algorithm starts with the back tracing process taking $\boldsymbol{y}_0$ and ends up with the centerline path 1. Second, it takes $\boldsymbol{y}_1$ from the boundary set $\boldsymbol{y}$ and traces back to $\boldsymbol{s}_0$ while it hits the existing path 1 at A. Now, the extraction stops and the length and average radius of the path from $\boldsymbol{y}_1$ to A is re-computed. If the ratio between length and average radius for the path $\boldsymbol{y}_1$ to A is above t_{val}, this path will be added to the set of final centerline paths. Otherwise it is removed. B-splines are used to approximate and smooth each centerline path.

Once all centerline paths are determined, the semantic centerline tree is constructed. Semantic means that the tree has one root centerline and the relationship between the centerline paths are considered to order the paths in a hierarchical father-son manner. Depending on whether cerebral or coronary arteries are acquired, the position of the patient on the table of the C-arm system is a priori known. Hence, for coronary reconstructions, the root centerline path is located in

Table 4.1: Evaluation results concerning 3-D DSA and coronary vessel centerlines. All quantitative measurements are given in mm. A and E denote automatic and expert.

3-D DSA - Quantitative comparison																
Data	$\mathcal{D}_1$	$\mathcal{D}_2$	$\mathcal{D}_3$	$\mathcal{D}_4$	$\mathcal{D}_5$	$\mathcal{D}_6$	$\mathcal{D}_7$	$\mathcal{D}_8$	$\mathcal{D}_9$	$\mathcal{D}_{10}$	$\mathcal{D}_{11}$	$\mathcal{D}_{12}$	$\mathcal{D}_{13}$	$\mathcal{D}_{14}$	$\mathcal{D}_{15}$	Mean
d_{mean} [mm]	0.13	0.14	0.14	0.10	0.13	0.19	0.13	0.14	0.13	0.13	0.21	0.18	0.10	0.12	0.13	**0.14**
d_{H} [mm]	0.68	0.69	1.61	1.00	0.73	1.90	1.23	1.92	1.60	1.74	2.21	2.19	1.13	1.49	1.53	**1.44**
3-D cardiac - Quantitative comparison																
Data	$\mathcal{D}_1$	$\mathcal{D}_2$	$\mathcal{D}_3$	$\mathcal{D}_4$	$\mathcal{D}_5$	$\mathcal{D}_6$	$\mathcal{D}_7$	$\mathcal{D}_8$	$\mathcal{D}_9$	$\mathcal{D}_{10}$	$\mathcal{D}_{11}$	$\mathcal{D}_{12}$	$\mathcal{D}_{13}$			
d_{mean} [mm]	0.23	0.42	0.43	0.37	0.40	0.49	0.40	0.52	0.34	0.65	0.35	0.38	0.44			**0.42**
d_{H} [mm]	4.37	6.63	3.55	1.66	5.16	4.69	4.80	5.49	1.59	2.98	3.04	11.29	2.98			**4.48**
Qualitative coronary vessel segment assessment																
#Seg. (A/E)	9/9 LCA	8/10 LCA	9/9 LCA	9/9 LCA	10/11 LCA	9/9 LCA	9/10 LCA	3/3 RCA	2/2 RCA	4/4 RCA	6/7 LCA	8/9 LCA	4/4 RCA			**95%**

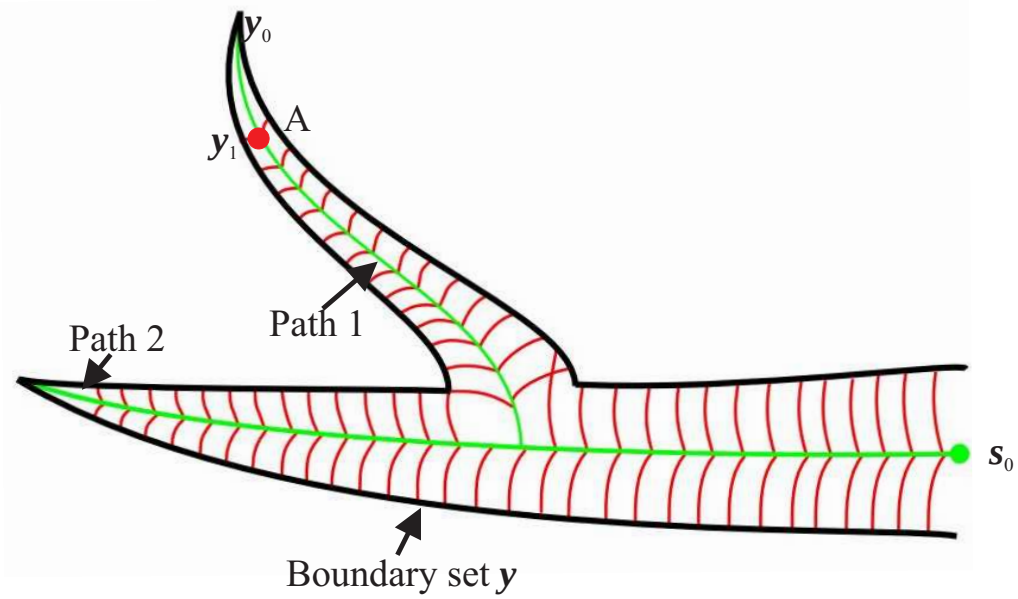

Figure 4.4: Illustration of the centerline extraction scheme. Paths 1 and 2 represent the longest paths with their vessel branches. All red paths are eliminated because the ratio between path length and mean radius is too small.

the upper part of the volume whereas for cerebral reconstructions, the root centerline denotes the largest vessel entering the volume from the bottom.

4.4 Evaluation and Results

4.4.1 Methods of Evaluation

Our proposed centerline method has been evaluated in a quantitative and qualitative manner with respect to different vessels, e. g. cerebral and coronary. The mean d_{mean} and the Hausdorff distance d_{H} have been applied to compare the pure MM driven centerline with our new distance map regularized MM centerline method. The qualitative assessment for the coronary vessels was performed by a medical expert. The coronary vessel tree detection result was assessed according to the coronary vessel tree model [Aust 75]. The model divides the coronary vessels into 15 segments, i.e. 4 RCA, 11 LCA (1 main LCA, 5 LAD and 5 LCx). A medical expert counted the number of coronary segments visible within the dataset and compared it with the centerline detection result based on our newly proposed cost function.

4.4.2 Experimental Results

In total, 15 3-D DSA and 13 motion-compensated coronary datasets were used to show the clinical flexibility and robustness of our centerline method. The image dimensions covering all datasets range between 192^3 and 512^3 voxels. The isotropic voxel spacing is 0.1 mm for 3-D DSA and 0.75 mm for cardiac volumes. The maxi-

mum radius r_{max} is set to 35 and 12 pixels for cerebral and coronary, respectively. The α is 0.1. The box size s is between 32^3 and 64^3 pixels for the coronary and cerebral data. The validity centerline threshold t_{val} is set to 0.2 and 0.12 for cerebral and coronary vessels, respectively. Table 4.1 gives an overview about the evaluation results. The mean distance shows that both centerlines are rather close to each other. The Hausdorff distance, however, reveals that there are centerline parts which heavily deviate between both approaches. The red circles in Figure 4.5 (top row) illustrate the major differences mostly appearing in medium and large vessel sections where the MM driven centerline suffers from inhomogeneous contrast agent distribution. Our regularized centerline approach models vessel bifurcations in a strict manner, i.e. the bifurcation is not cut short as depicted in Figure 4.5 (middle row). Moreover, Figure 4.5 (bottom row) depicts that our newly proposed centerline approach computes straight paths within small coronaries and better handles elliptical-shaped vessels with fewer path fluctuations. The qualitative coronary evaluation shows that our method robustly detects 95% of all segments observed by the medical expert.

4.5 Discussion

The results have shown that the newly introduced distance map regularized MM centerline approach delivers more accurate centerline paths concerning 3-DRA datasets especially for large or elliptical-shaped vessels. This allows coming up with more accurate vessel measurements like diameter or aneurysm neck size for stent placement or coiling embolization in interventional angio suites. The average distance indicates an almost identical match between both approaches. However, the Hausdorff distance reveals that there are centerline paths which heavily deviate. This deviation can be most often observed within major vessel branches. Especially for small coronary vessel branches, our approach delivers straight paths with fewer fluctuations.

No ground truth centerlines have been used to evaluate the accuracy of the centerline paths because the creation of such ground truth centerlines is rather difficult. Vessel motion, heterogeneous contrast agent distribution, beam hardening as well as reconstruction kernels leading to vessel boundary edge ramps make the manual outlining of centerlines a difficult task. This has to be evaluated within a different study investigating the inter observer variability.

The entire algorithm is integrated within a clinical approach allowing to manually remove centerlines which are actually false alarms to prepare subsequent post-processing steps like 2-D and 3-D vessel segmentation. As described in Chapter 3, the 3-D vessel centerline tree can be utilized to initialize the semi-automatic 2-D vessel segmentation approach by performing a forward projection onto corresponding 2-D angiography images. This forward projection opens up the possibility to acquire vessel measurements like diameter in 2-D because the quantification of vessels within 3-DRA datasets is affected with uncertainty due to motion or improper contrast agent distribution. Furthermore, the next Chapter 5 requires a pre-computed vessel centerline such that interleaved 3-D ellipsoids can be placed

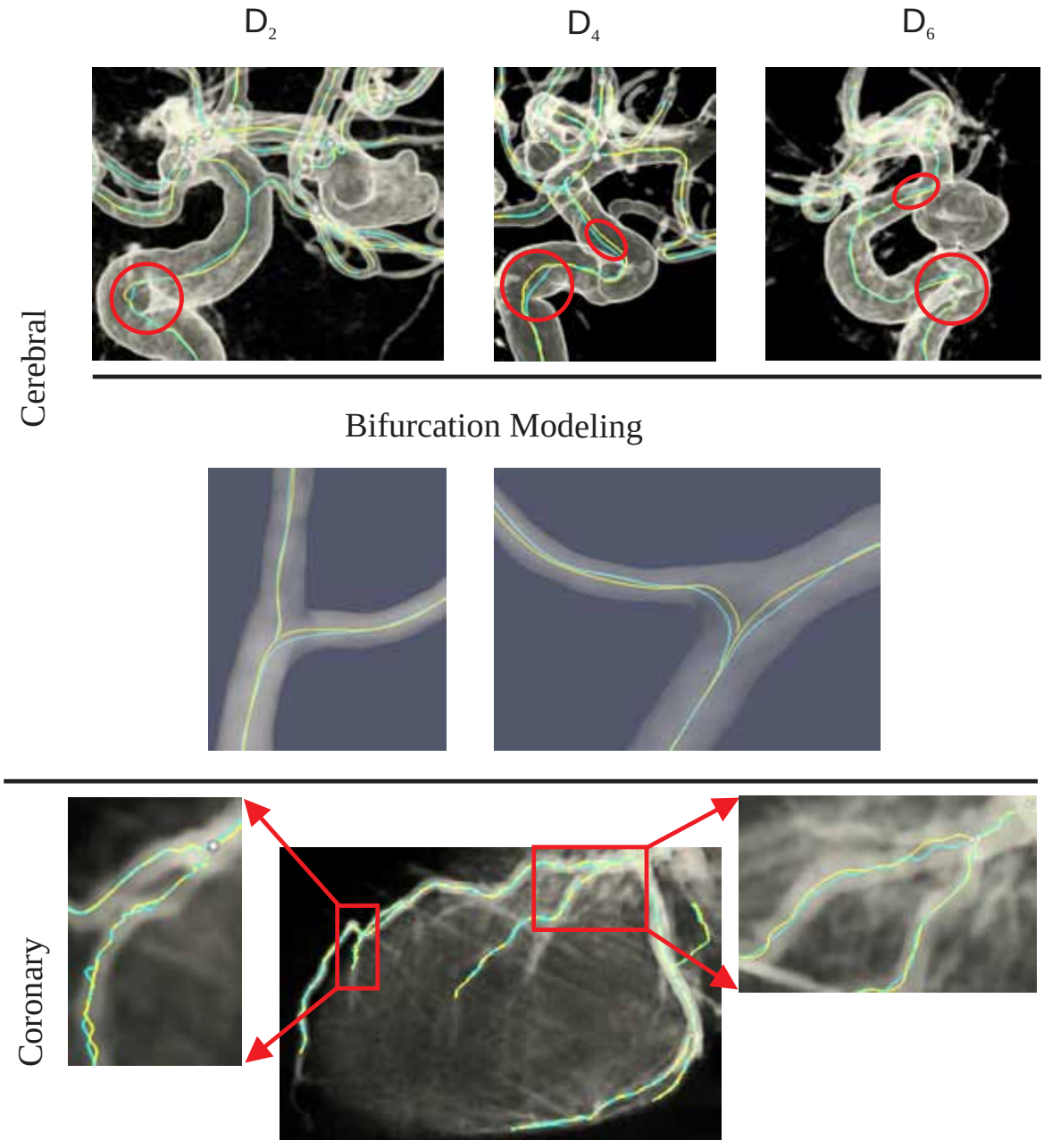

Figure 4.5: Centerline results for cerebral and coronary vessels. Yellow centerlines denote the distance map regularized paths and turquoise colored centerlines represent the purely MM driven paths. Red labels depict the major deviations between both approaches.

along the centerlines to approximate and segment the vessel branches in a smooth manner.

4.6 Conclusion

This chapter has presented a centerline extraction methodology which is mainly based on a multi-scale MM filtering and a graph-related minimum-cost path approach. The main contribution of our work denotes an extension of the voxel-based cost function which especially regularizes centerline paths within vessel regions showing inhomogenous contrast agent or elliptical-shaped vessels. The regularizer comprises a novel local adaptive statistical thresholding which makes use of the a priori known intensity distribution of 3-DRA datasets, a subsequent skeletonization and distance map computation. An evaluation performed on two types of vessels, cerebral and coronary, demonstrates the robustness of our approach and delivers better results as the pure MM driven centerline technique.

The next chapter uses the centerline tree as initialization for the ellipsoid-based 3-D vessel segmentation.

CHAPTER 5

2-D Driven 3-D Vessel Segmentation

A 2-D driven 3-D vessel segmentation algorithm is presented within this chapter which takes the results from Chapter 3 and 4 into account. The 3-D vessel segmentation approach is an interleaved ellipsoid-based method which allows to locally adapting to 3-D vessel branches. Chapter 4 provides the required vessel centerline tree which is utilized as initialization to arrange the ellipsoids along the centerlines. The results of Chapter 3 deliver corresponding 2-D vessel segmentations such that the 3-D segmentation can be adjusted towards the edge information from the 2-D images. The adaptation of the 3-D segmentation towards the 2-D information is performed by a novel method making use of the 2-D/3-D registration principle. The combination of 2-D and 3-D vessel information opens up the opportunity to perform a validation of different 3-D vessel segmentation methodologies based on 3-D DSA volumes. Our segmentation framework is evaluated using one phantom and ten patient datasets. The 2-D adapted 3-D segmentation results show an average increase in precision of 6% against methods driven purely on 3-D information. The algorithm has been conditionally accepted in [Spie 11b] and patented [Spie 11a].

5.1 Motivation

As already mentioned within the introduction part of this thesis, 3-D DSA is a well established and helpful technique in modern neuroradiology to visualize complex cerebral vascular pathology and to guide interventional procedures. More and more 3-D DSA data are also used for further quantitative analysis to support treatment planning and therapeutic procedures in patients with cerebrovascular dis-

eases, e.g. aneurysms or stenosis [Hera 06a]. This analysis requires reliable 3-D vessel segmentation methods that delineate the boundary of the vessel as accurate as possible to come up with exact vessel measurements, e.g. vessel diameter, bifurcation angle of vessel branches, aneurysm dome sizes etc. Since latest investigational techniques like hemodynamic simulations based on CFD have become more and more popular within the research community of neuroradiology [Cebr 05a, Cast 06, Ford 08, Jou 08, Spie 11c], the segmentation result and its corresponding mesh representation are the base for even more reliable analysis. Small changes within the segmentation result may induce completely different flow patterns or wall shear stress distributions ([Venu 06] and see Chapter 7). Hence, vessel segmentation results get more important for post-processing applications within the clinical environment. Accurate vessel segmentation based on 3-D DSA is challenging as it depends on the quality of the 3-D DSA image that might vary for the individual patient. In clinical practice, there are a lot of factors that contribute to optimal and reproducible image quality. This includes the amount of injected contrast agent, the timing of injection, hemodynamic mixture of contrast agent and factors like blood flow cardiac output. Also reconstruction parameters may be different between patients [Zell 05, Stro 09]. Figure 5.1 gives examples about the influence of the different acquisition parameters on the final 3-D DSA reconstructed images. The edge ramp between background and vessel intensities differs dependent on the applied reconstruction kernel (see Figure 5.1 upper part), e.g. some kernels yield an edge ramp whose slope is much higher than those generated by another kernel [Kak 88, Buzu 08]. These profiles open a space for different segmentation methods to differently interpret these edge ramps which may lead to varying vessel boundary positions. The ramp itself is also an indicator how the contrast agent is distributed at this position. In case of sub-optimal injection timing, the contrast agent may leach out which leads to locally blurred vessel boundaries. Even if all acquisition parameters would be exactly the same, the final 3-D DSA image volume will slightly differ because of the heterogeneous hemodynamic mixture of the contrast agent with the blood. Due to this, the validation of 3-D DSA vessel segmentation results turns out to be rather difficult and thus 2-D DSA imaging is still considered as gold standard in quantitative evaluation and measurements [Peke 09] being available during and after interventional evaluations. This is a challenge to validate any kind of segmentation methods so far that is especially true for the individual patient while phantom models can be used for general validation tests.

To overcome these challenges, a novel 3-D vessel segmentation method is proposed in this thesis that is driven by 2-D vessel information. 2-D DSA acquisitions are used as validation base for 3-D segmentations as well as a driving force to adapt an initial 3-D segmentation. Each 3-D DSA dataset comes automatically with 133 2-D DSA projections showing the patient from various viewing angles. Moreover, these projections are registered and calibrated with the 3-D DSA dataset. Selected 2-D DSA images exhibit the advantage that the vessel boundaries are clearly visible and not blurred as it often happens in 3-D DSA images. The 3-D vessel segmentation approach denotes a 3-D parametric vessel segmentation technique based on ellipsoids. The novelty of our approach now comprises an

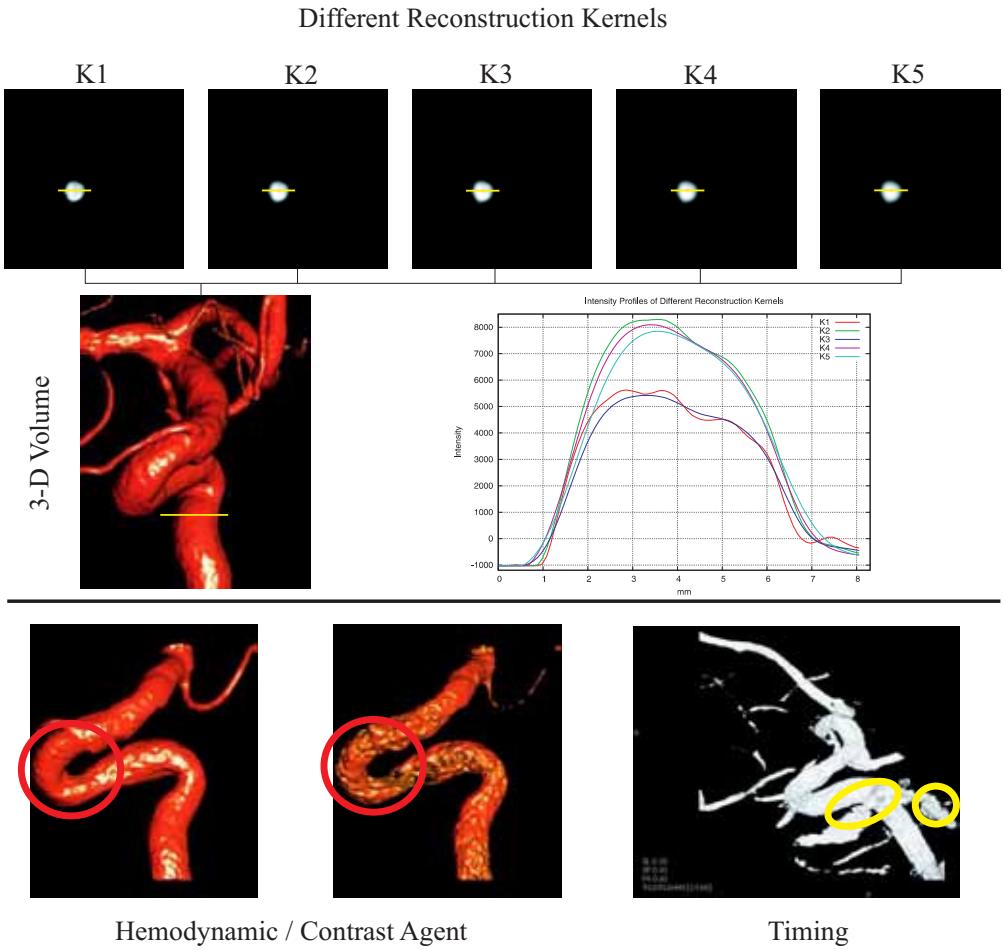

Figure 5.1: Influence parameters during the generation of a 3-D DSA image: The upper part of the image shows the result using five different reconstruction kernels according with the intensity profiles. The lower part illustrates how beam hardening and the distribution of contrast agent affect the reconstruction result (see red circles). Also an improper timing of contrast agent injection is depicted on the lower right corner where the venous phase is already visible (see yellow circles).

automatic segmentation algorithm that smoothly combines 2-D vessel information with a given 3-D vessel segmentation. Given a certain number of 2-D DSA acquisitions, a forward projection of the current 3-D segmentation is computed to be overlaid with the 2-D acquisitions. The match between forward projection and 2-D DSA vessel information is used to drive and adapt the 3-D vessel segmentation towards the 2-D information. Figure 5.2 illustrates the entire algorithm.

5.2 Related Work

Within the last ten years, a large variety of vessel detection, extraction and segmentation algorithms have been introduced for all kinds of imaging modalities (CT, MRI, 3-D DSA) and applications. An extensive overview of this field is given

by Lesage *et al.* [Lesa 09] as well as by Kirbas and Quek [Kirb 04]. The focus in this section lies on vessel segmentation approaches using 3-D DSA image data.

The 3-D vessel segmentation approach used in this work is related to tubular-preserving vessel models. Yim *et al.* [Yim 01] employs a tubular deformable model in order to reconstruct vessel surfaces from 3-D angiographic images. Another idea, proposed by Tyrrell *et al.* [Tyrr 07], models complex vessel trees by cylindrical super ellipsoids together with a joint estimation of vessel boundary and centerlines. This approach does not take explicit edge information into account for vessel boundary detection. Wong and Chung [Wong 07] introduced a probabilistic vessel axis tracing method for 3-D angiograms to delineate the vessel boundary on cross sections. In a second step, the 3-D vessel surface is defined by the minimum cost path on a weighted acyclic graph. Chang *et al.* [Chan 09] applied a region-growing segmentation approach on 3-D DSA image data with a 3-D extension for deformable contour based on charged fluid model. 4-D minimal paths are used by Li *et al.* [Li 07] to exploit and reconstruct 3-D tubular structures on MR angiography and CT images. A non-parametric deformable model with high-order multiscale features is proposed by Hernandez *et al.* [Hern 07] to segment vascular structures in 3-D DSA and CT data. Gan *et al.* [Gan 05] applied a statistical vessel segmentation approach for 3-D DSA images using expectation-maximization (EM) algorithm to estimate the intensity distribution of vessels based on maximum intensity projection (MIP) images. Kang *et al.* [Kang 09] introduces a complementary geodesic distance field in order to smoothly register a given centerline onto the vessel lumen and to adapt an active tube model.

Another common approach is to apply multiscale filtering methods for determining vessel boundaries and to subsequently extract the vessel geometry from the image volume. Law and Chung [Law 07] introduced a combination of translated and rotate first derivative Gaussian filters to detect the intensity drop along vessels and aneurysms. The detection response is used to guide a level set segmentation framework. Tek *et al.* [Tek 05] described an algorithm for multiscale vessel detection and segmentation by using mean-shift analysis.
The literature shows some works which combine 2-D DSA images with different 3-D imaging modalities, e.g. 3-D DSA, CT or MR [Hipw 03, Chan 04]. Groher *et al.* [Groh 07] proposed a 2D-3D registration approach of abdominal angiographic data to register a catheter. Hentschke and Toennies [Hent 09, Hent 10] registered 2-D DSA images with 3-D DRA datasets to compare and validate flow simulation with the flow information encoded in 2-D DSA images.

Although there are already ambitions to incorporate 2-D information into 3-D image datasets for various purposes, so far there is no 2-D driven 3-D vessel segmentation framework which adapts 3-D vessel morphology by using 2-D DSA information.

5.3 Methods

This section describes the proposed 2-D driven 3-D vessel segmentation approach. First, a short overview is given about the applied ellipsoid-based 3-D vessel segmentation which is enhanced by a local foreground/background intensity estima-

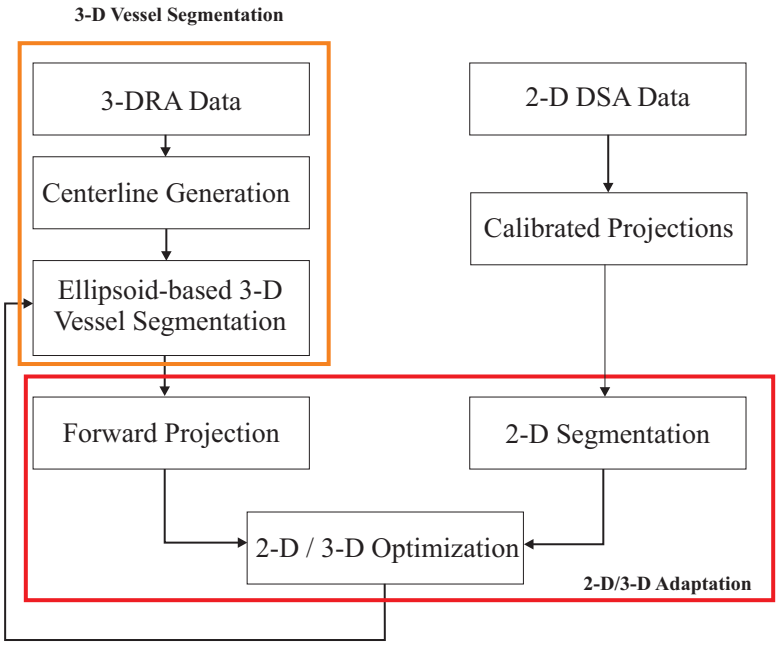

Figure 5.2: Overview about the proposed 2-D driven 3-D vessel segmentation system. The orange box indicates the 3-D vessel segmentation approach and the red box illustrates the components of the 2-D/3-D adaptation method.

tion using GMMs (Chapter 4). Our ellipsoid-based vessel segmentation is similar to the approach from [Tyrr 07]. The methodology combining 2-D and 3-D vessel information represents the core part of this work and will be discussed in detail. Figure 5.2 depicts the individual modules of the algorithms as a flow chart.

5.3.1 3-D Vessel Segmentation Approach

The main purpose of the 3-D segmentation approach is to detect and segment medium and large vessels within 3-D DSA datasets delivering the input for the subsequent adaptation with 2-D information.

Initialization and Centerline

The centerline technique described in Chapter 4 requires at least one seed point for initialization and to start the centerline computation. Within Chapter 4, this seed point was manually provided by the user. Since the position of the patient on the table of the C-arm system remains always the same, the major vessel like ICA enters the reconstructed image volume from the bottom. Hence, the flow direction of the contrast agent is from bottom to top. This prior knowledge is now used to automatically provide this seed point by finding the position of the largest vessel entering the volume. Therefore, the Hough-Transformation [Jaeh 11] for circles is applied on the most bottom slice of a 3-D DSA image to localize entering vessels of a certain diameter. The position associated with the largest diameter is taken as seed point for the centerline computation method. Figure 4.5 (upper part) gives an example of the vessel centerline tree.

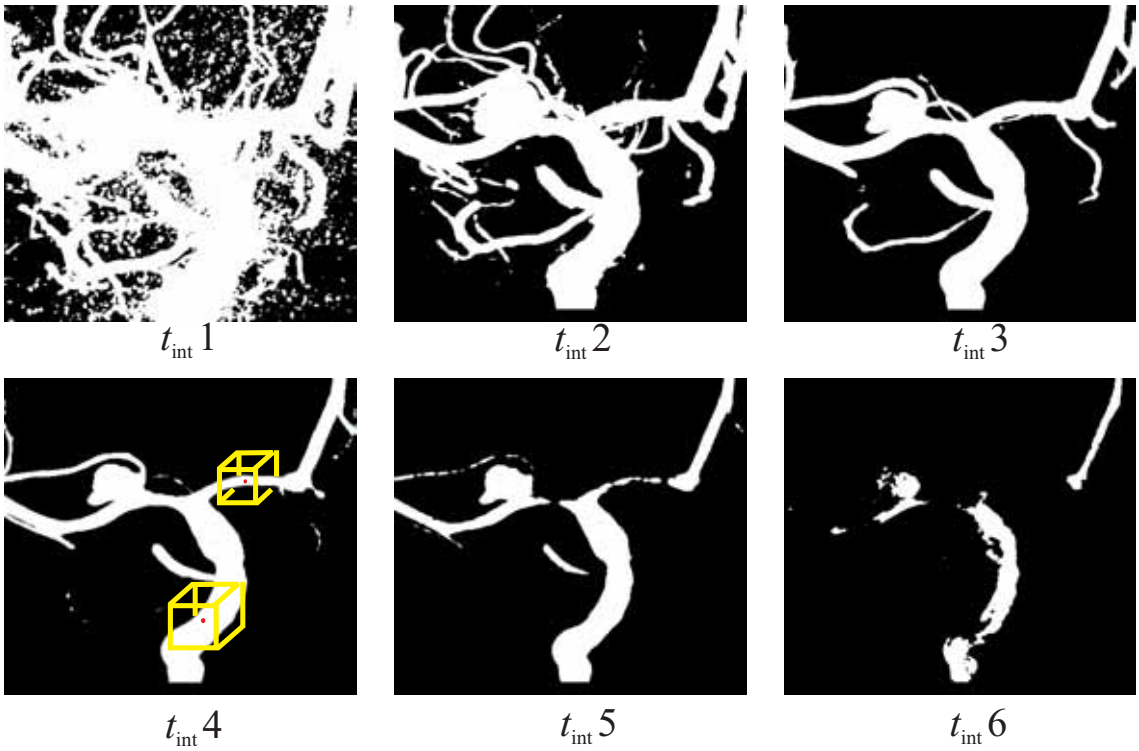

Figure 5.3: Different intensity windowing thresholds are applied to patient dataset 9. t_{int} denotes intensity threshold value which is increasing from t_{int} 1 to t_{int} 6, i.e. t_{int} 1 represents a very low threshold and t_{int} 6 depicts the windowing result using a very high intensity threshold. The yellow boxes are used to estimate local intensity thresholds which are described in detail within Chapter 4.3.1.

Ellipsoid-based Vessel Segmentation

Superellipsoids, ellipsoids or spheres are geometric primitives that are well suited for describing local vessel segments because such primitives being interleaved are able to approximate the tubular vessel structures in a smooth manner as mentioned in [Tyrr 07]. A unit sphere located within the coordinate center is implicitly defined as follows:

$$F(\boldsymbol{x}) = x_0^2 + x_1^2 + x_2^2 = 1 \tag{5.1}$$

where $\boldsymbol{x} = (x_0, x_1, x_2)^T \in \mathbb{R}^3$ denotes a point on the surface of the sphere. To approximate localized vessel segments, a coordinate transformation has to be applied to allow arbitrary rotation, scale and translation, i.e. nine transformation parameters have to be estimated (three rotation, three scaling, three translation). The entire transformation function is expressed by

$$T(\phi, \boldsymbol{x}) = \boldsymbol{R}(\boldsymbol{r})\boldsymbol{S}(\boldsymbol{s})\boldsymbol{x} + \boldsymbol{t}. \tag{5.2}$$

$\mathbf{R}$ represents the 3×3 rotation matrix with the argument $\boldsymbol{r} \in \mathbb{R}^3$ as rotation parameters. The scaling parameters $\boldsymbol{s} \in \mathbb{R}^3$ are encoded within the 3×3 diagonal matrix $\boldsymbol{S}(\boldsymbol{s})$ and $\boldsymbol{t} \in \mathbb{R}^3$ denotes the translation vector. All transformation parameters are

summarized within the vector $\phi = (\boldsymbol{r}, \boldsymbol{s}, \boldsymbol{t}) \in \mathbb{R}^9$. Thus, the implicit shape model can be rewritten as

$$F_T(\phi, \boldsymbol{x}) := F(T(\phi, \boldsymbol{x})) = F(\boldsymbol{R}(\boldsymbol{r})\boldsymbol{S}(\boldsymbol{s})\boldsymbol{x} + \boldsymbol{t}) \tag{5.3}$$

which separates the space into three different regions:

$$F_T(\phi, \boldsymbol{x}) \in \begin{cases} < & 1, \text{if } \boldsymbol{x} \in \mathcal{I}(\phi) \\ & 1, \text{if } \boldsymbol{x} \in \mathcal{S}(\phi) \\ > & 1, \text{if } \boldsymbol{x} \in \mathcal{O} \backslash (\mathcal{I}(\phi) \cup \mathcal{S}(\phi)), \end{cases} \tag{5.4}$$

where $\mathcal{S}(\phi)$ and $\mathcal{I}(\phi)$ denote the surface and the interior of an ellipsoid respectively. $\mathcal{O}$ describes the image domain. This distinction will be later used as external energy term within the global objective function to estimate the parameters properly. The previously computed centerlines (see Chapter 4) are used to initialize the parameters, i.e. the center of the ellipsoids is placed on the centerlines. They are rotated such that the tangent vector of the centerline coincides with the local z-axis of the ellipsoid. The curvature of the centerline is utilized to determine the number of ellipsoids that are required to approximate the vessel branch. In centerline sections with high curvature, the number of ellipsoids is increased while the ellipsoid scale in z-direction is concurrently decreased. Areas of low curvature are treated vice versa. The ellipsoid scales pointing perpendicular to the vessel direction are initialized by cross-sectional radius intensity profiling. The parameter vector $\Phi = (\phi_0, \phi_1, ..., \phi_{M-1}) \in \mathbb{R}^{9\times M}$ holds all ellipsoid parameter of the entire model and M denotes the total number of ellipsoids used. For each ellipsoid, a specific local intensity threshold is estimated using GMM dividing the local image domain into foreground and background intensities. This is done to properly cover the heterogeneous intensity distribution within and around vessels as illustrated in Figure 5.3 (yellow boxes). The boxes are used as environment to estimate the local intensity threshold for each ellipsoid. The threshold values are stored within the vector $\boldsymbol{h} = (h_0, h_1, ..., h_{M-1})^T \in \mathbb{R}^M$. This estimate is further described later within this text when it comes to the definition of the *external energy* functional.

The initialized ellipsoid tube model is now optimized such that the model evolves towards the boundary of the vessels according to a predefined energy. The total energy functional, $G_{\text{tot}}(\Phi, \boldsymbol{h})$, is composed of two terms:

$$\begin{aligned} G_{\text{tot}}(\Phi, \boldsymbol{h}) &: \mathbb{R}^{9\times M} \times \mathbb{R}^M \to \mathbb{R} \\ \arg\min_{\Phi, \boldsymbol{h}} G_{\text{tot}}(\Phi, \boldsymbol{h}) &= \alpha G_{\text{ext}}(\Phi, \boldsymbol{h}) + (1-\alpha) G_{\text{int}}(\Phi) \end{aligned} \tag{5.5}$$

where $G_{\text{ext}}(\Phi, \boldsymbol{h})$ and $G_{\text{int}}(\Phi)$ denote the external and internal energy term respectively. α defines the weighting factor.

The *internal energy* term is associated to the inherent characteristics of the tube model, i.e. the pose parameters between two subsequent ellipsoids have to be modeled in a smooth way. For that purpose, the internal energy term consists of

three cubic B-splines ($\{B_i\}_{i=0}^{2}$) to ensure smoothness in terms of rotation, scaling and translation between neighboring ellipsoids:

$$G_{\text{int}}(\Phi) = \sum_{i=0}^{2} \int_{R_i} \left| B_i(k,\Phi)' \right| dk + \int_{R_i} \left| B_i(k,\Phi)'' \right| dk \tag{5.6}$$

where $B_i(k,\Phi)'$ and $B_i(k,\Phi)''$ represent the first and second derivative of the B-spline B_i. R_i is the total length of the B-spline and k the position on the spline. The first B-spline, $B_0(k,\Phi)$, is a B-spline in 2-D and it describes the change of orientation between two ellipsoids. Its sample points $\boldsymbol{q}_r = (k,\delta) \in \mathbb{R}^2$ are defined by k and δ denoting the length position of the ellipsoid center on the B-spline and the change of the orientation angle between two ellipsoids respectively. $B_1(k,\Phi)$ is a B-spline in 3-D covering the change of scales between subsequent ellipsoids. The sample points are defined as $\boldsymbol{q}_s = (k, s_0, s_1) \in \mathbb{R}^3$ where s_0 and s_1 represent the scaling in x-y direction of the ellipsoid. The last B-spline, $B_2(k,\Phi)$, represents the centerline in 3-D which is now defined by the center points of the ellipsoids $\boldsymbol{q}_t = (c_0, c_1, c_2) \in \mathbb{R}^3$.

The *external energy* term is responsible to drive the model towards the surrounding vessel structures. A 3-D DSA image consists of foreground and background voxel intensities as already described in Chapter 4.3.1. Given this prior knowledge, our ellipsoid vessel shape model tries to separate the image domain into these two regions as good as possible. This is evaluated by counting the number of foreground and background voxel intensities within the sets $\mathcal{S}(\Phi_i)$ and $\mathcal{I}(\Phi_i)$. Depending on the local intensity threshold h_i and the ellipsoid parameters Φ_i, $\mathcal{F}(\Phi_i, h_i) \subset (\mathcal{S}(\Phi_i) \cup \mathcal{I}(\Phi_i))$ defines the set of foreground voxels. Consequently, $\mathcal{B}(\Phi_i, h_i) \subset (\mathcal{O} \backslash \mathcal{F}(\Phi_i, h_i))$ describes the set of background voxels which is constrained by the ellipsoid bounding box. The *external energy* is described as

$$G_{\text{ext}}(\Phi, \boldsymbol{h}) = \frac{1}{M} \sum_{i=0}^{M-1} \left(\frac{|\mathcal{F}(\Phi_i, h_i)| - |\mathcal{B}(\Phi_i, h_i)|}{|\mathcal{F}(\Phi_i, h_i) \cup \mathcal{B}(\Phi_i, h_i)|} \right)^{-1} \tag{5.7}$$

In Chapter 4.3.1, a global threshold was computed for image data preprocessing. Here however, the GMM modeling is used to estimate the local intensity threshold within a box which is centered at the current ellipsoid center and its size s ranges between 32^3 and 64^3 depending on the vessel scales. This local foreground/background estimation ensures that the external energy adapts to vessel structures exhibiting even high intensity variation throughout the entire dataset. The *external energy* term becomes minimal if the parameters Φ are estimated such that the number of foreground voxels $|\mathcal{F}(\Phi_i, h_i)|$ is maximum given a certain threshold h_i.

The optimal ellipsoid parameters are found by minimizing the total energy functional $G_{\text{tot}}(\Phi, \boldsymbol{h})$ together with the local intensity thresholds. Since the model is initialized by a pre-computed centerline and cross-sectional radius profile estimation, the initial parameter set is located near the global optimum. Hence, gradient descent is applied to optimize our energy functional using finite differences. There are other optimization schemes, however, which will lead to similar results.

5.3.2 2-D driven 3-D Adaptation

The methods described in section 5.3.1 deliver a parametric 3-D vessel segmentation result that is purely driven by 3-D image data. As already mentioned within the introduction part, the appearance of the 3-D DSA volume data depends on four factors of influence, i.e. amount of contrast agent, time of injection, hemodynamic mixture of the contrast agent and the applied reconstruction kernel. Therefore, a comparison of the 3-D segmentation result with 2-D DSA segmentation is necessary. 2-D DSA projections are manually selected to validate the 3-D segmentation result via overlay matching. The mapping of the volumetric data onto the 2-D DSA images is known by calibration [Hopp 07]. This comparison is performed by forward projection of the 3-D vessel segmentation using ray casting [Sher 90]. The basic idea of our novel 2-D driven 3-D segmentation method comes from 2-D / 3-D registration methods [Penn 98] where interventional 2-D DSA images are registered with previously acquired volumetric data to the intervention. Thus, the 2-D/3-D registration principle here is used as external force to drive the initial 3-D parametric segmentation result to perfectly match with the 2-D DSA projections. The novel external 2-D/3-D energy functional $G_{\text{ext2D/3D}}(\Phi)$ is now defined as follows:

$$G_{\text{ext2D/3D}}(\Phi) = \sum_{i=0}^{Q-1} \sum_{\boldsymbol{u}} \left(v(i,\boldsymbol{u}) - v(i,\boldsymbol{u},\Phi)\right)^2 \tag{5.8}$$

where Q indicates the number of projection images used to adapt the 3-D segmentation result and $v(i,\boldsymbol{u})$ denotes the intensity value of the 2-D ground truth segmentation of the i-th projection image at position $\boldsymbol{u}$. The intensity value of the forward projection $v(i,\boldsymbol{u},\Phi)$ is either one or zero because the 3-D segmentation is a binary volume such that the ray casting based forward projection generates a binary projection image. The novel 2-D/3-D external energy functional leads to a new total energy that is defined as follows:

$$\begin{aligned} G_{\text{tot2D/3D}}(\Phi) &: \mathbb{R}^{9\times M} \rightarrow \mathbb{R} \\ \arg\min_{\Phi} G_{\text{tot2D/3D}}(\Phi) &= \alpha G_{\text{ext2D/3D}}(\Phi) + (1-\alpha) G_{\text{int}}(\Phi) \end{aligned} \tag{5.9}$$

The external energy term in Eq. 5.5 is replaced by the new 2-D driven 3-D external force $G_{\text{ext2D/3D}}(\Phi)$ while the internal energy is kept. The internal energy functional denotes an important regularization term during 2-D/3-D adaptation because the 3-D information is lost while performing the forward projection. Thus, the internal energy ensures that the 3-D ellipsoid model does not deform towards unrealistic vessel approximations or twisting.

As illustrated in Eq. 5.8, the *sum of squared differences* (SSD) between the 2-D ground truth and the forward projection is applied as similarity measure. Considering the 2-D/3-D medical image registration literature, however, there might be other similarity measures [Penn 98] like *normalized cross correlation* etc. which might lead to similar results.

Program 5.1: 2-D driven 3-D ellipsoid vessel segmentation

Input: Φ // ellipsoid parameter vector initialized using centerline and radius profiling
$\boldsymbol{h}$ // local intensity thresholds
t_κ // 2-D/3-D similarity measure threshold
N // number of 2-D projections used
Output: Φ // parametric 3-D vessel segmentation optimized according 2-D information
begin
  // Pure 3-D driven ellipsoid-based vessel segmentation **for** $i \leftarrow 0$ **to** $M-1$ **do**
    $h_i \leftarrow$ threshold estimation using GMM's
    $\Phi_i \leftarrow$ optimize Φ_i such that local ellipsoid energy $G_{\text{tot}}(\Phi_i, h_i) \rightarrow \min$
  end
  // 2-D driven 3-D ellipsoid-based vessel segmentation **for** $i \leftarrow 0$ **to** $M-1$ **do**
    // Initialize cost function
    $\kappa_{\text{old}} \leftarrow 0$
    for $j \leftarrow 0$ **to** $N-1$ **do**
      Perform forward projection according jth projection matrix
      $\kappa_{\text{tmp}} \leftarrow$ compute κ, e.g. SSD between 2-D segmentation and forward projection
      $\kappa_{\text{old}} \leftarrow \kappa_{\text{old}} +$ tmp
    end
    loop $\leftarrow$ true
    while *loop* **do**
      optimize Φ_i such that global energy $G_{\text{tot2D/3D}} \rightarrow \min$
      $\kappa_{\text{new}} \leftarrow 0$
      for $j \leftarrow 0$ **to** $N-1$ **do**
        Perform forward projection according jth projection matrix
        $\kappa_{\text{tmp}} \leftarrow$ compute κ, e.g. SSD between 2-D segmentation and forward projection
        $\kappa_{\text{new}} \leftarrow \kappa_{\text{new}} + \kappa_{\text{tmp}}$
      end
      if $|\kappa_{new} - \kappa_{old}| < t_\kappa$ **then**
        loop $\leftarrow$ false
        $\kappa_{\text{old}} \leftarrow \kappa_{\text{new}}$
      end
    end
  end
end

5.4 Evaluation and Results

The 2-D driven 3-D vessel segmentation method was evaluated on one phantom image and ten patient datasets with different cerebrovascular disease. The datasets were again acquired at the Department of Neuroradiology (University Hospital Erlangen, Germany), during endovascular interventions using a flat-panel equipped C-Arm System (AXIOM Artis dBA, Siemens AG Healthcare Sector, Forchheim, Germany). The volume dimensions range between $512 \times 512 \times 390$ and $512 \times 512 \times 511$ with an isotropic voxel spacing of 0.1mm. A 3-D DSA image volume is commonly reconstructed given 133 2-D DSA projections that were acquired while the C-Arm rotates around the patient's head. Three out of the 133 projections were selected showing the volume from different viewing angles to perform the 2-D/3-D match. The viewing angle difference of the selected projections varies from 10 to 170 degree which ensures an adaptation of the 3-D segmentation according to sufficiently different 2-D projections. The novel idea of using 2-D DSA projection in order to refine the given 3-D ellipsoid-based segmentation result is compared to the clinical established threshold-based region growing segmentation. Hence, three different 3-D vessel segmentations were computed, i.e. region-growing, 3-D ellipsoid and 2-D driven 3-D ellipsoid segmentation. The marching cubes algorithm [Lore 87] was applied to visualize the 3-D segmentation results as meshes.

5.4.1 Methods of Evaluation

Since the setup of 3-D gold standard segmentations given 3-D DSA data is rather difficult due to the dependency of many parameters (hemodynamic mixture of the contrast agent, applied reconstruction kernel, start and time of acquisition), the focus is on pure 2-D related evaluation measures. The 3-D segmentation result is being forward projected into 2-D defining the vessels of interest within the used 2-D DSA projections for adaptation (see Figure 5.4 left column (DSA) with the red boxes). These vessels were manually outlined and approved by a neuroradiologist to be used as gold standard segmentation in 2-D. The overlap between the forward projection of a 3-D segmentation result and the 2-D gold standard was evaluated using two measurements: Dice coefficient and precision. The Dice coefficient is defined by

$$d_{\mathrm{DICE}} = \frac{2\left|\boldsymbol{P}_{\mathrm{Gold}} \cap \boldsymbol{P}_{\mathrm{Seg}}\right|}{\left|\boldsymbol{P}_{\mathrm{Gold}}\right| + \left|\boldsymbol{P}_{\mathrm{Seg}}\right|} \tag{5.10}$$

The precision (P) is expressed by the following formula:

$$d_{\mathrm{PR}} = \frac{\#\mathrm{TP}}{\#\mathrm{TP} + \#\mathrm{FP}} \tag{5.11}$$

Table 5.1: Summary of the 2-D/2-D evaluation results. The numbers are mean values measuring the overlap (Dice, precision) between the forward projection of a 3-D segmentation method and the corresponding ground truth vessel segmentation of the selected 2-D DSA projection images. Here, the result against the incorporated 2-D DSA projections is shown.

	Method	Mean 2-D/2-D measurements - part of the optimization set.												
Dataset		$\mathcal{P}$	$\mathcal{D}_1$	$\mathcal{D}_2$	$\mathcal{D}_3$	$\mathcal{D}_4$	$\mathcal{D}_5$	$\mathcal{D}_6$	$\mathcal{D}_7$	$\mathcal{D}_8$	$\mathcal{D}_9$	$\mathcal{D}_{10}$	Mean	σ
	Region Growing	86.1	91.4	91.4	89.7	90.1	90.4	88.6	85.8	88.6	85.8	89.2	**89.1**	2.0
d_{DICE}	3-D Ellipsoid	91.4	89.8	92.9	90.4	89.7	91.8	87.0	86.0	89.8	88.5	88.4	**89.4**	2.1
	2-D driven 3-D	98.1	96.7	96.1	95.0	96.2	95.6	93.4	93.2	96.9	93.9	95.0	**95.2**	1.3
	Region Growing	76.3	87.1	86.2	84.9	86.1	84.7	82.4	77.9	83.3	78.0	81.4	**83.2**	3.3
d_{PR}	3-D Ellipsoid	85.8	91.9	91.1	85.0	85.1	90.5	84.2	83.9	88.4	85.4	84.6	**87.0**	3.1
	2-D driven 3-D	97.2	96.0	95.9	94.7	95.8	95.8	90.4	90.0	96.1	93.4	94.3	**94.2**	2.3

Table 5.2: Summary of the 2-D/2-D evaluation results. The numbers are mean values measuring the overlap (Dice, precision) between the forward projection of a 3-D segmentation method and the corresponding ground truth vessel segmentation of the selected 2-D DSA projection images. Here, three other 2-D DSA projections were selected that are ***not*** part of the optimization set in order to measure the overall match of our 2-D driven 3-D method.

	Method	Mean 2-D/2-D measurements - **not** part of the optimization set.												
Dataset		$\mathcal{P}$	$\mathcal{D}_1$	$\mathcal{D}_2$	$\mathcal{D}_3$	$\mathcal{D}_4$	$\mathcal{D}_5$	$\mathcal{D}_6$	$\mathcal{D}_7$	$\mathcal{D}_8$	$\mathcal{D}_9$	$\mathcal{D}_{10}$	Mean	σ
	Region Growing	86.7	92.0	91.0	90.2	92.7	91.9	91.1	85.4	91.2	85.9	88.5	**90.0**	2.6
d_{DICE}	3-D Ellipsoid	90.8	91.3	92.0	89.1	92.6	93.4	91.2	85.5	93.6	88.8	91.8	**90.9**	2.5
	2-D driven 3-D	95.0	93.4	92.0	91.0	92.8	92.4	91.9	89.6	89.8	92.6	90.2	**91.6**	1.3
	Region Growing	77.5	88.5	84.0	84.6	87.9	86.2	84.4	77.6	84.1	76.9	80.1	**83.5**	4.0
d_{PR}	3-D Ellipsoid	85.6	89.6	88.0	81.5	87.1	92.1	85.9	83.2	90.2	84.2	86.3	**86.8**	3.3
	2-D driven 3-D	93.1	92.9	89.2	87.1	91.5	92.2	87.9	85.9	87.1	89.8	87.9	**89.2**	2.4

FP is the number of pixels that have been falsely classified as vessel structure. The Hausdorff distance is applied to measure and visualize the deformations before and after 2-D driven 3-D optimization.

The evaluation regarding 2-D measurements is four-sided:

1. A simple intensity region growing segmentation is applied which is initialized by a manual seed point. The intensity range was chosen by a neuroradiologist based on his working experience with 3-D DSA data. The forward projections are compared to the 2-D gold standard segmentations.

2. The pure 3-D driven ellipsoid-based segmentation result (see section 5.3.1) is being forward projected to measure the overlap with the 2-D gold standard segmentation.

3. The forward projections of the novel 2-D driven 3-D segmentation approach are compared to 2-D gold standard segmentations. This allows judging the overlap match before and after 2-D/3-D adaptation.

4. Three additional 2-D DSA projections are selected that were **not** part of the 2-D/3-D adaptation process. These three 2-D DSA projections were again manually outlined. Than the 2-D driven 3-D segmentation result is forward projected against these three 2-D projections and the overlap is measured. This measurement allows to come up with a statement about the overall fit of the 2-D adapted 3-D segmentation result w.r.t. other 2-D projections.

5.4.2 Experimental Results

This section describes the segmentation results concerning the three different segmentation approaches. All experiments were performed on an Intel Core2 CPU with 2 GHz, 4GB of main memory and NVIDIA Quadro FX 2500M graphics card. The algorithms were completely implemented in C++ whereas the computation of the forward projection was done using OpenGL. The overall intension of incorporating 2-D information into the 3-D segmentation process is to be able to come up with quantitative measurements in 3-D that are taken on a valid base. Therefore, our experimental setup is split in two categories, i.e. phantom-based and patient-specific experiments.

Phantom Experiment

The vessel phantom (see Figure 5.6) is made up of a plastic tube exhibiting an inner diameter of 3.6mm and a wall thickness of 1.3mm. The phantom experiment was conducted in order to setup an ideal acquisition environment. This environment eliminates some disturbing factors in contrast to a real patient acquisition, i.e. there is no patient movement, the plastic tube was completely filled with contrast agent such that it is homogenously distributed without air blebs and the vessel diameter is known a priori. The phantom results are really promising. The quantitative results are illustrated within the Tables 5.1 and 5.2 (column P). Looking at Table 5.1 summarizing the results concerning the optimization projections: the 2-D driven

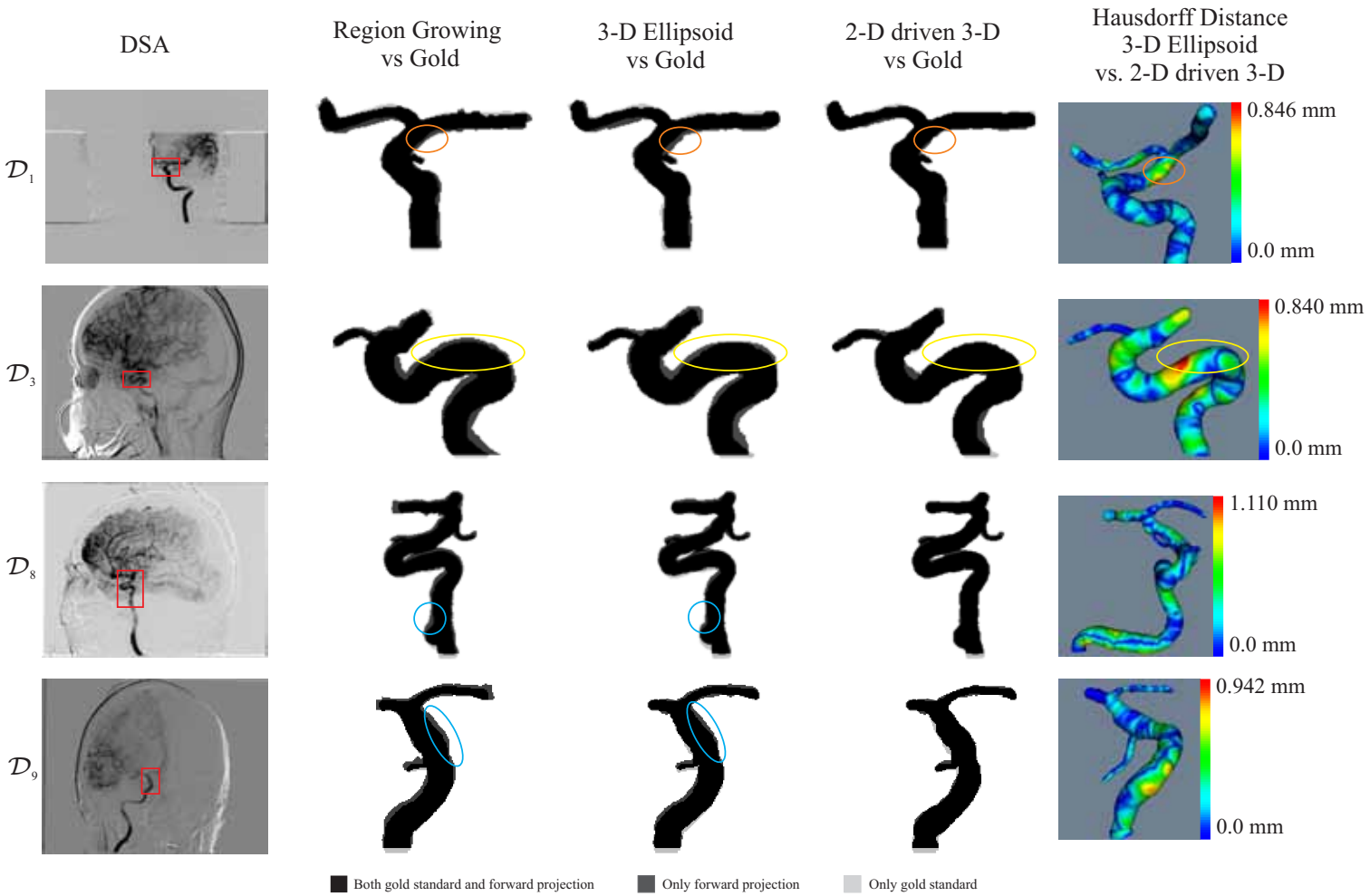

Figure 5.4: This set of images shows evaluation results concerning four datasets. On the left column one of the three projection images is illustrated that was used to adapt the 3-D ellipsoid segmentation. The three middle columns depict a 2-D comparison of the forward projections originating from three different vessel segmentation methods, i.e. region growing, 3-D ellipsoid and 2-D driven 3-D segmentation. The most right column gives a 3-D impression of the deviations. The meaning of the circles is described within the result section.

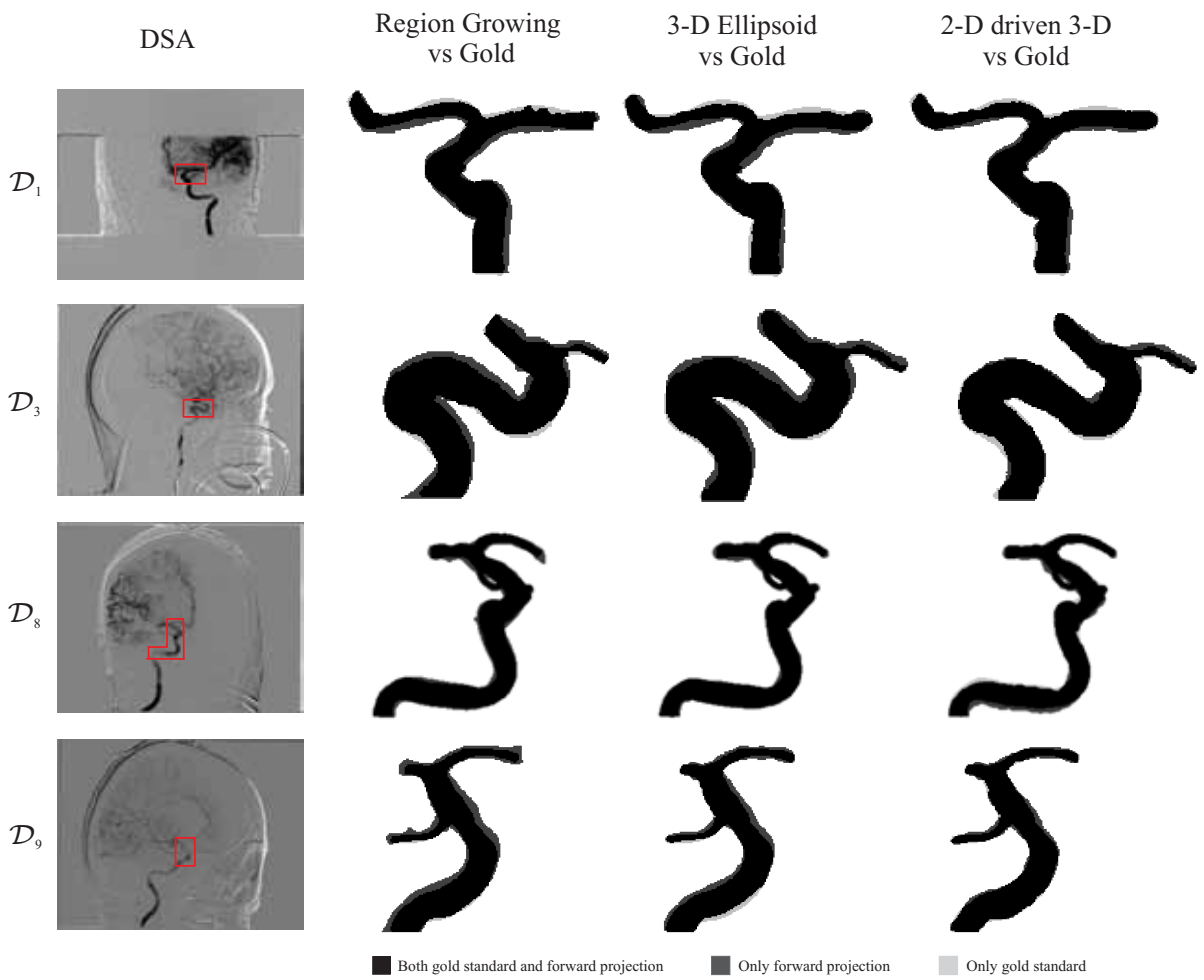

Figure 5.5: This set of images shows qualitative evaluation results concerning four datasets. The projections were ***not*** part of the optimization set in order to measure the overall fit of the 2-D driven 3-D segmentation approach. The three columns on the right depict a 2-D comparison of the forward projections originating from three different vessel segmentation methods, i.e. region growing, 3-D ellipsoid and 2-D driven 3-D segmentation.

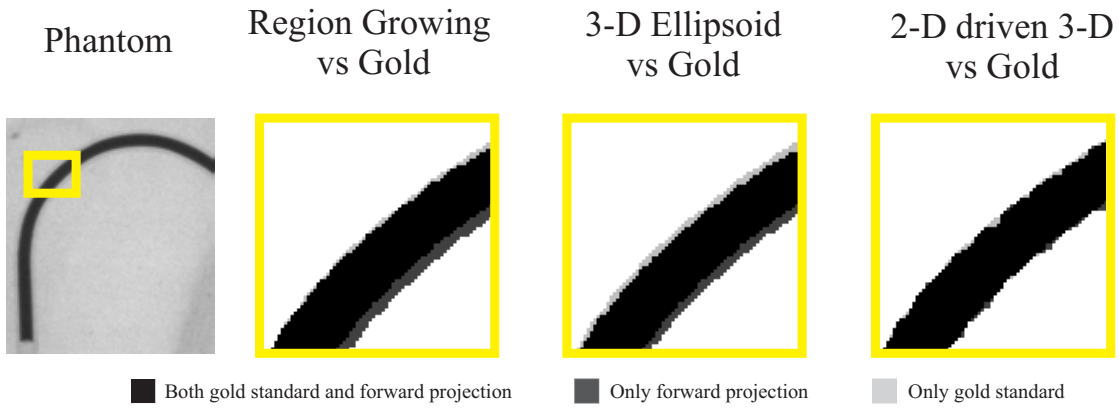

Figure 5.6: Qualitative results of the phantom-related experiments. The projections shown in this figure were part of the optimization set. The red box denotes the area of reconstruction. The yellow boxes represent the zoomed region for illustration purposes.

3-D approach shows an improvement of about 7% points against the 3-D ellipsoid-based segmentation and almost 13% over the result computed by region growing. Also the results for those projections which were not used for optimization show a clear outperformance of our 2-D driven 3-D method over the other two methods (see Table 5.2).

Patient-Specifc Experiments

This section describes the experiments that were conducted with patient-specific data. An overview about the segmentation results is given in Table 5.1. Figure 5.4 illustrates the qualitative results. Considering the quantitative results given in Table 5.1, it turns out that the 2-D driven 3-D vessel segmentation approach outperforms the other two segmentation methods.

Regarding the evaluation measurements within the optimization set (Table 5.1), the region growing approach achieves an overall fit of 89.1% (Dice) and 83.2% (Precision). The 3-D ellipsoid segmentation shows a slightly better result, i.e. 89.4% (Dice) and 87.0% (Precision). A major improvement, however, could be achieved by the 2-D driven 3-D segmentation approach, i.e. 95.2% (Dice) and 94.2% (Precision).

Moreover, the Table 5.2 shows that this novel 2-D/3-D segmentation method delivers better results as the other two techniques even for projections that have **not** been part of the optimization set. There, the average Dice coefficient and precision reveal 91.6% and 89.2% respectively. The region growing and 3-D ellipsoid-based segmentation end up on average with 90.0% and 90.9% for Dice - 83.5% and 86.8% for precision respectively.

Comparing the qualitative segmentation results of the region growing approach with the 3-D ellipsoid method, the vessel diameters appear slightly thicker within the region growing results (see Figure 5.4 blue circles). The 2-D/3-D adapted ellipsoid segmentation result is shown within the fourth column of Figure 5.4. The new algorithm deforms smoothly towards the boundary of the given 2-D gold standard

segmentation. The deformations are depicted using the Hausdorff distance before and after 2-D/3-D optimization. The orange and yellow circles within Figure 5.4 illustrate exemplarily the differences between the three segmentation results. The 2-D driven 3-D approach is able to fit to the gold standard segmentations in almost all regions. Those remaining regions that are not covered by the 2-D/3-D model originate due to external influence factors, e.g. vessel movement due to the beating heart or patient movement.

5.5 Discussion

When it comes to measurements of vessel diameters during treatment planning, 2-D DSA projections denote the gold standard image modality to perform these measurements. Therefore, this 2-D driven 3-D vessel segmentation method can be considered as a general approach to validate 3-D vessel segmentations based on 3-D DSA image data. Independent from the applied segmentation algorithm, it is possible to judge the 3-D segmentation result by means of forward projection and comparison with corresponding 2-D DSA projections. The new external energy force introduced in section 5.3.2 can be applied as regularizer for various 3-D vessel segmentation methods based on different mathematical principles, e.g. other parametric segmentation algorithms, level sets or graph-cuts. We applied the SSD as cost function due to the fact that we dealt only with segmentations in 2-D as well as in 3-D. Within the evaluation, three 2-D DSA projections were used to adapt the 3-D segmentation but this approach is open to incorporate as many projections as the user wants to be used. Another approach would be not to manually segment the vessel of interest within the 2-D DSA projections but to incorporate the projections as is. This would imply to use different cost functions for the 2-D/3-D external force, e.g. normalized cross correlation, pattern intensity, gradient difference etc. One might argue that the original 2-D edge information can be already integrated within the reconstruction process by manual outlining of all 133 2-D DSA projections used for reconstruction - and finally reconstruct a binary image volume. This, however, is not feasible within clinical routine because this manual outlining will take several hours. Our 2-D driven 3-D approach has been developed with respect to clinical workflows and aspects, i.e. during stent or coil planning physicians choose selected 2-D DSA projections to measure the vessel diameter or aneurysm neck size to decide which stent or coil type has to been used to get an optimal therapeutic outcome. Within the integrated 2-D/3-D segmentation framework, the adaptation of the 3-D vessel segmentation to the chosen 2-D projection can be easily done.

Moreover, this segmentation approach helps to reduce the influence of acquisition and reconstruction related factors as described during the introduction. Different reconstruction kernels [Kak 88, Buzu 08] exhibit inherently different edge enhancement leading to varying edge ramps (see Figure 5.1), i.e. the original edge information which is present within the 2-D DSA projections (being used for reconstruction) has not been used so far to drive the segmentation algorithm towards the real vessel edge. With the incorporation of the 2-D projections, however, this information is now used a second time (first for reconstruction and second for

vessel segmentation) within the new 2-D driven 3-D ellipsoid segmentation approach to ensure that the vessel edges of the 3-D fits to the edges given in 2-D.

A 3-D ellipsoid-based segmentation is used to approximate the vessel structures with a strong tubular regularizer. The advantages of this segmentation algorithm denotes the ability to adapt to local vessel branches and its deviations by interleaving ellipsoids as already mentioned in [Tyrr 07]. It reveals slightly better results (see Table 5.4 most right column) than the region growing approach because the 3-D ellipsoid segmentation is based on local adaptive threshold estimations using GMM's and not using one global threshold value. Due to this, it is possible to approximate the local intensity variations within the vessels (see Figure 5.3) in a better way. While performing a forward projection onto the three selected 2-D projections, the 3-D information is lost. The deformations computed within 2-D may cause changes within the 3-D segmentation that may lead towards unrealistic vessel appearance. Now, the advantage of the parametric 3-D vessel segmentation comes into play because those deviations can be easily avoided by the internal energy force introduced in section 5.3.1. This internal force watches the parameter changes of the interleaved ellipsoids concerning rotation, scaling and translation and penalizes those changes featuring highly non-tubular vessel structures.

The overall 2-D driven 3-D segmentation results look promising even if there are still some remaining areas where our 2-D/3-D adaptation could not properly deform towards the 2-D vessel boundaries as depicted within Figure 5.3 red circles. There are three reasons which might cause this behavior:

1. Patient movement between the different 2-D DSA projections may cause an area of conflict showing an inconsistent vessel situation.

2. The 2-D DSA projections were arbitrarily selected with the only condition that the vessels are depicted from different viewing angles. This may imply vessel movement between the projections due to different phases of the cardiac cycle.

3. The internal force keeps the model from deformation towards these areas because the gain of cost reduction concerning the external force is too less compared to the increase of the costs induced by the internal term.

5.6 Conclusion

The major contribution of this chapter denotes the incorporation of 2-D projection information into a 3-D vessel segmentation method for 3-D DSA data. The results indicate that the match between the forward projection of 3-D segmentation volume with manual outlined 2-D DSA vessel segmentations is not identical as it is supposed to be for an ideal calibrated case. This occurs because of the influcence factors that appear during a 3-D DSA acquisition. The 2-D driven 3-D method opens up the possibility to drive the 3-D vessel segmentation results towards previously selected 2-D information. This step enables to perform quantitative vessel measurements in 3-D on a more valid base. This approach serves as a key module towards an automatic 2-D/3-D vessel segmentation framework.

The 2-D segmentation module introduced in Chapter 3 delivers the corresponding 2-D segmentation. The combination of the methods outlined in part one and two of this thesis will boost the feasibility of this 2-D driven 3-D approach within a clinical environment.

The next part of this thesis takes the 3-D segmentation results obtained within the previous chapters and investigates the impact of different mesh configurations and resolutions on the simulation results. Furthermore, this 2-D driven 3-D segmentation approach delivers two vessel segmentations per dataset which provides the opportunity to evaluate the geometry related effects on the hemodynamic simulation result.

Part III

Hemodynamic Simulations

CHAPTER 6

Mesh Size Evaluation on Flow Velocity and Wall Shear Stress

As outlined within the introduction part of this thesis (see Chapter 1.4), the hemodynamic simulation workflow consists of four major steps. This chapter will shed light on the second step of this workflow and its impact on the simulation result. Two different vessel geometries, exhibiting a side wall and a basilar tip aneurysm, were taken to evaluate different mesh size resolutions and compare tetrahedral versus polyhedral mesh type elements. A set of mesh configurations was constructed showing spatially varying surface and volume mesh models with and without boundary layers. The main goal of this chapter is to find a good trade-off between spatial accuracy, convergence stability and computation time w. r. t. future clinical simulation applications. This chapter is explicitly not on numerical convergence or solver related issues. The evaluation is performed comparing WSS distributions on the model wall and point-based velocity measurements. The results indicate that polyhedral meshes are more stable in terms of computational convergence with less computation time. Major parts of this chapter have been already published in [Spie 11c].

6.1 Motivation

More and more cerebral aneurysms are incidentally detected as already stated within the introduction part of this thesis due to advances in the field of medical imaging techniques such as 64 slice CT or MRI at 3T. So far, the reason for growth or rupture of an aneurysm is not entirely understood but it is assumed that the hemodynamic within an aneurysm plays an important role [Jou 08]. Geometric factors, e. g. lesion size and aspect ratio [Ujii 01, Nade 04, Ragh 05] are also considered to determine the risk of rupture. However, even hemodynamic information together with geometric aspects have so far proven insufficient for the cal-

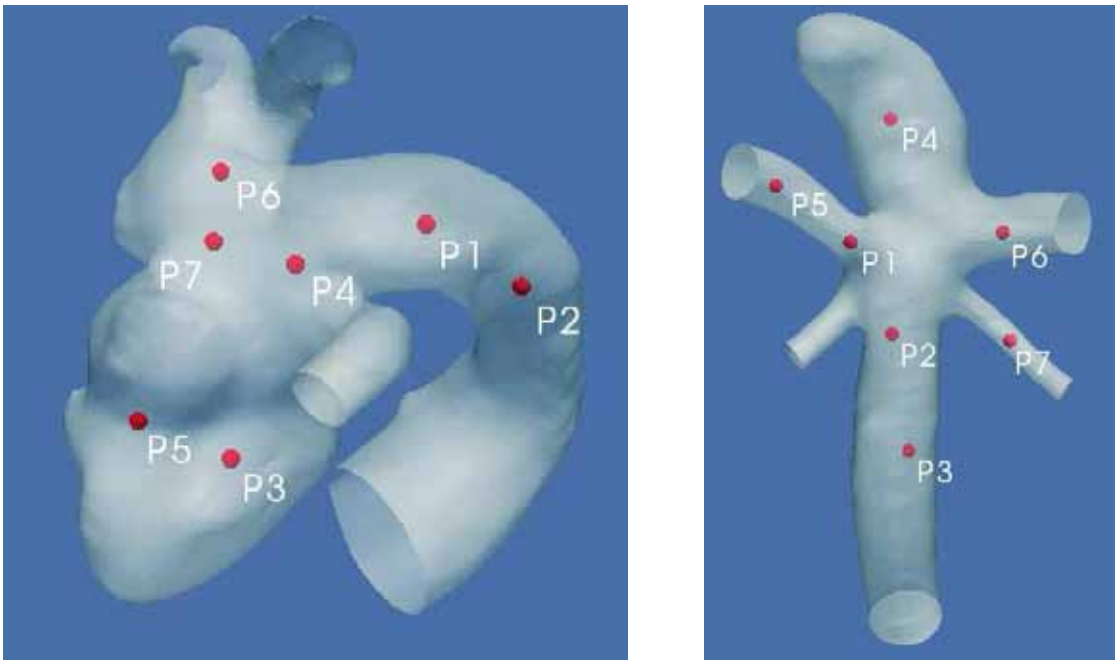

(a) Internal carotid side wall aneurysm (b) Basilar tip aneurysm

Figure 6.1: 3-D mesh representations of the evaluated aneurysms: (a) Case 1 depicts an internal carotid aneurysm. (b) Case 2 illustrates a basilar tip aneurysm. The red spheres show the positions of the velocity measurement points distributed in the vicinity of the aneurysms, i. e. at the inlet, within the aneurysm and at the outlet.

culations of a reliable patient-specific risk index for a particular aneurysm. Other biological mechanisms and systemic conditions may also contribute to aneurysm rupture. To assess intra-aneurysmal hemodynamic, CFD simulations have been employed with patient-specific geometries derived from clinical image data in [Stei 03, Karm 04, Shoj 04, Hoi 04, Cebr 05a, Cebr 05c, Venu 07]. Other kinds of simulation techniques are imaginable to perform blood flow simulations like Lattice-Boltzmann methods [Goet 06]. A reliable patient-specific CFD-based blood flow simulation will be strongly influenced by two factors:

1. Geometric accuracy of the patient-specific vascular model dependent on the used segmentation method.

2. Boundary conditions and simulation parameters such as inflow blood speed, blood density/viscosity and rigid walls.

Patient-specific boundary conditions can either be obtained through invasive measurements during treatment (i. e. pressure catheder) or, as demonstrated recently, by 2D phase-contrast magnetic resonance imaging (2D pcMRI) providing the time-varying blood flow profile at the inlet of the computational model as shown in [Karm 08].

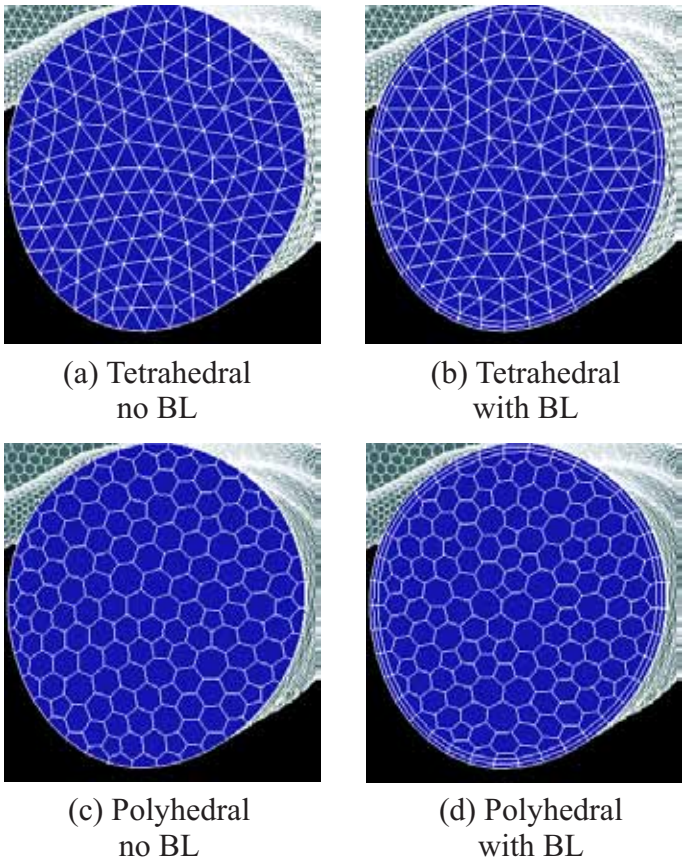

Figure 6.2: Meshing example regarding case 2. (a) and (c) show tetrahedral and polyhedral meshes. (b) and (d) depict tetrahedral and polyhedral-based meshes with a boundary layer.

The sensitivity of other computational parameters on the simulation results, in particular mesh size and mesh design, have not been evaluated in detail for this particular vascular pathology. The hemodynamic situation in cerebral aneurysms is favorable to be simulated using CFD: blood flow in cerebral vessels is always antegrade as compared to the blood flow in the aorta with modest pulsatility. Unless downstream vascular disease is present such as a stenotic lesion distal to the aneurysm, vascular resistance is low. Reynolds numbers are low (≤ 100) and therefore no turbulence flow can be expected. Due to these favorable conditions, most studies so far have successfully employed simple meshes such as tetrahedral meshes with no adaptation or boundary layer. Still, the assessment of the mesh quality is considered as a very important task because inaccurate meshing including high skewness of cells or coarse spatial resolution may lead to non-valid CFD results and thus leading to potentially inaccurate local velocities or WSS patterns.

In particular for a future clinical CFD-based diagnostic and treatment tool, the performed simulations have to be fast and stable. The mesh size has to be as small as possible but concerning accuracy as fine as necessary to avoid numerical prediction errors (velocity and WSS). Two different approaches are known

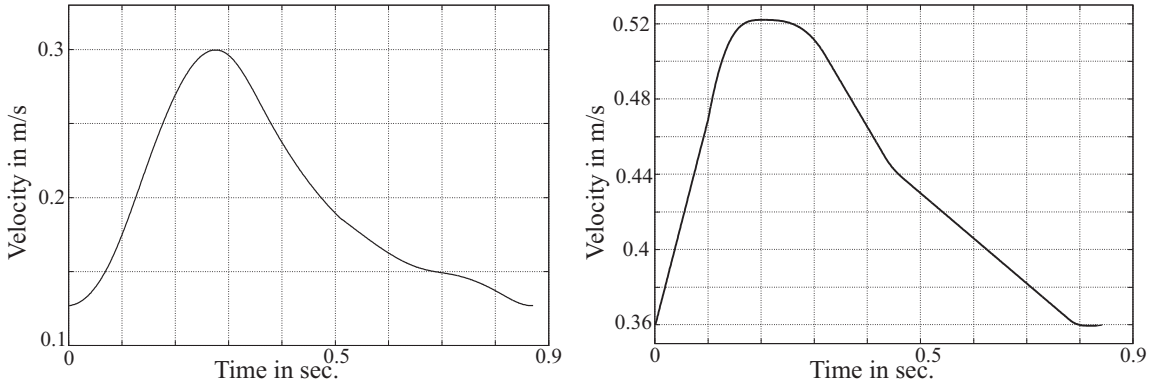

(a) PC-MRI measured inlet waveform (b) Idealized inlet waveform

Figure 6.3: Inlet velocity waveforms applied for pulsatile simulations. Left: Phase constrast MRI measured blood flow waveform used for case 1. Right: Idealized waveform used for case 2. This waveform is inspired by [Grod 01].

to experimentally verify the mesh suitability for CFD simulation introduced by [Prak 01]:

1. Comparison of CFD results with experimental measured data.
2. Mesh independence analysis

Within this chapter, the second approach is applied to evaluate the impact of varying surface and volume mesh resolutions as well as different meshing techniques represented by polyhedral [Oaks 00] and tetrahedral meshes. In particular, the question which mesh granularity can be considered as accurate enough to get reliable blood flow simulation results is investigated with time-restraints existing for future clinical applications.

Two cerebral vessel geometries were investigated, i. e. a sidewall aneurysm of the internal carotid artery and a basilar bifurcation aneurysm as depicted in Figure 6.1. Blood flow velocity and WSS distributions according to varying spatial mesh resolutions and configurations (polyhedral vs. tetrahedral elements) are evaluated. Effects of boundary layer regarding WSS are studied by means of comparing boundary layer-based meshes with those exhibiting no boundary layer. Pulsatile simulations are performed with varying time-step to determine the largest step delivering still valid simulation results.

6.2 Methods

3-D DSA image data [Hera 06b] of the two cerebral aneurysms (see Figure 6.1) were acquired during endovascular interventions using Siemens C-Arm System (AXIOM Artis dBA, Siemens AG Healthcare Sector) in Erlangen (Germany) and Houston (USA). 3-D image reconstructions of both aneurysms led to an image volume for Case 1 of $138.24 \times 138.24 \times 57.72$mm with a voxel spacing of $0.27 \times 0.27 \times 0.13$mm and for Case 2 $97.28 \times 97.26 \times 66.43$mm (voxel spacing $0.19 \times 0.19 \times 0.1$mm)

respectively. The non-isotropic voxel spacing comes from image downsampling in x/y direction due to segmentation and memory issues. For mesh generation and smoothing, the Marching Cubes [Lore 87] and a Laplacian-based smoothing algorithm (VTK Kitware Inc.) were applied as an additional step. The image data was stored as a STL file providing the input data for the meshing software GAMBIT (ANSYS Inc.). The mesh corresponding to case one exhibits a volume of 537mm^3 and the mesh of the second case of 282mm^3. The maximal diameters of the inlet and outlets are as follows:

- Case one: inlet 5.2mm, outlet1 2.0mm, outlet2 2.3 mm and outlet3 2.6mm.
- Case two: inlet 3.3mm, outlet1 2.5mm, outlet2 1.5mm, outlet3 1.5mm and outlet4 2.4mm.

Different surface mesh resolutions were generated by using the GAMBIT curvature size function [Coop 07]. This function constraints the angle between outward-pointing normals for any two adjacent surface triangles. That leads to a denser mesh resolution in areas exhibiting high curvature like the aneurysm and coarser resolution in more flat regions. Four parameters define the curvature size function, i. e. angle, growth, max. and min. triangle size. Table 6.1 contains a detailed overview of the applied curvature size function parameters as well as the set of meshes. The final number of triangles representing the surface mesh is automatically determined by the meshing algorithm according to the chosen parameter values and the geometry. The resolution of the surface mesh rules the final number of tetrahedral control volume elements - the larger the number of surface triangles, the larger is the number of tetrahedral control volume elements.

To study the effects of boundary layer usage, almost all meshes (see Table 6.1) were generated without and with boundary layers [Loeh 00, Gari 00]. Since a boundary layer approximates the boundary of the vessel tubes with prisms as shown in Figure 6.2, this automatically results in a higher number of tetrahedral control elements as compared to meshes without a boundary layer. The boundary layers were created through GAMBIT's boundary layer algorithm featuring two levels. The height of the first level was chosen to be 0.04 mm and the second one 20% larger, i. e. 0.048 mm. The mesh quality in terms of aspect ratio and surface/mesh skewness is summarized in Table 6.2.

Table 6.1: Set of Meshes - Case 1 and Case 2. Tet. and Poly. abbreviate tetrahedral and polyhedral respectively. BL denotes boundary layer.

	#Tet. Cells (BL)	Diff. No-BL to BL for Tet. Cells in %	#Poly. Cells (BL)	Diff. No-BL to BL for Poly. Cells in %	Diff. Poly. vs. Tet. in %	Diff. Poly. vs. Tet. BL in %	Diff. Poly. BL vs. Tet. non-BL in %	Max./Min. Triangle	Growth	Angle
Case 1	13841 (-)	-	5,119 (-)	-	-	-	-	6 / 0.001	1.2	25
	26,702 (40,699)	52.4	7,283 (24,206)	232.4	-72.7	-40.5	-9.3	3.6/0.001	1.2	14
	52,374 (77,252)	47.5	12,467 (31,548)	153.1	-76.2	-59.2	-39.8	1.8/0.001	1.1	14
	76,493 (109,638)	43.3	17,695 (38,564)	117.9	-76.9	-64.8	-49.6	1.2/0.001	1.2	6
	86,621 (107,336)	23.9	18,681 (32,012)	71.4	-78.4	-70.2	-63.0	0.4/0.001	1.1	12
	106,010 (124,041)	17.0	22,297 (35,866)	60.9	-79.0	-71.1	-66.2	0.36/0.001	1.1	12
	115,014 (160,771)	39.8	25,540 (48,687)	90.6	-77.8	-69.7	-57.7	0.3/0.001	1.1	10
	189,625 (202,565)	6.8	37,495 (53,794)	43.5	-80.2	-73.4	-71.6	0.28/0.001	1.1	10
	197,098 (228,097)	15.7	38,991 (58,879)	51.0	-80.2	-74.2	-70.1	0.27/0.001	1.1	10
	231,354 (258,481)	11.7	45,158 (65,707)	45.5	-80.5	-74.6	-71.6	0.26/0.001	1.1	10
Case 2	31,696 (47,311)	49.3	8,814 (26014)	195.1	-72.2	-45.0	-17.9	0.42/0.001	1.2	17
	43,063 (59,914)	39.1	10,843 (21,153)	95.1	-74.8	-64.7	-50.9	0.37/0.001	1.17	17
	56,176 (75,447)	34.3	13,280 (24,978)	88.1	-76.4	-66.9	-55.5	0.34/0.001	1.12	15
	75,469 (100,587)	33.3	16,795 (30,435)	81.2	-77.7	-69.7	-59.7	0.32/0.001	1.10	13
	98,399 (129,516)	31.6	21,108 (37,221)	76.3	-78.6	-71.3	-62.2	0.3/0.001	1.10	10
	114,227 (142,336)	24.6	23,846 (39,833)	67.0	-79.1	-72.0	-65.1	0.28/0.001	1.10	10
	148,625 (159,797)	7.5	30,167 (44,652)	48.0	-79.7	-72.1	-70.0	0.25/0.001	1.09	8
	184,226 (219,922)	19.4	36,845 (65,398)	77.5	-80.0	-70.3	-64.5	0.24/0.001	1.10	6
Mean		**29.2**		**93.8**	**-77.7**	**-66.5**	**-55.6**			

The tetrahedral meshes were imported into the simulation software Fluent (ANSYS Inc.). A conversion algorithm, part of the Fluent CFD solver, was used to generate for each tetrahedral mesh a corresponding polyhedral mesh. The surface of the vessel models was assumed to be rigid-walls and no slip as shear condition. Blood was modeled as an incompressible Newtonian fluid with a density of 1050 kg/m^3 and a viscosity of 0.004 N/m^2 [Hass 04].

The boundary conditions for all conducted simulations were as follows: the inlet was considered as velocity inlet and all outlets were modeled as pressure outlet zero. A constant inflow rate of 0.3 m/s and 0.5 m/s was applied in the steady simulations for the first and second case respectively. In pulsatile simulations two different inflow waveforms were used (Figure 6.3): for the first case a MRI measured waveform and for the second case, we applied a waveform taken from a former publication [Grod 01] which was measured with ultrasound since there was no patient-specific blood flow profile measured with MRI or ultrasound. Similar blood flow velocity profiles concerning the basilar artery were also measured in [Kato 02]. Steady-state simulations were considered as converged if the relative residuals fall under 0.001 (i. e. the absolute values of the residuals were reduced by three orders of magnitude). In addition, the mass flow was measured to prove convergence by subtracting outflow from inflow. All converged solutions exhibit a mass flow difference between inflow and outflow of $\pm 5e^{-5}$ g/s.

Seven points were defined to measure the simulated blood flow velocity occurring in the environment of the aneurysm. In the first case, two points were placed in the inlet region of the aneurysm, three inside the aneurysm dome and two in the outlet region of the aneurysm. In second case, one point was located within the inlet vessel part, another one inside the aneurysm dome and the remaining points were distributed near the aneurysm neck and within the outlets respectively. The different point distributions between the first and second case are reflected in the different vessel geometries, i. e. side wall vs. tip aneurysm. Figure 6.1 gives a good overview about distributions of the measurement points for both cases. In reality, the points are located inside the geometry. The simulation experiments performed in this chapter can be separated into three types:

1. Starting with the given number of tetrahedral cells we compare this number with the corresponding number of polyhedral cells and also without and with boundary layer.

2. A series of steady state simulations is performed to compare tetrahedral vs. polyhedral meshes in terms of velocity and WSS. This series is supposed to shed light on the question what spatial resolution is required to avoid inaccurate CFD results caused by unsuitable CFD meshes. The results were analyzed in terms of

   - Computational convergence (number of iterations)
   - Velocity convergence
   - Wall shear stress convergence

Table 6.2: Overview mesh quality, i. e. aspect ratio (AR) and skewness (SN) for surface and mesh.

	# Tet. Cells (BL)	# Poly. Cells (BL)	Surface		Mesh	
			AR	SN	AR	SN
Case 1	26,702 (40,699)	7,283 (24,206)	1-1.76	0-0.43	1-4	0-0.75
	52,374 (77,252)	2,467 (31,548)	1-1.52	0-0.40	1-3.19	0-0.77
	76,493 (109,638)	17,695 (38,564)	1-1.60	0-0.48	1-3.34	0-0.80
	86,621 (107,336)	18,681 (32,012)	1-1.74	0-0.51	1-3.52	0-0.77
	106,010 (124,041)	22,297 (35,866)	1-1.63	0-0.46	1-3.28	0-0.78
	115,014 (160,771)	25,540 (48,687)	1-1.53	0-0.45	1-3.34	0-0.74
	189,625 (202,565)	37,495 (53,794)	1-1.62	0-0.49	1-3.31	0-0.77
	197,098 (228,097)	38,991 (58,879)	1-1.55	0-0.46	1-3.28	0-0.77
	231,354 (258,481)	45,158 (65,707)	1-1.44	0-0.40	1-3.43	0-0.75
Case 2	31,696 (47,311)	8,814 (26014)	1-1.62	0-0.49	1-3.10	0-0.76
	43,063 (59,914)	10,843 (21,153)	1-1.62	0-0.49	1-3.22	0-0.76
	56,176 (75,447)	13,280 (24,978)	1-1.41	0-0.38	1-3.10	0-0.78
	75,469 (100,587)	16,795 (30,435)	1-1.42	0-0.38	1-3.31	0-0.76
	98,399 (129,516)	21,108 (37,221)	1-1.63	0-0.50	1-3.19	0-0.77
	114,227 (142,336)	23,846 (39,833)	1-1.38	0-0.36	1-3.25	0-0.76
	148,625 (159,797)	30,167 (44,652)	1-1.58	0-0.47	1-3.34	0-0.75
	184,226 (219,922)	36,845 (65,398)	1-1.56	0-0.46	1-3.31	0-0.77

Also these steady state simulations were repeated with boundary layer-based meshes to evaluate both the effects on the WSS distribution and the increased complexity concerning the mesh generation process.

3. A series of pulsatile simulations is conducted according to varying time steps, i. e. 1ms, 5ms and 10ms. The pulsatile simulations for both cases were only performed with the highest resolved boundary layer-based polyhedral meshes (see Table 6.1 row 9 and 17). A total of 3 cardiac cycles were computed and only the results of the 2^{nd} and 3^{rd} cardiac cycle are stored to avoid transient effects as much as possible.

The Area-Weighted-Average WSS distribution WSS_{AW} was used to express and compare WSS distributions between meshes in terms of numbers. It is defined as follows:

$$\mathrm{WSS}_{AW} = \frac{1}{A} \sum_{i=1}^{n} \phi_i \, |A_i| \tag{6.1}$$

where A denotes the total area being considered and ϕ_i describes the wall shear stress associated with the facet area A_i. For the analysis the complete aneurysmal surface was included but without considering the surrounding vessel segments.

Since tetrahedral based meshes are considered as state-of-the-art within the CFD simulation community [Luon 09], they are taken as the golden base. Thus, the differences in Tables 6.1, 6.3 and 6.4 between polyhedral and tetrahedral meshes,

i. e. the number of volume elements, WSS and iterations are computed by the following formula:

$$\text{diff}_i = \frac{x_i \cdot 100}{y_i} - 100 \tag{6.2}$$

$$\text{with } i \in \{ \text{\#iter, Area-Weighted-Average WSS} \} \tag{6.3}$$

where x_i and y_i denote values given from polyhedral and tetrahedral mesh respectively.

6.3 Results

6.3.1 Cell Numbers

Considering Table 6.1 last row, a boundary layer increased the number of volume elements (NVE) for tetrahedrals about 29% (column 3) and for polyhedrals about 93% (column 5) on average. Polyhedrals reduced the NVE compared to tetrahedrals about 77% (column 6) on average. Polyhedral meshes with boundary layer needed 66% (column 7) less NVE compared to the corresponding boundary layer based tetrahedrals meshes. Even polyhedral meshes with boundary layer exhibited less than 55% NVE than tetrahedral meshes without a boundary layer.

6.3.2 Convergence

Computational Convergence

Polyhedral meshes exhibited a far better convergence as tetrahedral ones as can be easily seen in Table 6.3 and 6.4 (column 3 and 4). Polyhedral meshes needed ca. 60% (see Table 6.3 and 6.4, -63.7%, -54.8%, -66.6% and -60.7%) less iterations than the corresponding tetrahedral ones.

Velocity Convergence

The blood flow velocity generally converged with increasing mesh size. Figure 6.4 illustrates the point-based measurement results regarding the first and second case. For both cases, there were no significant differences between the simulated velocities of polyhedral and tetrahedral meshes. The velocity fluctuations rapidly decreased for mesh sizes larger than 125,000 tetrahedral and 22,000 polyhedral elements in case 1 and 60,000 tetrahedral and 16,000 polyhedral elements for case 2 respectively (see Figure 6.4 red bars). From this point on, these mesh sizes are considered as convergence criterion and only the results of meshes larger than that are taken into account for the following velocity and WSS analysis.

Table 6.3: Summary of the results. Tet. and Poly. abbreviate tetrahedral and polyhedral respectively. Diff and Iter denote difference and iterations. WSS is measured in Pascal.

	No Boundary Layer					
	#Tet. (Poly.) Cells	#Iter. Tet. (Poly.)	Difference #Iter Tet. vs. Poly. [%]	WSS Tet.	WSS Poly.	Difference WSS Tet. vs. Poly [%]
Case 1	13,841 (5,119)	129 (58)	-55.0	4.60	4.66	1.3
	26,702 (7,283)	169 (72)	-57.4	5.39	5.31	1.5
	52,374 (12,467)	238 (98)	-58.8	5.98	5.73	-4.2
	76,493 (17,695)	225 (102)	-54.7	6.33	5.94	-6.2
	86,621 (18,681)	384 (134)	-65.1	6.39	6.03	-5.6
	106,010 (22,297)	377 (151)	-60.0	6.51	6.07	-6.8
	115,014 (25,540)	297 (131)	-55.9	6.33	6.08	-4.0
	189,625 (37,495)	987 (213)	-78.4	6.82	6.59	-3.4
	197,098 (38,991)	815 (214)	-73.7	6.89	6.59	-4.4
	231,354 (45,158)	1142 (248)	-78.3	7.01	6.69	-4.6
Mean			**-63.7**	**6.76**	**6.49**	
σ				**0.22**	**0.20**	
Uncertainty				**3.20%**	**3.14%**	
Case 2	31,696 (8,814)	242 (111)	-54.1	5.91	5.26	12.4
	43,063 (10,843)	378 (176)	-53.7	7.18	6.20	-13.7
	56,176 (13,280)	365 (185)	-49.3	7.06	6.51	-7.8
	75,469 (16,795)	437 (202)	-53.8	7.33	6.84	7.3
	98,399 (21,108)	462 (211)	-54.3	7.43	7.15	-3.7
	114,227 (23,846)	496 (230)	-53.6	7.47	7.23	-3.2
	148,625 (30,167)	714 (269)	-62.3	7.62	7.45	-2.1
	184,226 (36,845)	934 (399)	-57.3	7.70	7.66	1.2
Mean			**-54.8**	**7.51**	**7.27**	
σ				**0.12**	**0.23**	
Uncertainty				**1.6%**	**3.18%**	

Table 6.4: Summary of the results. Tet. and Poly. abbreviate tetrahedral and polyhedral respectively. Diff and Iter denote difference and iterations. WSS is measured in Pascal.

	With Boundary Layer					
	#Tet. (Poly.) Cells	#Iter. Tet. (Poly.)	Difference #Iter Tet. vs. Poly. [%]	WSS Tet.	WSS Poly.	Difference WSS Tet. vs. Poly [%]
Case 1	40,699 (24,206)	170 (77)	-54.7	5.48	5.45	-0.5
	77,252 (31,548)	252 (109)	-56.8	5.93	5.82	-1.9
	109,638 (38,564)	255 (115)	-54.9	6.20	6.00	-3.2
	107,336 (32,012)	346 (139)	-59.8	6.02	6.04	0.33
	124,041 (35,866)	443 (154)	-62.2	6.38	6.14	-3.8
	160,771 (48,687)	331 (147)	-55.6	6.38	6.13	-3.9
	202,565 (53,794)	891 (209)	-76.5	6.63	6.42	-3.2
	228,097 (58,879)	2404 (241)	-90.0	6.68	6.49	-2.8
	258,481 (65,707)	1804 (258)	-85.7	6.78	6.56	-3.2
Mean			**-66.6**	**6.62**	**6.40**	
σ				**0.12**	**0.14**	
Uncertainty				**1.79%**	**2.11%**	
Case 2	47,311 (26,014)	256 (123)	-51.9	5.98	5.19	-13.2%
	59,914 (21,153)	324 (180)	-44.4	6.84	6.03	-11.9%
	75,447 (24,978)	353 (182)	-48.4	9.06	6.44	-28.9%
	100,587 (30,435)	450 (214)	-52.4	7.11	6.53	-8.1
	129,516 (37,221)	563 (236)	-58.1	7.19	6.80	-5.4
	142,336 (39,833)	1705 (266)	-84.4	7.22	6.93	-4.4
	159,797 (44,652)	684 (253)	-63.0	7.29	7.02	-3.6
	219,922 (65,398)	1902 (320)	-83.1	7.31	7.12	-2.6
Mean			**-60.7**	**7.22**	**6.88**	
σ				**0.06**	**0.17**	
Uncertainty				**0.84%**	**2.50%**	

Considering the data meeting the convergence criterion given above, the mean uncertainty of the simulated velocities over all points is as follows:

- Case 1 Tetrahedral/Polyhedral - 6.3%/4.4%
- Case 2 Tetrahedral/Polyhedral - 1.8%/1.9%

Wall Shear Stress Convergence

This section describes the WSS distribution between polyhedral and tetrahedral meshes with and without boundary layer usage. First, the results and findings of non-boundary layer meshes are presented and later in this section the results of boundary layer-based meshes are shown and compared to those without a boundary layer.

The WSS results obtained without using boundary layer are presented in Figure 6.5 and 6.6 left hand side. The WSS pattern of polyhedral meshes appeared more homogeneous than the tetrahedral ones. This is illustrated by the yellow circles in Figure 6.5 on the left. Moreover, it turned out that polyhedral meshes were able to resolve significant WSS pattern with far less elements than the corresponding tetrahedral ones (see Figure 6.5 red circles).

Table 6.3 (column 5/6) shows a detailed comparison regarding WSS between tetrahedral and polyhedral meshes without boundary layer. Convergence behavior can be seen for the mesh size variations for both cases. All values highlighted in gray meet the convergence criterion and thus, being considered for the statistics, i. e. mean, σ and uncertainty. In case 1, the mean WSS is 6.76Pa$\pm$0.22 Pa (tetrahedral) compared to 6.49Pa$\pm$0.20 (polyhedral). In case 2, we have 7.51Pa$\pm$0.12 (tetrahedral) against 7.27Pa$\pm$0.23 (polyhedral). The results for meshes with boundary layer are shown in Table 6.4. Again, convergence behavior can be seen for mesh size variations with boundary layer for both cases. In case 1, the mean WSS is 6.62Pa (tetrahedral) compared to 6.40Pa (polyhedral). In case 2, 7.22Pa (tetrahedral) against 6.88Pa (polyhedral).

No boundary layer could be generated regarding the polyhedral mesh with the fewest number of volume elements (see Table 6.1 second row) because its approximation of the original vessel geometry is too coarse. Thus, there is no comparison to the corresponding tetrahedral mesh. The WSS patterns, obtained with a boundary layer-based mesh, are depicted in Figure 6.5 and 6.6 (right side). The observations are as follows:

1. Generally, WSS pattern appeared smoother and better developed than those having no boundary layer.
2. The differences, however, became more and more negligible with increasing mesh size especially when comparing the highest resolved meshes as illustrated in the bottom row of Figure 6.5 and 6.6.

The primary WSS pattern was also visible and recognizable without a boundary layer except for the meshes shown in the top row of Figure 6.5 and 6.6. Here,

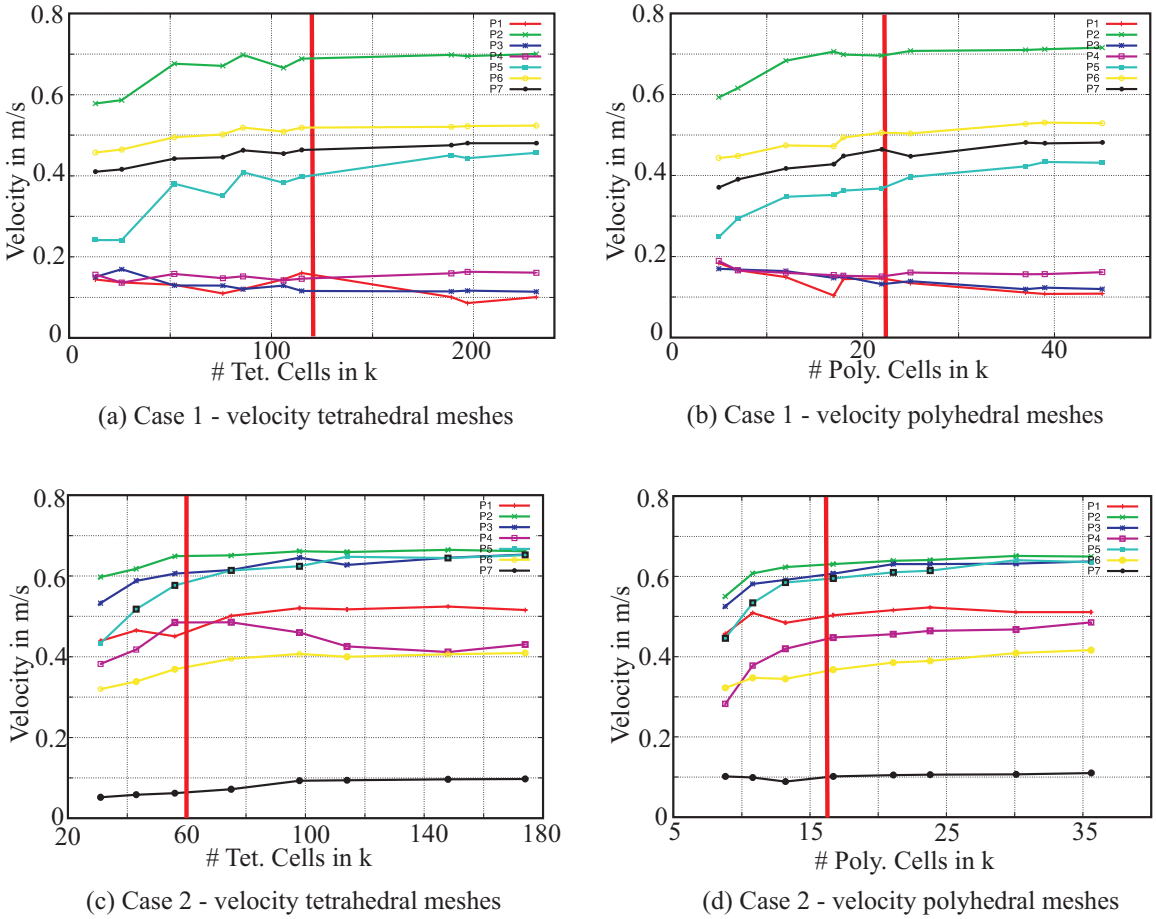

(a) Case 1 - velocity tetrahedral meshes

(b) Case 1 - velocity polyhedral meshes

(c) Case 2 - velocity tetrahedral meshes

(d) Case 2 - velocity polyhedral meshes

Figure 6.4: Velocity measurements for different mesh sizes. Top row depicts the velocity results for the first case. Bottom row illustrates the velocity values for the second case. The simulated velocities converge with increasing meshes. An increase of the mesh resolution leads to a convergence of the simulated velocity values for all point measurements. The red bar shows the border for convergence. In our study, all meshes left of the red bar are considered as non-converged velocities.

the WSS patterns considerably differ to the ones with boundary layer. But this is also due to the fact that a boundary layer-based mesh automatically exhibits more tetrahedral/polyhedral elements.

6.3.3 Pulsatile Simulation Effects of Varying Time Step Size

The WSS distributions between the pulsatile simulations with different time step sizes were negligible considering the results at the moment of systole. This is shown in Figure 6.7 and 6.8. Table 6.5 summarizes the differences in the Area-Weighted-Average WSS distribution between the different pulsatile simulations averaged over the second and third cardiac cycle. The computation time significantly decreased as indicated in Table 6.5 column 2. However, while increasing the computational time step size for the Fluent CFD solver there are some important issues coming up: a) the transition from one cardiac cycle to the next cardiac cycle

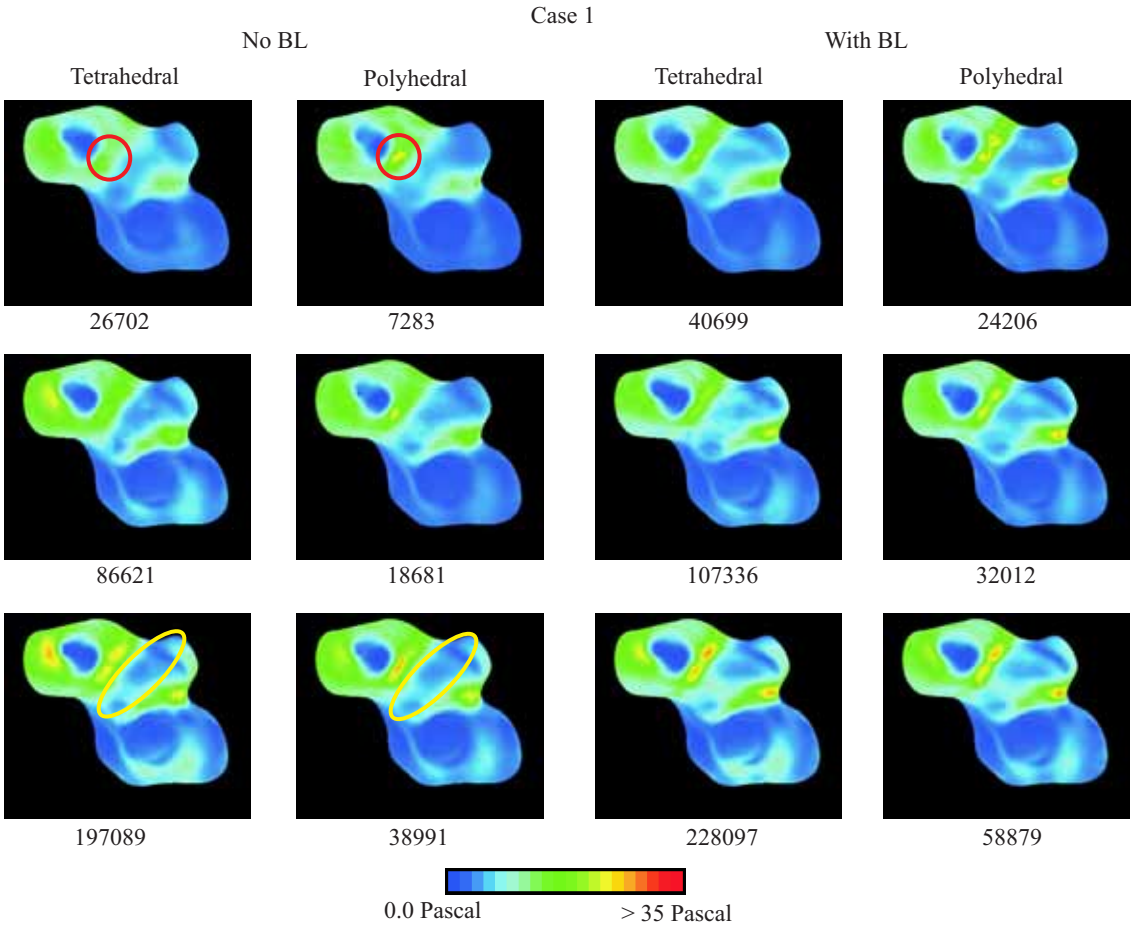

Figure 6.5: WSS distribution for polyhedral and tetrahedral meshes in comparison. Polyhedral meshes were also able to represent significant WSS pattern with fewer cells than tetrahedral ones as marked by the red circles. The numbers below the individual figures denote the number of cells of the mesh.

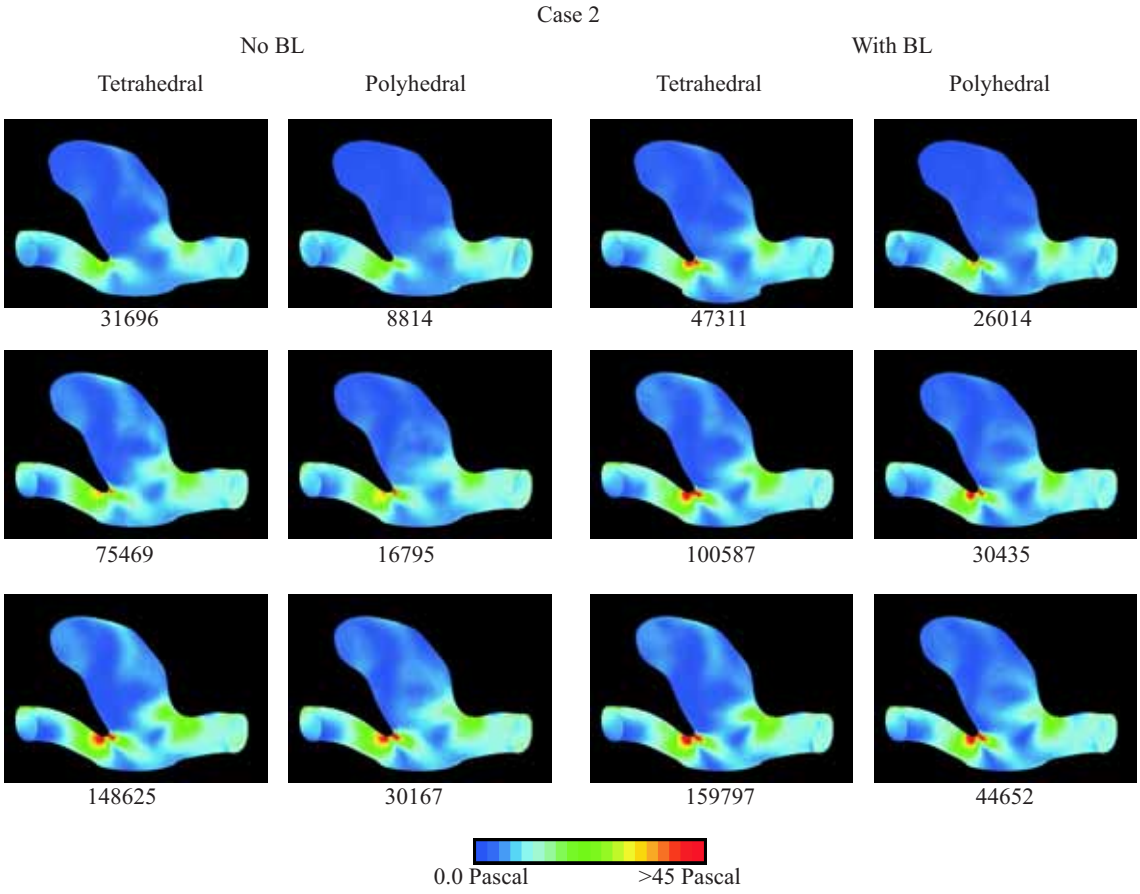

Figure 6.6: WSS distribution for polyhedral and tetrahedral meshes in comparison to boundary layer-based meshes. The numbers below the individual figures denote the number of cells of the mesh.

Table 6.5: Pulsatile WSS simulation results - Case 1 and Case 2. CT and TS abbreviate computation time and time step.

		Wall Shear Stress	
	CT [h] (TS [sec.])	Mean	σ
Case 1	12 (0.001)	3.3832	1.4395
	4.5 (0.005)	3.2885	1.6721
	2 (0.01)	3.2893	1.6874
Case 2	7 (0.001)	5.9294	1.1007
	4 (0.005)	5.9291	1.1019
	2.5 (0.01)	5.9089	1.1019

became unstable in a sense of rapidly changing WSS distributions as illustrated in Figure 6.8 blue circles. b) regarding a time step size of 0.001, the computation of each time step converged. While increasing the time step size for pulsatile simulation from 0.001 sec. to 0.005 sec. or 0.005 sec. to 0.01 sec., the number of non-converged time steps was also increasing. Consequently, the number of iterations per time step had to be increased in order to assure precise numerical simulation results. This led to increased time requirement for computation. However, the total time requirement for pulsatile simulations performed with 0.005 sec. or 0.01 sec. significantly decreased compared to the one with 0.001 sec. The detailed time requirements for each pulsatile simulation are given in Table 6.5.

6.4 Discussion

This study revealed that a certain threshold of mesh resolution was required to obtain converged blood flow velocities and WSS distributions. With a resolution lower than this threshold the velocity field and the WSS patterns fluctuated (see Table 6.3 and 6.4 gray areas and Figure 6.5, 6.6). These results comply with the work of [Prak 01, Lu 09] and [Domp 02] who stated that different mesh resolutions lead to different flow predictions and only mesh-independent flow solutions should be taken into account.

Once converged, WSS distributions obtained with either tetrahedral or polyhedral meshes were of similar appearance. Polyhedral meshes may therefore be considered as viable alternative to tetrahedral meshes:

1. Improved computational convergence as previously described by [Peri 04]. This becomes very important considering the clinical applicability of CFD-based hemodynamic simulations. Future clinical CFD-based diagnostic and treatment tools have to perform fast and stable. Varying simulation parameters for convergence optimization are not feasible during an intervention.

2. Polyhedral elements resolve significant WSS patterns with far less control elements in a more homogeneous manner than tetrahedral meshes. The reason

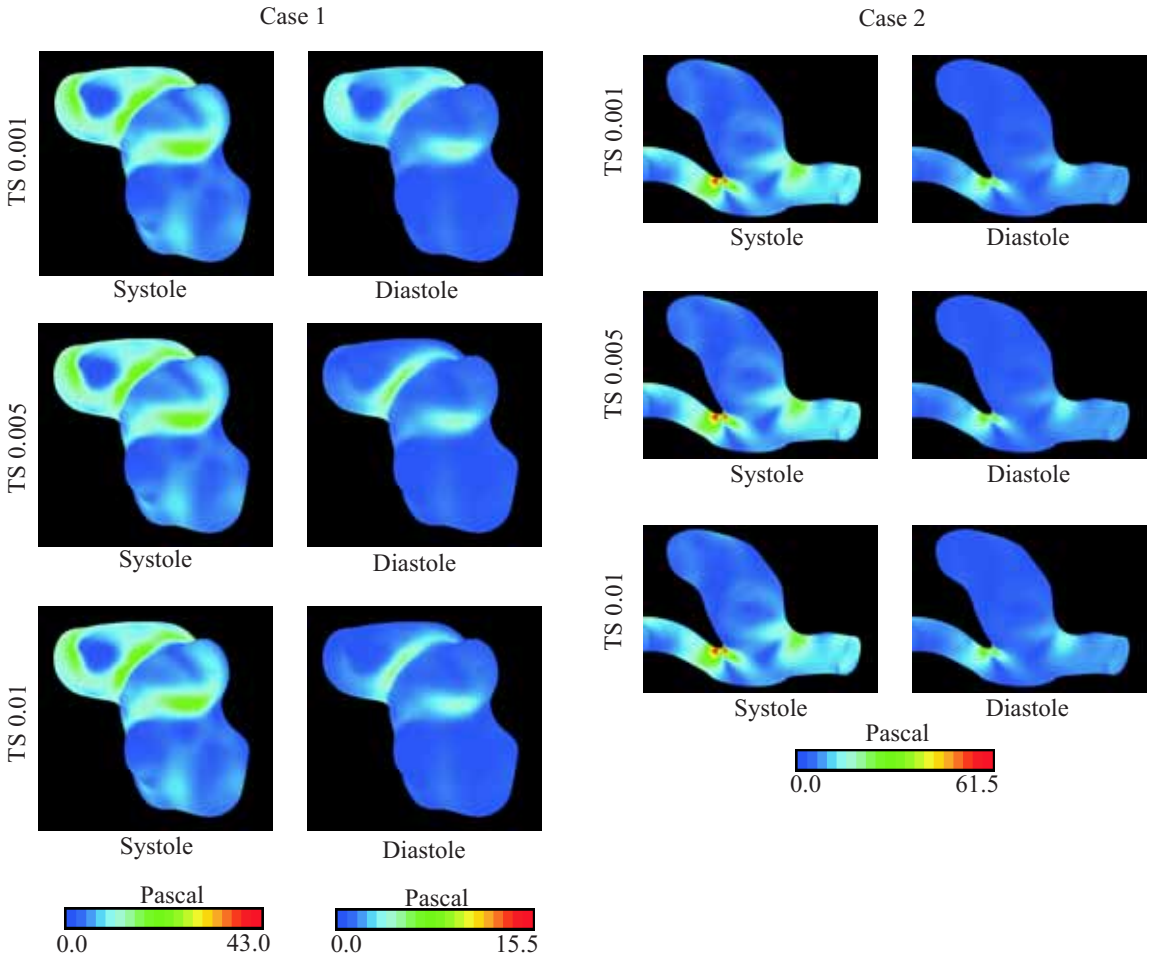

Figure 6.7: WSS distribution regarding pulsatile simulation performed with different time steps (TS). The images show results at systole and diastole. Overall, there are no significant differences between the WSS patterns obtained from simulations with time step 0.001 sec., 0.005 sec. or 0.01 sec.

for this lies in the way the WSS magnitude is calculated which depends on two major aspects: Firstly, only those cell elements are considered which actually share a face with the vessel boundary. Not all tetrahedral elements located at the vessel boundary share necessarily an entire face with the boundary - some may touch the boundary with its corner. While all polyhedral elements located at the wall share an entire face with the boundary itself. Secondly, the distances of the considered tetrahedral centers are not equal to the vessel wall leading to a more inhomogeneous WSS appearance.

Polyhedral meshes should be preferred over tetrahedral meshes in future standardized clinical simulations since they have shown superior CFD properties in terms of better convergence and less control elements which directly leads to a shorter computation time.

The usage of boundary layer leads to a more detailed appearance of WSS distributions. This occurs because the small prism elements approximating the vessel wall in denser and accurate manner. Accurately approximating WSS on the

aneurysm wall is of particular interest, as previous studies [Cebr 05b, Jou 08] have demonstrated that aneurysms exhibiting a WSS distribution with a higher portion of lower values were more prone to expansion and perhaps rupture. While boundary layers lead to more details in the WSS patterns, major features were already well resolved in meshes without boundary layers.

The drawback of boundary layer meshes consists in their setup resulting in an increased complexity in user interaction. Correct initialization of a boundary layer requires high smoothness and spatial resolution of the vessel surface mesh to avoid highly skewed elements at surface region exhibiting high curvature, e. g. vessel bifurcations. Extensive smoothing without close inspection by the user may lead to a deformation of the original vessel surface, i. e. shrinkness of the vessel diameter and more critical a shrinkness of the aneurysm neck potentially falsifying flow pattern and, thus, WSS distributions. Future clinical applications requiring an automated setup, boundary layer meshes may therefore be more difficult.

Another important aspect of our study is that the WSS distribution values vary even if the mesh size is considered fine enough to match the convergence criterion for our cases (see section 6.3.2). Since the true WSS distribution cannot be measured *in vivo* one has to be aware that the WSS distribution simulations have an intrinsic uncertainty. Within this study, this uncertainty for WSS values and velocities ranges between 0.84% to 6.3% comparing polyhedral vs. tetrahedral meshes with and without boundary layers. This uncertainty has to be taken into account clinically when making a quantitative statement concerning WSS, blood velocity or blood flow pattern. The key step in performing hemodynamic simulations therefore may be considered to generate a series of spatial varying meshes and to postulate convergence once variation of WSS falls in the range of 3% to 6%. If that is the case than the mesh maybe considered to be within a convergence area where mesh-independent simulation values can be computed. Given this evaluation, we propose to omit the usage of boundary layer for future clinical CFD application at least in the research phase. This will help to keep the mesh generation process simpler and easier automatable.

Pulsatile simulations according to a patient-specific cardiac cycle may lead to different WSS distributions as obtained by steady simulations. However, pulsatile simulations induce a much higher computational demand and thus lead to longer computation time making a clinical CFD application difficult during an intervention. The computation time can be minimized by either a reduction of the mesh resolution (which may lead to non-reliable results) or an increase of the computation time step governing the Fluent CFD solver for solving the Navier-Stokes equation. Our experiments have shown that an increase of the time step from 0.001 sec. to 0.01 sec. does not lead to any observable changes of the WSS distribution at systole time but a decrease of the computation time by a factor of six (case 1) and three (case 2) (see Table 6.5 column 2). An increase of the time step, however, has to be regarded with suspicion because there will be for sure a point once the time step is above a certain value which leads to unstable or even disconverging numerical solution. Overall, the first cardiac cycle should not be used for evaluation or diagnosis because of the transient response of the corresponding Navier-Stokes equations.

The results obtained during this study may be affected due to several limitation of the analysis. Our assumptions concerning the conducted CFD experiments differ from the *in vivo* state in terms of rigid vessel walls, Newtonian-based blood fluid and the determination of the boundary conditions. The outflows of the patient-specific models are defined as pressure outlet zero which does not have to match with the real environment. There might be natural resistances at the outflows. As with other computational studies, it is assumed that these limitations have only minor effects on the resulting flow pattern [Cebr 05a]. Future work, however, has to focus on the reduction of these limitations in the sense of validation against *in vivo* measurements, perform this analysis with much more cases and repeat it for the pulsatile simulation.

6.5 Conclusion

To the knowledge of the author, this chapter has presented the first mesh granularity and mesh independency analysis in the field of cerebral blood flow simulation of aneurysms. Here, the focus is on the influence of the CFD mesh as aneurysms represent a complex geometry. The aim was to determine how to reduce the computation time of the CFD simulation.

The results illustrate the importance of a well-founded mesh granularity evaluation leading to four major contributions:

1. A certain resolution is needed to obtain valid and stable WSS patterns and velocity values. However, even the CFD results of sufficient fine resolved meshes show an uncertainty of 3-6%.

2. Polyhedral meshes are preferred for cerebral aneurysm CFD simulations due to its advantages concerning better convergence, shorter computation time and high WSS accuracy.

3. The usage of a boundary layer revealed that it does not significantly change the accuracy of the WSS distributions especially when using polyhedral cell elements.

4. The variations of the time step for the pulsatile simulation experiments have illustrated that this leads to a reduction in time without losing significant WSS information at systole time.

Concerning the framework of this thesis, this study might serve as a first key step towards a future clinical CFD application where the mesh generation process has to be automated. Given the results of this chapter, the next chapter shows the effects of different patient-specific vessel segmentations on the hemodynamic simulation.

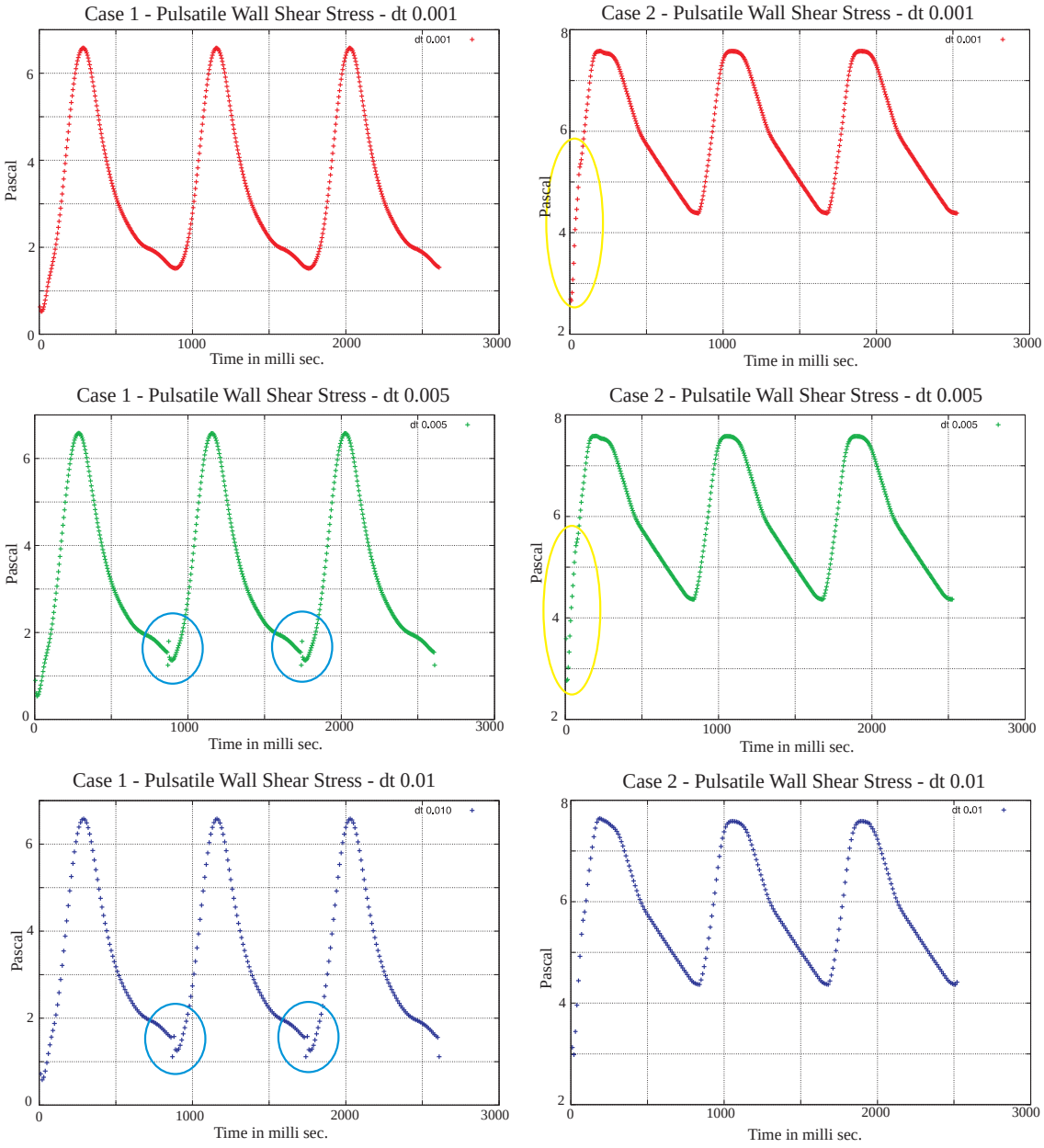

Figure 6.8: Area-Weighted-Average WSS distribution values of the pulsatile simulations plotted for the first three cardiac cycles. Left column shows the first case and right column the second case. While changing the time step, the transition between cardiac cycles becomes unstable as marked by the blue circles. The yellow circle indicates the transient response at the beginning of pulsatile simulations.

CHAPTER 7

Influence of Geometry Changes on Simulation

The last chapter of this thesis describes the impact of different patient-specific vessel geometries and their influence on hemodynamic simulations. Therefore, different vessel geometries are computed by three segmentation algorithms, i. e. region growing, pure 3-D driven ellipsoid (Chapter 5.3.1) and the novel 2-D driven 3-D ellipsoid vessel segmentation (Chapter 5.3.2). The knowledge concerning mesh independency of Chapter 6 is considered for all simulations performed within this chapter. Five patient datasets have been selected to evaluate the geometric effects regarding hemodynamic simulation. The results are twofold: (1) small vessel diameter changes at large vessel branches lead to minor effects in the hemodynamic simulation. (2) variations at bifurcation angles or small vessels imply major changes regarding flow pattern and volume as well as WSS distributions.

7.1 Motivation

Patient-specific cerebral vessel segmentation represents the base for performing hemodynamic simulations based on CFD. As already mentioned within the previous chapters, 3-D DSA volumes can be considered as the preferred image modality for CFD simulations due to its high spatial accuracy and contrastation such that even small vessel morphologies become visible. This accuracy, however, may be affected by factors like beam hardening, varying reconstruction kernels or the amount of injected contrast agent such that different vessel segmentation algorithms may come up with diverse vessel geometries. Considering the entire hemodynamic simulation pipeline (see Chapter 1.4) [Cebr 05a], various factors besides the geometry affect such simulations: starting from mesh element and surface approximations [Spie 11c] over patient-specific inflow waveforms [Karm 08] or blood modeling parameters like viscosity or density. If keeping all simulation parame-

ters fixed, the reproducibility of simulation results highly depends on the vessel segmentation and its subsequent geometric modeling.

As the literature shows, there have been some contributions which try to evaluate the influence of geometry variations. Hoi *et al.* [Hoi 04, Hoi 06] performed a study to validate CFD simulations on cerebral aneurysms using particle image velocimetry. The focus of his study was on the effects of small geometric variations. All experiments were based on a silicone phantom indicating alternations of the flow-field caused by geometric variations. Sun *et al.* [Sun 10a, Sun 10b] investigated the influence of input parameters together with meshing techniques on the flow patterns. An elastic cerebral aneurysm phantom model has been used to prove the reliability of CFD results under well controlled conditions.

Moreover, a reproducibility study has been conducted by Geers *et al.* [Geer 09, Geer 11] where patient-specific simulations were computed based on vessel models that were generated by 3-D DSA and CT-angiography (CTA). The experimental results revealed that small vessels (< 1 mm diameter) could not be reconstructed with CTA and the neck size of aneurysms appeared smaller in 3-D DSA than in CTA datasets. The difference in WSS distribution was large between the model from CTA and 3-D DSA, the main flow patterns, however, could be reproduced in both models. Venugopal *et al.* [Venu 06] used simple threshold segmentation techniques to extract two patient-specific aneurysms (ACoA and MCA) based on CTA datasets. The authors applied two intensity thresholds to create two vessel models per aneurysm and investigated the effects of geometric differences on the simulation result. The results revealed that the pressure distribution was similar whereas the WSS were different.

Although there are contributions in the literature concerning the influence of geometric changes on the hemodynamic simulation, so far the experiments are either phantom-based or the datasets are mainly generated by CTA. In this chapter, only 3-D DSA datasets are used with focus on the performance of three different vessel segmentation techniques to extract segmentation dependent patient-specific 3-D vessel geometries without showing vessel pathologies. These geometries are taken to evaluate the effects of geometry variations on the simulation results.

7.2 Methods

A subset of the evaluation patient datasets of Chapter 5.4 is taken in these experiments whose properties are again briefly summarized. The datasets were acquired with a Siemens C-arm system at the Department of Neuroradiology (University Hospital Erlangen, Germany) and contain different vessel types, e. g. ICA, MCA, ACA or PCoA. The spatial resolution ranges between $512\times512\times390$ and $512\times512\times511$ with an isotropic voxel spacing of 0.1 mm.

Three segmentation approaches are used to extract the vessel geometry from the datasets, i. e. three models are generated per dataset, to investigate the effects of different segmentations. These segmentation techniques can be distinguished in two ways:

1. 2-D or 3-D driven methods and

2. model-based versus intensity-related approach

The ellipsoid-based segmentation approach, detailed in Chapter 5.3.1, can be categorized as an entirely 3-D driven vessel segmentation method which makes use of tubular constraints to approximate the vessel branches. The 2-D driven 3-D technique (see Chapter 5.3.2) denotes a model-related hybrid segmentation methodology taking 2-D DSA information into account to adjust the vessel boundaries of the initial 3-D segmentation. To compare these automatic methods against a manual driven segmentation approach, region growing is applied where a medical expert decided on the selected intensity threshold based on his experience. Figure 7.1 shows an overview of the used vessel geometries and the deviations between the different segmentation results.

As already outlined in Chapter 6.2, the voxel-based vessel segmentations are converted into a triangle surface mesh using marching cubes algorithm, smoothed and saved in stereolithographic file format (STL). The STL file provides the input for the GAMBIT (ANSYS Inc.) [2] meshing toolkit to generate a volumetric mesh representation based on tetrahedral elements. The curvature size function of GAMBIT takes care of the triangle density such that areas of high curvature are approximated with a higher density of small triangles than those areas with less curvature. Given the evaluation results from Chapter 6.3 regarding polyhedral mesh elements, the Fluent simulation software (ANSYS Inc.) again is taken to convert the tetrahedral into polyhedral meshes. Table 7.2 summarizes the polyhedral mesh parameters, i. e. volume and number of cell elements. Due to different vessel segmentations, the volume size and number of cell elements vary in a range of less than 2%. This variation is small enough such that the effects on the simulation results can be negligible.

Blood is modeled as an incompressible, Newtonian fluid (density: 1050 kg/m^3; viscosity: 0.004 N/m^2 [Hass 04]) and the vessel walls are considered as rigid. Only steady-state simulations are performed with a constant inflow rate of 0.3 m/s and zero pressure outlet without using boundary layers as it is proposed in Chapter 6.2. Throughout all simulation experiments, simulation parameters are kept fixed to make the simulation results comparable regarding the geometric changes between different vessel models.

[2] www.ansys.com

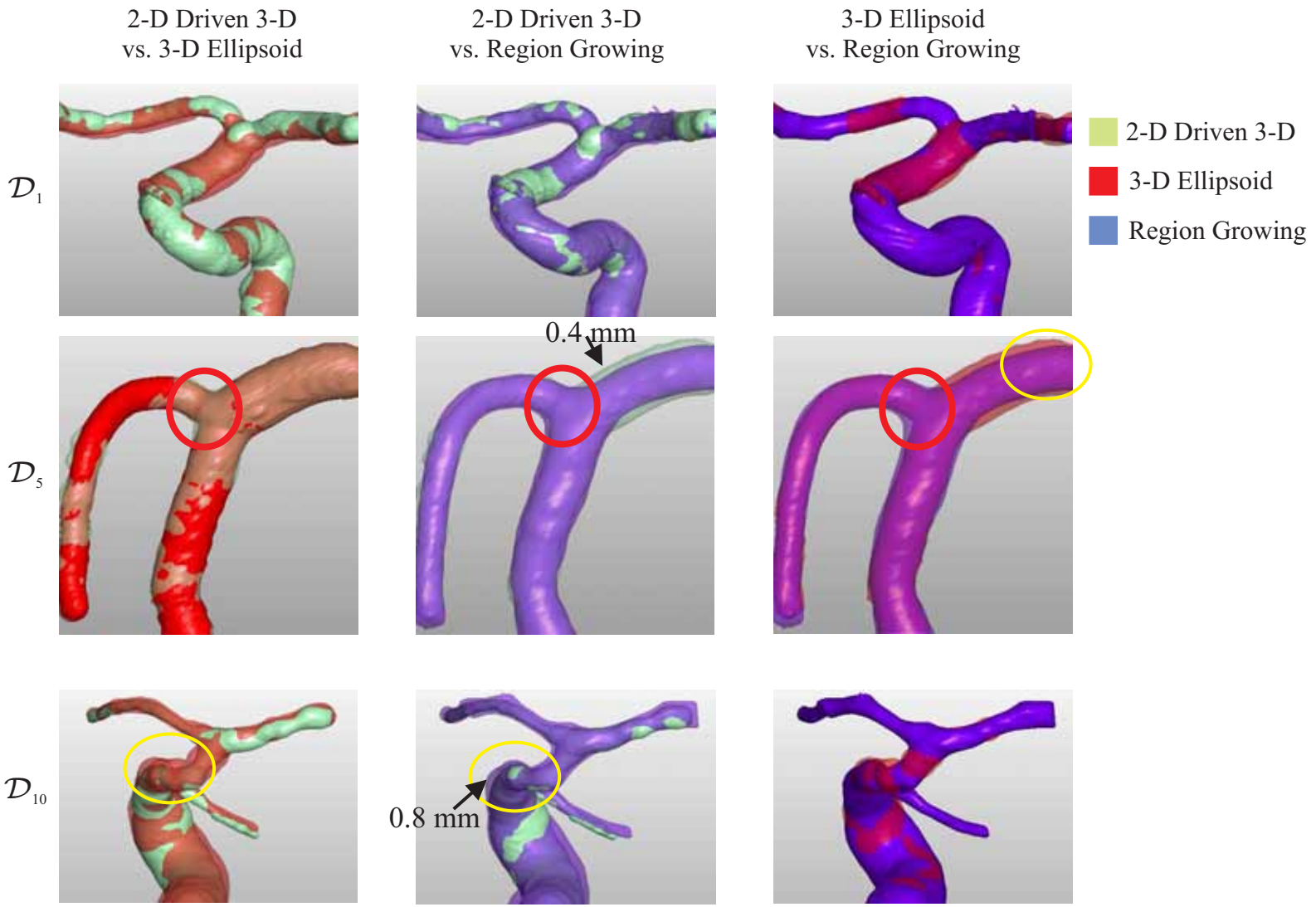

Figure 7.1: Overview of the differences between vessel geometries generated by three segmentation algorithms. The yellow circles indicate positions where the vessel diameter is modeled differently. The red circles highlight the deviation of the bifurcation angle between segmentations.

Table 7.1: Quantitative evaluation results concerning mass flow rates and outflow vessel diameter area concerning three different segmentation methods, i. e. region growing (Re.Gr.), 3-D ellipsoid (3-D E.) and 2-D driven 3-D segmentation (2-D/3-D).

Data	Seg.	Inflow	Out1				Out2				Out3				Out4			
			Mass flow		Area		Mass flow		Area		Mass flow		Area		Mass flow		Area	
		[g/s]	[g/s]	[%]	[mm^2]	[%]	[g/s]	[%]	[mm^2]	[%]	[g/s]	[%]	[mm^2]	[%]	[g/s]	[%]	[mm^2]	[%]
	Re.Gr.	4.9	1.3	27.3	4.0	45.7	0.4	8.0	0.55	6.3	3.2	64.7	4.2	48.1				
$\mathcal{D}_1$	3-D E.	3.7	1.1	30.0	3.0	39.3	0.4	10.7	0.56	7.5	2.2	59.3	4.0	53.3				
	2-D/3-D	4.0	1.1	26.8	2.7	34.8	0.5	12.1	0.63	8.1	2.4	61.1	4.4	57.1				
	Re.Gr.	4.3	0.7	3.8	3.1	23.2	0.9	19.8	0.56	4.2	2.7	61.5	6.9	50.4	0.6	14.9	3.0	22.3
$\mathcal{D}_2$	3-D E.	3.6	0.2	5.9	2.4	16.4	0.5	14.4	0.62	4.2	2.7	74.2	8.8	59.8	0.2	5.4	2.9	19.6
	2-D/3-D	2.9	0.2	7.7	2.0	18.6	0.6	20.0	0.56	5.2	1.9	67.0	5.8	54.3	0.1	5.3	2.3	21.8
	Re.Gr.	4.0	0.2	4.5	0.5	9.1	3.8	95.5	5.01	90.9								
$\mathcal{D}_3$	3-D E.	4.1	0.3	8.3	1.1	13.3	3.8	91.7	7.05	86.7								
	2-D/3-D	3.7	0.4	11.4	1.0	19.6	3.7	88.6	4.15	80.4								
	Re.Gr.	3.5	0.5	13.3	0.6	9.6	0.6	16.6	1.6	25.6	2.4	70.1	4.1	64.8				
$\mathcal{D}_5$	3-D E.	2.9	0.6	20.5	1.0	11.3	0.2	6.3	1.8	20.5	2.2	73.3	5.9	68.2				
	2-D/3-D	3.1	0.6	20.8	1.0	11.2	0.2	5.6	1.7	19.7	2.3	73.7	5.9	69.2				
	Re.Gr.	5.8	1.3	22.2	1.0	16.8	0.9	15.2	1.5	24.4	3.6	62.5	3.5	58.8				
$\mathcal{D}_{10}$	3-D E.	4.7	0.7	15.4	0.5	13.8	0.9	18.7	1.0	26.3	3.1	65.9	2.2	59.9				
	2-D/3-D	4.3	0.9	20.7	0.6	17.2	0.3	6.7	1.1	30.6	3.1	72.6	1.8	52.2				

Table 7.2: Three different segmentation algorithms delivered three vessel geometries per dataset, i. e. 2-D driven 3-D, 3-D ellipsoid and region growing. This table gives an overview about the properties of the computed vessel models.

	2-D driven 3-D		3-D Ellipsoid		Region Growing	
	Volume [mm^3]	# Cells	Volume [mm^3]	# Cells	Volume [mm^3]	# Cells
$\mathcal{D}_1$	512	79,780	531	82,564	586	98,090
$\mathcal{D}_2$	510	78,709	521	80,701	669	85,701
$\mathcal{D}_3$	495	75,505	617	83,170	571	88,119
$\mathcal{D}_5$	383	89,952	377	88,589	451	84,994
$\mathcal{D}_{10}$	477	85,161	568	87,657	642	88,314

7.3 Results

As illustrated in Figure 7.1, different segmentation approaches lead to different vessel geometries. Comparing vessel diameters (yellow circle in Figure 7.1), pure 3-D driven segmentation methods like region growing or 3-D ellipsoid show up with thicker vessel diameters as 2-D driven 3-D segmentation. Vessel diameters vary up to 0.8 mm which corresponds to eight voxels. Concerning CFD simulations, the most serious difference between these methods appear at vessel bifurcations. The reason for this difference is due to different segmentation algorithms. Model-based segmentation methods like interleaved 3-D ellipsoid (Chapter 5.3.1) are characterized by tubular constraints modeling vessel branching points more perpendicular w. r. t. its mother vessel than pure intensity driven methods. The red circles in Figure 7.1 demonstrate the difference concerning the vessel bifurcation modeling. All quantitative simulation results are summarized in Table 7.1.

Yellow circles in Figure 7.2 indicate the different modeling aspects regarding vessel bifurcations resulting in completely different flow patterns encoded as velocity pathlines and WSS distribution. The number of velocity pathlines shown in Figure 7.2 is related to the mass flow rate, i. e. more pathlines indicate a higher mass flow rate. Considering the pathlines of dataset $\mathcal{D}_5$ in Figure 7.2, the inflow jet coming from the bottom splits up into two major jets for the region growing vessel model because of the location and position of the vessel branching to the left. The 3-D ellipsoid and the 2-D driven 3-D model do not show such a split because the location of the bifurcation point is segmented more parallel to the jet stream which let the blood flow pass by. This change of the bifurcation angle leads to a mass flow drop of about 10% concerning Out2 and an increase of the mass flow rate of 7% at Out1 between region growing and model-based vessel geometries (see Table 7.1 $\mathcal{D}_5$ Out1 and Out2).

Not only different bifurcation angles may imply changes to the flow pattern but also local deviations of vessel diameters. $\mathcal{D}_{10}$ in Figure 7.2 shows differences regarding vessel diameters and bifurcation angles indicated by red circles. The 2-D driven 3-D vessel geometry exhibits a smaller vessel diameter as the other two

geometries because of the additional 2-D vessel information inducing this vessel diameter reduction especially concerning outflow (Out2). This causes a change in the mass outflow rate of 12% w. r. t. Out2 (Table 7.1, $\mathcal{D}_{10}$, Out2) comparing region growing and 3-D ellipsoid segmentation with the 2-D driven 3-D method. Dependent on the location and degree of geometry changes, the primary WSS distributions may be similar between different vessel geometries as depicted in Figure 7.2 ($\mathcal{D}_5$). However, if the geometric changes are essential, the WSS and the flow patterns feature huge differences, e. g. $\mathcal{D}_{10}$ (see orange circles in Figure 7.2).

7.4 Discussion

Overall, it can be stated that vessel segmentation denotes the key for valid patient-specific CFD-based hemodynamic simulations. As indicated by [Venu 06], different vessel segmentations result in varying vessel geometries leading to major differences in the simulation result. Hence, vessel segmentation has to be performed very carefully because small local geometric deviations may induce huge changes in the local flow pattern. The main focus of this work has been on evaluating the geometric deviations which originate from different vessel segmentation approaches.

Model-based segmentation methods like interleaved 3-D ellipsoids are characterized by tubular constraints. This can be considered, on the one hand, as an advantage within the clinical hemodynamic workflow (refer to Chapter 1.4) because the segmentation result yields a smooth surface without showing peak artifacts or highly skewed triangles. This heavily minimizes the efforts and required time during the mesh generation step. Moreover, smooth surface meshes denote a key requirement for CFD solvers such that the computation process converges fast. On the other hand, this 3-D ellipsoid segmentation method may miss small geometric vessel aspects due to its tubular regularization which may have an impact on the simulation result.

In particular, the bifurcation plane which defines the vessel branching point is modeled differently comparing the different vessel geometries. Such kind of differences may lead to totally different splits of the inflow jet which explain the increase or decrease concerning the mass flow rates at the corresponding outlets of the geometries. Also, the WSS distribution is affected by the geometric variations as shown in Figure 7.2. The 3-D DSA reconstruction overestimates vessel diameters which has been discussed in Chapter 5 in detail. Hence, the 2-D driven 3-D based vessel geometries locally exhibit smaller vessel diameters compared to the pure 3-D data driven methods. This implies different WSS distributions and flow pattern. Especially if considering vessel branches with very small diameters, a further reduction of the vessel diameter can have a dramatic drop of the mass flow rate as depicted in Table 7.1 ($\mathcal{D}_5$ out2).

7.5 Conclusion

The impact of different patient-specific vessel geometries on the hemodynamic simulation result has been investigated within the study of this chapter. Two conclusions can be drawn from the experiments:

1. The 3-D ellipsoid-based segmentation algorithm models vessel bifurcations more different than intensity related segmentations which leads to different mass flow rates and flow patterns.

2. Variation of vessel diameters also have an impact on the mass flow rate as well as on the WSS distribution.

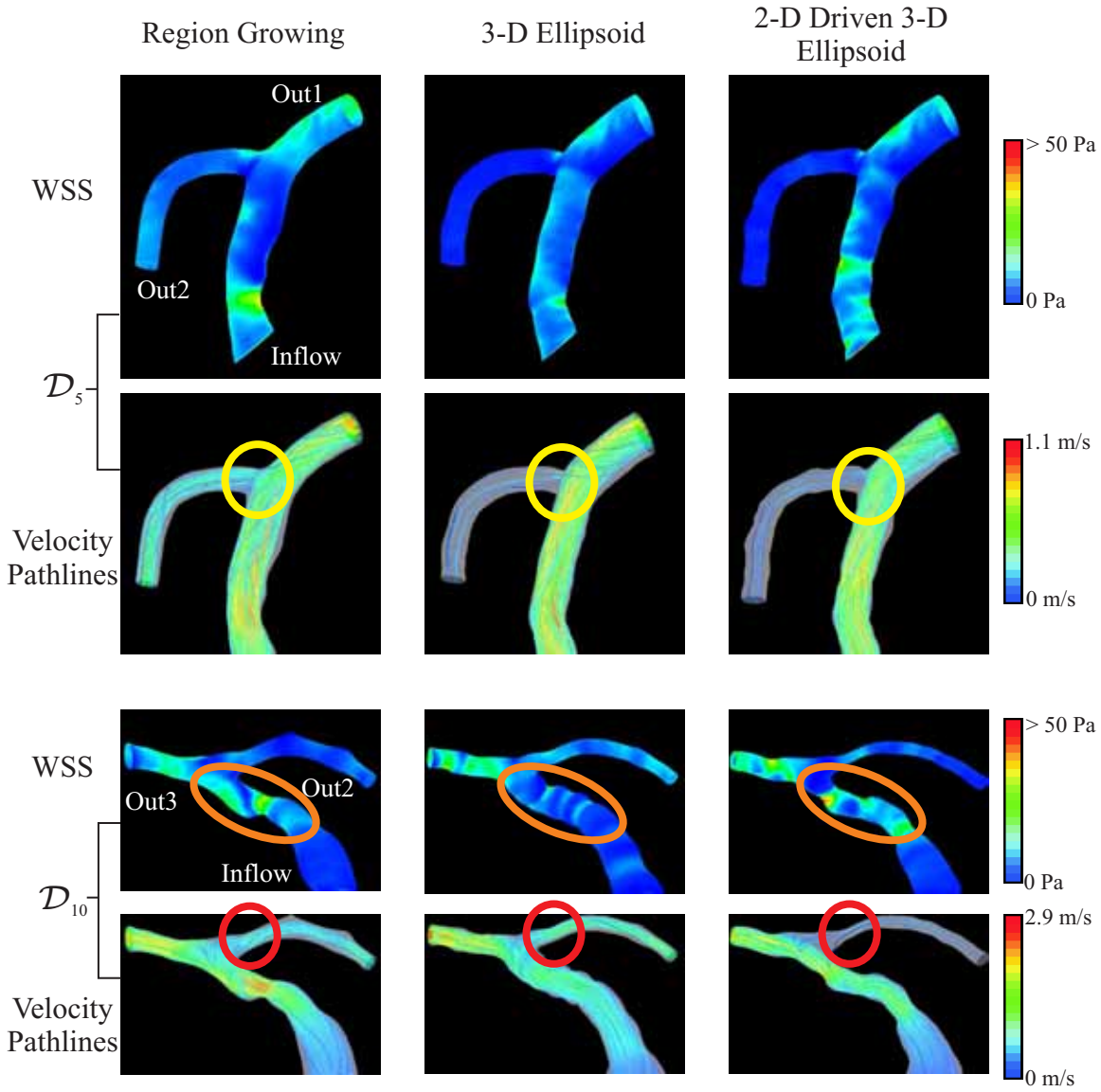

Figure 7.2: Simulation results based on vessel geometries created by three different segmentation results. The yellow circles indicate the different bifurcation modeling resulting in a change of the split of the inflow jet, i. e. more pathlines denote larger mass flow. The red circles illustrate the effect of local vessel diameter deviations and its consequences regarding the flow pattern and mass flow rate. The orange circles depict the variation of the WSS distribution between different vessel geometries.

Part IV

Outlook and Summary

CHAPTER 8

Outlook

Within this thesis, different components have been developed providing a major step to perform 2-D and 3-D vessel segmentation on DSA data together. An algorithmic framework has been presented to combine 2-D vessel information with 3-D segmentation. This enables to automatically perform 3-D vessel segmentation enhanced and driven by 2-D vessel segmentation. Further scientific work might improve the efficiency and robustness of the 2-D driven 3-D segmentation approach. One step improving the computational efficiency of the 2-D/3-D segmentation method denotes the avoidance of computing the forward projection for each parameter optimization step. Since the forward projection makes use of rays, the intersection points between these rays and the ellipsoid-based segmentation can be analytically computed. The computation of the intersection point yields a quadratic equation which can be efficiently done on the GPU. Hence, the entire ellipsoid parameter optimization can be transferred onto the GPU such that read and write operations between the CPU and GPU can be heavily reduced. This speedup will make the proposed 2-D/3-D segmentation framework more attractive to be applied in a clinical prototype.

Further evaluation studies may shed light on how many 2-D projections are required to get optimal results in terms of time and quality. Therefore, a varying number of projections with different projection angles have to be evaluated to gain information about the effect on the 3-D vessel segmentation result and the required computation time. Since the 2-D projection images were chosen w. r. t. different projection angles, the vessel movement may not be coherent regarding the cardiac phase. The robustness of the 2-D driven 3-D vessel segmentation may be increased by incorporating ECG-gated 2-D DSA projections such that the projections chosen for 3-D adaptation show the vessels at the same cardiac phase. This will limit the influence of vessel movement during the 2-D/3-D optimization as much as possible.

Considering the hemodynamic workflow (see Chapter 1.4), this thesis investigated the first two steps, i. e. vessel segmentation and mesh generation and its influence on the hemodnamic simulation result. The presented evaluations have built a base to perform further research w. r. t. the next two steps of the hemodynamic workflow, i. e. simulation parameters and fluid structure interaction. One important aspect to utilize blood flow simulation results for diagnostic purposes is the acquisition of patient-specific simulation parameters in vivo, e. g. blood pressure or velocity. For example, a pressure catheter or Doppler ultrasound device may be applied at the neck area to gain such information. Or since a catheter has been used in every endovascular intervention, a much less cost-intensive alter-

native may be the direct usage of the catheter as pressure sensor like it is done for a drip. The combination of patient-specific and in-vivo acquired simulation parameters will make blood flow simulations much more reliable. Furthermore, the incorporation of additional flow information like high speed DSA acquisitions (>30 frame/sec.) or MRI velocity fields may enrich CFD-based simulations. High speed DSA series show the blending of contrast agent with blood and its flow pattern in a very detailed manner. The temporal resolution of such series is also very high. Moreover, MRI acquired velocity fields may also be used as validation base for CFD simulations. Prospective CFD solver may fuse MRI or high speed DSA-related flow information as supporting points or as validation base to make hemodynamic simulation results more acceptable for diagnose purposes in the future.

CHAPTER 9

Summary

Within the last decade, more and more cerebrovascular pathologies have been treated by catheter-guided minimal invasive interventions. In angio suites, this kind of treatment has become possible because of the availability of modern C-arm systems providing X-ray based 2-D and 3-D DSA data during an intervention. Even small cerebral vessels become visible due to its high contrastation and spatial resolution which emphasizes the high diagnostic value. Thus, 3-D DSA represents a major step in diagnosis and treatment planning for endovascular interventions in the field of neuroradiology. The thesis makes use of this data and focuses on vessel segmentation in 2-D and 3-D. At first glance, this task seems to be straightforward. Accurate 3-D vessel segmentation, however, is challenging due to the uncertainty of the exact vessel boundary position in 3-D DSA data. The determination of the vessel boundary may be corrupted by beam hardening, the hemodynamic mixture of the contrast agent or reconstruction kernels. Particularly with regard to the performance of patient-specific hemodynamic simulations, small changes within the vessel segmentation may induce variations on flow, pressure or WSS pattern. Since 2-D DSA projections clearly show the vessel boundary position, it is of benefit to integrate this information into the 3-D vessel segmentation process. Therefore, a novel framework seamlessly combining 2-D and 3-D vessel segmentation algorithms is presented in this thesis to compute vessel geometries of highest accuracy which meet the input requirements of CFD simulation software to perform hemodynamic simulations.

2-D DSA series are heavily used for diagnosis and treatment planning of cerebrovascular diseases, e. g. stenosis or aneurysms. Depending on the amount of injected contrast agent and the duration of injection, these DSA series may not exhibit one single DSA image showing the entire vessel tree. Typically, such a DSA series can be split up into three phases due to the contrast agent flow, i. e. mask, arterial and parenchymal phase. The interesting vessel information regarding our post-processing algorithms (see Chapter 3 and 5) is depicted within the arterial phase showing medium and large vessels. Therefore, a novel classification-based summation algorithm is delineated in Chapter 2 which automatically categorizes the images of the series within the aforementioned phases. All images corresponding to the arterial phase are put together into one *final image* by either image summation or taking the minimum intensities. The phase classification is done by a two-step approach. The mask/arterial phase border is determined by classification methods (Perceptron, SVM etc.) being trained from a set of DSA series. The arterial/parenchymal phase border is specified by a simple but effective threshold-based method. The evaluation of the proposed method is two-sided: (1) compar-

ison between automatic and medical expert-based phase selection using different classifiers and (2) the quality of the *final image* is measured by gradient magnitudes inside the vessels and SNR outside. Experimental results, which were performed on 14 DSA series, show a match between expert and automatic phase separation of 93% and 50%. The *final images* exhibit a mean SNR increase of up to 182% compared to summing up the entire series.

The *final images* and the 2-D DSA projections given from the 3-D reconstruction denote the input of the 2-D vessel segmentation method which is described in Chapter 3. Inhomogeneous contrast agent distributions within the vessels, patient movement as well as smooth intensity ramps at the vessel boundary do not allow performing straightforward global threshold-based vessel segmentation. Hence, a new semi-automatic 2-D vessel segmentation method is proposed working with local adaptive contrast enhancement to eliminate intensity inhomogeneity within the vessel region. Since this method is designed to work within the 2-D/3-D vessel segmentation framework, there are two initialization modes for this algorithm: either manually selected seed points or a forward projected 3-D centerline define the vessel branches to be segmented. If the segmentation algorithm has been initialized by manual seed points, a 2-D vessel centerline is computed using Dijkstra's algorithm which connects these seed points. The local contrast enhancement is done within boxes which are aligned perpendicular along the centerline. The eigenvectors of the Hessian matrix, computed at each centerline point, are utilized for proper alignment. The intensities are enhanced for each box using the sigmoid function which is controlled by the local box mean value. The evaluation database comprises 45 different DSA images where a mean Hausdorff distance of 23 pixels and a sensitivity of 89% could be achieved.

The 2-D vessel segmentation results can now be incorporated as ground truth information into the 3-D vessel segmentation approach. The 3-D centerline computation represents the initialization step for the subsequent 3-D vessel segmentation. This 3-D centerline technique has to overcome similar challenges as for the 2-D vessel segmentation, e. g. inhomogeneous contrast agent distributions, beam hardening, elliptically shaped vessels occurring due to vessel movement especially for coronary arteries, multi-scale vessel diameters or touching vessel structures. This partially leads to an uncertainty about the actual centerline path. To properly handle all this, a graph-based centerline method has been proposed in Chapter 4 which is based on a multi-scale MM cost function. The major contribution represents a distance map regularization of the MM cost function such that the centerline path remains at the actual vessel center axis even for corrupted vessel regions. Therefore, the distance map is computed by a newly developed local adaptive statistical thresholding scheme separating the three a priori known intensity classes (background, artifacts and vessel structure) of a 3-DRA volume. The centerline algorithm has shown to be powerful within a clinical setup and is extensively evaluated on 15 cerebral and 13 motion-compensated coronary 3-DRA datasets. The quantitative evaluation shows a mean distance of 0.42 mm against a pure MM driven centerline approach.

Re-considering the 2-D/3-D vessel segmentation framework, the 3-D centerline component provides an initialization for the 2-D as well as for the 3-D ellipsoid-

based vessel segmentation approach which is outlined in Chapter 5. This chapter represents the key contribution of this thesis because a novel 2-D driven 3-D vessel segmentation algorithm is proposed which can also be considered as a validation technique for other 3-D vessel segmentation methods working on 3-DRA data. The 2-D DSA images are considered as gold standard regarding quantitative vessel measurements during diagnosis or therapy planning of cerebrovascular diseases. The interleaved ellipsoids are aligned and initialized utilizing the centerline. The parameters of all ellipsoids are optimized by an energy function comprising an external and internal energy term. The internal energy term takes care about the smoothness of the entire vessel model and the external energy term guides the parameters such that the ellipsoids deform towards the local vessel boundary. The parameter optimization is done by gradient descent. To assess the accuracy of the converged 3-D vessel segmentation, its forward projections from different viewing angles are iteratively overlaid with the corresponding 2-D DSA projections. Now, the local adaptivity of the proposed 3-D segmentation approach pays off because local vessel discrepancies between the forward projection of the 3-D segmentation and the 2-D vessel data can be adjusted by back-projection into 3-D and changing the parameters of the corresponding ellipsoids. This parameter adjustment is formalized as a global objective function steering the 2-D/3-D optimization. Our methodology has been evaluated on phantom and ten patient datasets. Three 2-D DSA projections from varying viewing angles have been used for optimization. Superior results could be achieved against state-of-the-art segmentations like region growing, i. e. a mean improvement of 7.2% in precision and 5.8% for the Dice coefficient.

In respect to the hemodynamic workflow, Chapter 2 to 5 only deal with the vessel segmentation step. In Chapter 6, the proximate mesh generation step is analyzed w. r. t. the effect of different volume element types, mesh sizes and mesh compositions on the CFD simulation result (flow velocity and WSS). Therefore, two vessel geometry models have been selected to perform a mesh independence analysis by creating a set of varying mesh size configurations based on tetrahedral and polyhedral volume element types. Throughout this study, only the surface and volume mesh approximation of the vessel geometry have varied spatially - not the vessel geometry itself. Three conclusions can be drawn from the simulation results based on Fluent software (ANSYS Inc.): (1) with increasing mesh size, the flow velocity and the WSS distribution converge towards stable values with a variation of up to 6.3%. (2) polyhedral mesh types are beneficial concerning convergence speed and more homogeneous WSS pattern. (3) the comparison of WSS patterns between meshes with and without boundary layers yields that the difference has become more and more negligible with increasing mesh size. Without considering vessel geometry related issue, it can be stated that different mesh configurations induce an uncertainty of up to 6% on the hemodynamic simulation result.

In opposition to the study described in Chapter 6, Chapter 7 concludes this thesis with a CFD study which investigates the impact of having the same patient dataset but different vessel segmentation methods applied yielding slightly different vessel geometries. Hence, in this study the vessel geometry does change -

not the surface or volume mesh approximation. Per patient dataset, three different vessel segmentation algorithms have been applied which are: region growing, pure 3-D ellipsoid-based and the 2-D driven 3-D vessel segmentation approach. The results regarding mesh generation of Chapter 6 have been considered throughout this study, i. e. the number of volume elements of the vessel geometries being compared to each other varies less than 2%. Major differences between the different vessel geometries are found concerning the vessel diameters and the modeling of branching vessels. Particularly, variations of the bifurcation angle at the vessel branching point lead to major changes of the mass flow or flow pattern because of the different split of the inflow jet. The 2-D driven 3-D based vessel geometries tend to show smaller vessel diameters due to the adaptation towards 2-D vessel information. Local decrease of the vessel diameter may develop a bottle neck area leading to a significant change in the flow distribution as well.

In conclusion, this thesis proposed a new vessel segmentation framework combining 2-D and 3-D DSA vessel data for validation and adaptation purposes. The CFD evaluation studies concerning mesh generation and vessel geometry changes revealed that vessel segmentation and its corresponding mesh approximation denote a very crucial part within the hemodynamic workflow. As requested, the algorithms have been implemented on a clinical prototyping platform to be successfully applied within a clinical environment.

List of Symbols

$\mathcal{K}$	DSA series showing the contrast agent flow through vessels	18
$\mathcal{K}_{\text{F,SUM}}$	Final SUM image of DSA series	26
$\mathcal{K}_{\text{F,MIN}}$	Final MIN image of DSA series	26
L	Frame index - lower boundary of the arterial phase	20
U	Frame index - upper boundary of the arterial phase	20
Ω	Image region	21
v	Provides access to a pixel intensity value	20
$\boldsymbol{u}$	Pixel coordinates $\in \mathbb{R}^2$	20
μ	Mean intensity value	21
γ	Skewness of histogram	21
ψ	Hessian matrix based vesselness measure	21
$\boldsymbol{w}$	Feature vector DSA summation	23
λ	Eigenvalue of the Hessian matrix	22
$\boldsymbol{e}$	Eigenvector of the Hessian matrix	24
Λ	Set of features containing all features for DSA summation	23
ω	Class label	24
g	Linear discriminant function	24
Y	Set of missclassified features	24
$\mathcal{B}$	Background region	27
ζ	Evaluation measure - sum of gradient magnitudes	27
σ	Standard deviation	27
$\boldsymbol{n}$	Normal vector $\in \mathbb{R}^3$	24
H	Plane	24
d	Distance to origin of coordinate system $\in \mathbb{R}$	24
D	Perceptron criterion function	24
$\boldsymbol{c}$	Centerline point $\in \mathbb{R}^2$	36
$\boldsymbol{C}$	Set of centerline points	36
l	Box length $\in \mathbb{R}$	36
ξ	Vessel diameter $\in \mathbb{R}$	37
S	Sigmoid function	38
$\boldsymbol{o}$	Origin of a coordinate system	38
$\boldsymbol{P}_{\text{Gold}}$	Ground truth segmentation	41
$\boldsymbol{P}_{\text{Seg}}$	Segmentation result	41
d_{H}	Hausdorff distance $\in \mathbb{R}$ - evaluation measurement	41
d_{SE}	Sensitivity value $\in \mathbb{R}$ - evaluation measurement	42
$\boldsymbol{b}$	Center position $\in \mathbb{R}^3$ of a box	54
$\boldsymbol{V}$	Set of voxels defining the local box neighborhood	54
f	Provides access to a voxel intensity value	54
p	Probability density function	54
Θ	Box parameter vector $\in \mathbb{R}^3$	54

List of Figures

List of Tables

Bibliography

[Atla 09] S. Atlas. *Magnetic Resonance Imaging of the Brain and Spine*. Vol. 2, Lippincott Williams and Wilkins, 4 Ed., 2009.

[Aust 75] W. Austen, J. Edwards, R. Frye, G. Gensini, V. Gott, L. Griffith, D. McGoon, M. Murphy, and B. Roe. "A reporting system on patients evaluated for coronary artery disease. Report of the Ad Hoc Committee for Grading of Coronary Artery Disease, Council on Cardiovascular Surgery, American Heart Association". *Circulation*, Vol. 51, No. 4, pp. 5–40, April 1975.

[Aylw 02] S. Aylward and E. Eberly. "Initialization, noise, singularities, and scale in height-ridge traversal for tubular object centerline extraction". *IEEE Transactions on Medical Imaging*, Vol. 21, No. 2, pp. 61–75, February 2002.

[Baer 03] S. Baert, M. Viergever, and W. Niessen. "Guide-wire tracking during endovascular interventions". *IEEE Transactions on Medical Imaging*, Vol. 22, No. 8, pp. 965–972, August 2003.

[Bent 02] Y. Bentoutou, N. Taleb, M. C. E. Mezouar, M. Taleb, and L. Jetto. "An invariant approach for image registration in digital subtraction angiography". *Pattern Recognition*, Vol. 35, No. 12, pp. 2853–2865, December 2002.

[Boua 07] S. Bouattour and D. Paulus. "Vessel Enhancement in 2D Angiographic Images". In: F. Sachse and G. Seemann, Eds., *Lecture Notes in Computer Science, FIMH*, pp. 41–49, 2007.

[Bres 65] J. Bresenham. "Algorithm for computer control of a digital plotter". *IBM Systems Journal*, Vol. 4, No. 1, pp. 25–30, January 1965.

[Brin 09] W. Brinjikji, H. Cloft, G. Lanzino, and D. Kallmes. "Comparison of 2D Digital Subtraction Angiography and 3D Rotational Angiography in the Evaluation of Dome-to-Neck Ratio". *American Journal of Neuroradiology*, Vol. 30, pp. 831–834, April 2009.

[Brod 82] W. Brody. "Digital subtraction angiography". *American Journal of Neuroradiology*, Vol. 29, No. 3, pp. 1176–1180, November 1982.

[Brun 05] T. Brunner. *Cone-beam CT with C-arm systems In: Imaging Systems for Medical Diagnostic: Fundamentals, technical solutions and applications for systems applying ionization radiation, nuclear magnetic resonance and ultrasound*. Publicis Corporate Publishing, 2005.

[Buzu 02] T. M. Buzug. *Einführung in die Computertomographie: Mathematisch-physikalische Grundlagen der Bildrekonstruktion*. Springer-Verlag, 2002.

[Buzu 08] T. M. Buzug. *Computed Tomography - From Photon Statistics to Modern Cone-Beam CT*. Springer-Verlag, 2008.

[Cast 06] M. Castro, C. Putman, and J. Cebral. "Patient-Specific Computational Fluid Dynamics Modeling of Anterior Communicating Artery Aneurysms A Study of the Sensitivity of Intra-Aneurysmal Flow Patterns to Flow Conditions in the Carotid Arteries". *American Journal of Neuroradiology*, Vol. 27, No. 10, pp. 2061–2068, December 2006.

[Cebr 05a] J. Cebral, M. Castro, S. Appanaboyina, C. Putman, D. Millan, and A. Frangi. "Efficient pipeline for image-based patient-specific analysis of cerebral aneurysm hemodynamics: technique and sensitivity". *IEEE Transactions on Medical Imaging*, Vol. 24, No. 4, pp. 457–467, April 2005.

[Cebr 05b] J. Cebral, M. Castro, J. Burgess, R. Pergolizzi, M. Sheridan, and C. Putman. "Characterization of cerebral aneurysms for assessing risk of rupture by using patient-specific computational hemodynamics models". *American Journal of Neuroradiology*, Vol. 26, pp. 2550–2559, November 2005.

[Cebr 05c] J. Cebral and R. Lohner. "Efficient simulation of blood flow past complex endovascular devices using an adaptive embedding technique". *IEEE Transactions on Medical Imaging*, Vol. 24, No. 4, pp. 468–476, April 2005.

[Chan 04] H. Chan, A. Chung, S. Yu, and W. Wells. "2D-3D vascular registration between digital subtraction angiographic (DSA) and magnetic resonance angiographic (MRA) images". In: *IEEE International Symposium on Biomedical Imaging: Nano to Macro*, pp. 708–711, April 2004.

[Chan 09] H. Chang, G. Duckwiler, D. Valentino, and W. Chu. "Computer-assisted extraction of intracranial aneurysms on 3D rotational angiograms for computational fluid dynamics modeling". *Medical Physics*, Vol. 36, No. 12, pp. 5612–5621, December 2009.

[Cheo 03] L. Cheong, T. Koh, and Z. Hou. "An automatic approach for estimating bolus arrival time in dynamic contrast MRI using piecewise continuous regression models". *Physics in Medicine and Biology*, Vol. 48, No. 5, p. N83, 2003.

[Coop 07] F. Cooperation. *Gambit 2.4 User's Guide*. E.I. du Pont de Nemours and Co., 2007.

[Demp 77] A. P. Dempster, N. M. Laird, and D. B. Rubin. "Maximum likelihood from incomplete data via the EM algorithm". *Journal of the Royal Statistical Society, Series B*, Vol. 39, No. 1, pp. 1–38, 1977.

[Desc 01] T. Deschamps and L. Cohen. "Fast extraction of minimal paths in 3D images and applications to virtual endoscopy". *Medical Image Analysis*, Vol. 5, No. 4, pp. 281–299, December 2001.

[Dijk 59] E. W. Dijkstra. "A note on two problems in connexion with graphs". *Numerische Mathematik*, Vol. 1, pp. 269–271, 1959.

[Doer 06] A. Doerfler, I. Wanke, S. Goericke, H. Wiedemayer, T. Engelhorn, E. Gizewski, D. Stolke, and M. Forsting. "Endovascular Treatment of Middle Cerebral Artery Aneurysms with Electrolytically Detachable Coils". *American*, Vol. 27, No. 3, pp. 513–520, March 2006.

[Domp 02] J. Dompierre, M.-G. Vallet, Y. Bourgault, M. Fortin, and W. G. Habashi. "Anisotropic mesh adaptation towards user-independent mesh-independent and solver-independent CFD Part3 Unstructured meshes". *International Journal for Numerical Methods in Fluids*, Vol. 39, pp. 675–702, 2002.

[Duda 01] R. Duda, P. Hart, and D. Stork. *Pattern Classfication*. John Wiley and Sons, second edition Ed., 2001.

[Fitz 82] D. Fitzgerald, A. O'Shaughnessy, and V. Keavenyt. "Pulsed Doppler: determination of blood velocity and volume flow in normal and diseased common carotid arteries in man". *Cardiovascular Research*, Vol. 16, No. 4, pp. 220–224, April 1982.

[Fole 97] J. Foley, A. van Dam, S. Feiner, and J. Hughes. *Computer Graphics: Principle and Practice*. Addison Wesley, 1997.

[Ford 08] M. Ford, S. Lee, S. Lownie, D. Holdsworth, and D. Steinman. "On the effect of parent-aneurysm angle on flow patterns in basilartip aneurysms: Towards a surrogate geometric marker of intra-aneurismal hemodynamics". *Journal of Biomechanics*, Vol. 41, No. 2, pp. 241–248, January 2008.

[Fran 08] D. Franchi, P. Gallo, and G. Placidi. "A Novel Segmentation Algorithm for Digital Subtraction Angiography Images: First Experimental Results". In: G. B. et. al., Ed., *Lecture Notes in Computer Science, Advances in Visual Computing*, pp. 612–623, 2008.

[Fran 09] D. Franchi, P. Gallo, L. Marsili, and G. Placidi. "A shape-based segmentation algorithm for X-ray digital subtraction angiography images". *Computer Methods and Programs in Biomedicine*, Vol. 94, No. 3, pp. 267–278, June 2009.

[Fran 98] A. Frangi, W. Niessen, K. Vincken, and M. Viergever. "Multiscale Vessel Enhancement Filtering". In: *Proceedings of the first international conference on Medical image computing and computer-assisted intervention*, pp. 130–137, Springer-Verlag, Berlin, Heidelberg, 1998.

[Fran 99] A. Frangi, W. Niessen, R. Hoogeveen, T. van Walsum, and M. Viergever. "Model-based quantitation of 3-D magnetic resonance angiographic images". *IEEE Transactions on Medical Imaging*, Vol. 18, No. 10, pp. 946–956, October 1999.

[Gan 05] R. Gan, W. Wong, and A. Chung. "Statistical cerebrovacular segmentation in three-dimensional rotational angiography based on maximum intensity projections". *Medical Physics*, Vol. 32, No. 9, pp. 3017–3028, September 2005.

[Gano 01] W. F. Ganong. *Review of Medical Physiology*. McGraw-Hill Publishing Co, March 2001.

[Gari 00] R. Garimella and M. Shephard. "Boundary layer mesh generation for viscous flow simulation". *International Journal of Numerical Methods in Engineering*, Vol. 49, No. 2, pp. 193–218, September 2000.

[Geer 09] A. Geers, I. Larrabide, A. Radaelli, H. Bogunovic, H. G. van Andel, C. Majoie, and A. Frangi. "Reproducibility of image-based computational hemodynamics in intracranial aneurysms: Comparison of CTA AND 3DRA". In: *IEEE International Symposium on Biomedical Imaging: From Nano to Macro*, pp. 610–613, Boston, MA, USA, July 2009.

[Geer 11] A. Geers, I. Larrabide, A. Radaelli, H. Bogunovic, M. Kim, H. G. van Andel, C. Majoie, E. van Bavel, and A. Frangi. "Patient-Specific Computational Hemodynamics of Intracranial Aneurysms from 3D Rotational Angiography and CT Angiography: An In Vivo Reproducibility Study". *American Journal of Neuroradiology*, Vol. 32, No. 3, p. 581, March 2011.

[Goet 06] J. Goetz. "Simulation of bloodflow in aneurysms using the Lattice Boltzmann method and an adapted data structure". Tech. Rep., Friedrich-Alexander Universität Erlangen-Nürnberg, Department Informatik, Lehrstuhl für Informatik 10 (Systemsimulation), 2006.

[Gong 03] R. Gong, S. Wörz, and K. Rohr. "Segmentation of Coronary Arteries of the Human Heart from 3D Medical Images". In: T. Wittenberg, P. Hastreiter, U. Hoppe, H. Handels, A. Horsch, and H.-P. Meinzer, Eds., *Bildverarbeitung fuer die Medizin*, pp. 66–70, Springer-Verlag, Berlin Heidelberg, March 2003.

[Grod 01] C. Groden, J. Laudan, S. Gatchell, and H. Zeumer. "Three-Dimensional Pulsatile Flow Simulation Before and After Endovascular Coil Embolization of a Terminal Cerebral Aneurysm". *Journal of Cerebral Blood Flow & Metabolism*, Vol. 21, No. 12, pp. 1464–1471, December 2001.

[Groh 07] M. Groher, F. Bender, R.-T. Hoffmann, and N. Navab. "Segmentation-driven 2D-3D registration for abdominal catheter interventions". In: *Proceedings of the 10th international conference on Medical image computing and computer-assisted intervention*, pp. 527–535, Springer-Verlag, Berlin, Heidelberg, 2007.

[Guel 08] M. Guelsuen and H. Tek. "Robust Vessel Tree Modeling". In: *Proceedings of the 11th international conference on Medical Image Computing and Computer-Assisted Intervention - Part I*, pp. 602–611, Springer-Verlag, Berlin, Heidelberg, 2008.

[Hall 09] M. Hall, E. Frank, G. Holmes, B. Pfahringer, P. Reutemann, and I. Witten. "The WEKA Data Mining Software: An Update". *SIGKDD Explorations*, Vol. 11, No. 1, pp. 10–18, July 2009.

[Hass 04] T. Hassan, M. Ezura, E. Timofeev, T. Tominaga, T. Saito, A. Takahashi, K. Takayama, and T. Yoshimoto. "Computational Simulation of Therapeutic Parent Artery Occlusion to Treat Giant Vertebrobasilar Aneurysm". *American Journal of Neuroradiology*, Vol. 25, No. 1, pp. 63–68, January 2004.

[Hent 09] C. Hentschke and K.-D. Toennies. "Intensity-based Registration of 2D-DSA and 3D-DSA Data Sets for Flow Simulation in Intracranial Aneurysms". In: *Proc. of Vision, Modeling, and Visualization (VMV)*, pp. 375–376, Braunschweig, November 2009.

[Hent 10] C. Hentschke and K.-D. Toennies. "Automatic 2D/3D-Registration of Cerebral DSA Data Sets". In: T. Deserno, H. Handels, H. Meinzer, and T. Tolxdorff, Eds., *Bildverarbeitung fuer die Medizin*, pp. 162–166, Springer-Verlag, Berlin, Heidelberg, March 2010.

[Hera 06a] N. Heran, J. Song, K. Namba, W. Smith, Y. Niimi, and A. Berenstein. "The Utility of DynaCT in Neuroendovascular Procedures". *American Journal of Neuroradiology*, Vol. 27, No. 2, pp. 330–332, February 2006.

[Hera 06b] N. Heran, J. Song, K. Namba, W. Smith, Y. Niimi, and A. Berenstein. "The Utility of DynaCT in Neuroendovascular Procedures". *American Journal of Neuroradiology*, Vol. 27, No. 2, pp. 330–332, February 2006.

[Hern 06] M. Hernandez-Hoyos, P. Ortowski, and M. Orkisz. "Vascular centerline extraction in 3D MR angiograms for phase contrast MRI blood flow measurement". *International Journal of Computer Assisted Radiology and Surgery*, Vol. 1, No. 1, pp. 51–61, March 2006.

[Hern 07] M. Hernandez and A. Frangi. "Non-parametric geodesic active regions: Method and evaluation for cerebral aneurysms segmentation in 3DRA and CTA". *Medical Image Analysis*, Vol. 11, No. 3, pp. 224–241, June 2007.

[Hipw 03] J. H. Hipwell, G. P. Penney, R. A. McLaughlin, K. Rhode, P. Summers, T. C. Cox, J. V. Byrne, J. A. Noble, and D. J. Hawkes. "Intensity-Based 2-D-3D Registration of Cerebral Angiograms". *IEEE Transactions on Medical Imaging*, Vol. 22, No. 11, pp. 1417–1426, November 2003.

[Hoi 04] Y. Hoi, H. Meng, S. Woodward, B. Bendok, R. Hanel, L. Guterman, and L. Hopkins. "Effects of arterial geometry on aneurysm growth: three-dimensional computational fluid dynamics study". *Journal of Neurosurgery*, Vol. 101, No. 4, pp. 676–681, October 2004.

[Hoi 06] Y. Hoi, S. Woodward, M. Kim, D. Taulbee, and H. Meng. "Validation of CFD Simulations of Cerebral Aneurysms With Implication of Geometric Variations". *Journal of Biomechanical Engineering*, Vol. 128, No. 6, pp. 844–851, December 2006.

[Hopp 07] S. Hoppe, F. Noo, F. Dennerlein, G. Lauritsch, and J. Hornegger. "Geometric calibration of the circle-plus-arc trajectory". *Physics in Medicine and Biology*, Vol. 52, No. 23, pp. 6943–6960, December 2007.

[Hopp 09] S. Hoppe. *Accurate Cone-Beam Image Reconstruction in C-Arm Computed Tomography*. PhD thesis, Friedrich-Alexander-Universität Erlangen-Nürnberg, Technische Fakultät, 2009.

[Huan 08] Z.-K. Huang and K.-W. Chau. "A New Image Thresholding Method Based on Gaussian Mixture Model". *Applied Mathematics and Computation*, Vol. 205, No. 2, pp. 899–907, November 2008.

[Jaeh 11] B. Jaehne. *Digital Image Processing*. Springer-Verlag, 2011.

[Jou 08] L. Jou, D. Lee, H. Morsi, and M. Mawad. "Wall Shear Stress on Ruptured and Unruptured Intracranial Aneurysms at the Internal Carotid Artery". *American Journal of Neuroradiology*, Vol. 29, No. 9, pp. 1761–1767, October 2008.

[Kak 88] A. Kak and M. Slaney. *Principles of Computerized Tomographic Imaging*. IEEE Press, 1988.

[Kale 06] W. A. Kalender. *Computertomographie. Grundlagen, Gerätetechnologie, Bildqualität*. Publicis Corporate Publishing, 2006.

[Kang 09] D. Kang, D. Suh, and J. Ra. "Three-Dimensional Blood Vessel Quantification via Centerline Deformation". *IEEE Transactions on Medical Imaging*, Vol. 28, No. 3, pp. 405–414, March 2009.

[Karm 04] C. Karmonik, A. Arat, G. Benndorf, S. Akpek, R. Klucznik, M. Mawad, and C. Strother. "A Technique for Improved Quantitative Characterization of IntracranialAneurysms". *American Journal of Neuroradiology*, Vol. 25, No. 7, pp. 1158–1161, August 2004.

[Karm 08] C. Karmonik, R. Klucznik, and G. Benndorf. "Blood flow in cerebral aneurysms: comparison of phase contrast magnetic resonance and computational fluid dynamics–preliminary experience". *RöFo*, Vol. 180, No. 3, pp. 209–215, March 2008.

[Kato 02] T. Kato, T. Indo, E. Yoshida, Y. Iwasaki, M. Sone, and G. Sobue. "Contrast-Enhanced 2D Cine Phase MR Angiography for Measurement of Basilar Artery Blood Flow in Posterior Circulation Ischemia". *American Journal of Neuroradiology*, Vol. 23, No. 8, pp. 1346–1351, September 2002.

[Kirb 04] C. Kirbas and F. Quek. "A Review of Vessel Extraction Techniques and Algorithms". *ACM Computing Surveys*, Vol. 36, No. 2, pp. 81–121, June 2004.

[Kopp 95] R. Koppe, E. Klotz, and J. O. de Beek. "Three-dimensional vessel reconstruction based on rotational angiography". In: *Proceedings of the International Symposium on Computer Assisted Radiology*, pp. 101–107, Springer-Verlag, June 1995.

[Krug 78] R. A. Kruger, C. A. Mistretta, J. Lancester, T. L. Houk, M. Goodsitt, C. G. Shaw, S. J. Riederer, J. Hicks, J. Sackett, A. B. Crummy, and D. Flemming. "A Digital Video Image Processer for Real-Time X-Ray Subtraction Imaging". *Optical Engineering*, Vol. 17, No. 6, pp. 652–657, 1978.

[Law 00] T. Law and P. Heng. "Automatic Centerline Extraction for 3D Virtual Bronchoscopy". In: *Proceedings of the Third International Conference on Medical Image Computing and Computer-Assisted Intervention*, Springer-Verlag, London, UK, 2000.

[Law 07] M. Law and A. Chung. "Vessel and intracranial aneurysm segmentation using multi-range filters and local variances". In: *Proceedings of the 10th international conference on Medical image computing and computer-assisted intervention - Volume Part I*, pp. 866–874, Springer-Verlag, Berlin, Heidelberg, 2007.

[Lee 94] T. Lee, R. Kashyap, and C. Chu. "Building skeleton models via 3-D medial surface/axis thinning algorithms". *Computer Vision, Graphics, and Image Processing*, Vol. 56, No. 6, pp. 462–478, November 1994.

[Lesa 09] D. Lesage, E. Angelini, I. Bloch, and G. Funka-Lea. "A review of 3D vessel lumen segmentation techniques: Models, features and extraction schemes". *Medical Image Analysis*, Vol. 13, No. 6, pp. 819–845, December 2009.

[Li 07] H. Li and A. Yezzi. "Vessels as 4-D Curves: Global Minimal 4-D Paths to Extract 3-D Tubular Surfaces and Centerlines". *IEEE Transactions on Medical Imaging*, Vol. 26, No. 9, pp. 1213–1223, September 2007.

[Loeh 00] R. Loehner and J. Cebral. "Generation of non-isotropic unstructured grids via directional enrichment". *International Journal of Numerical Methods in Engineering*, Vol. 49, No. 2, pp. 219–232, September 2000.

[Lore 87] W. E. Lorensen and H. Cline. "Marching Cubes: A high Resolution 3D Surface Construction Algorithm". *Computer Graphics*, Vol. 21, No. 4, pp. 163–169, July 1987.

[Lu 06] D. Lu, E. Bai, J. Liu, H. Yu, Y. Wei, Z. Cai, M. Sharafuddin, J. Golzarian, A. Stolpen, O. Saba, M. Vannier, and G. Wang. "Projection-based bolus detection for computed tomographic angiography". *Computer Assisted Tomography*, Vol. 30, No. 5, pp. 846–849, October 2006.

[Lu 09] B. Lu, W. Wang, and J. Li. "Searching for a mesh-independent subgrid model for CFD simulation of gasŰsolid riser flows". *Chemical Engineering Science*, Vol. 64, No. 15, pp. 3437–3447, August 2009.

[Luon 09] N. Luon, M. Yusoff, and N. Shuaib. "Tetrahedral Mesh Generator For CFD Simulation of Complex Geometry". In: *Proceedings of 3rd International Conference on Energy and Environment*, pp. 330–336, IEEE Computer Society, Malacca, Malaysia, December 2009.

[Meij 99a] E. H. W. Meijering, W. J. Niessen, and M. A. Viergever. "Retrospective Motion Correction in Digital Subtraction Angiography: A Review". *IEEE Transactions on Medical Imaging*, Vol. 18, No. 1, pp. 2–21, January 1999.

[Meij 99b] E. H. W. Meijering, K. J. Zuiderveld, and M. A. Viergever. "Image Registration for Digital Subtraction Angiography". *International Journal of Computer Vision*, Vol. 31, No. 2–3, pp. 227–246, April 1999.

[Nade 04] A. Nader-Sepahi, M. Casimiro, J. Sen, and N. Kitchen. "Is aspect ratio a reliable predictor of intracranial aneurysm rupture?". *Neurosurgery*, Vol. 54, No. 6, pp. 1343–1347, June 2004.

[Oaks 00] W. Oaks and S. Paoletti. "Polyhedral Mesh Generation". In: *Proceedings ot the 9 th International Meshing RoundTable*, pp. 57–66, 2000.

[Olab 03] S. Olabarriaga, M. Breeuwer, and W. Niessen. "Minimum Cost Path Algorithm for Coronary Artery Central Axis Tracking in CT Images". In: *Proceedings of the 6th international conference on Medical image computing and computer-assisted intervention: Part I*, pp. 687–694, Springer-Verlag, Berlin, Heidelberg, 2003.

[Osbo 99] A. G. Osborn. *Diagnostic Cerebral Angiography*. Lippincott Williams & Wilkins, 2 Ed., January 1999.

[Peke 09] A. Peker, E. Uestuener, E. Oezkavukcu, and T. Sancak. "Performance analysis of 8-channel MDCT angiography in detection, localization, and sizing of intracranial aneurysms identified on DSA". *Neuroradiology*, Vol. 15, No. 2, pp. 81–85, June 2009.

[Penn 98] G. Penney, J. Weese, J. Little, P. Desmedt, D. Hill, and D. Hawkes. "A Comparison of Similarity Measures for Use in 2-D-3-D Medical Image Registration". *IEEE Transactions on Medical Imaging*, Vol. 17, No. 4, pp. 586–595, August 1998.

[Peri 04] M. Peric. "Flow simulation using control volumes of arbitrary polyhedral shape". In: *ERCOFTAC Bulletin*, September 2004.

[Plan 35] B. G. Z. des Plantes. "Subtraktion. Eine Röntgenographische Methode zur Separaten Abbildung Bestimmter Teile des Objekts". *Fortschritte auf dem Gebiete der Röntgenstrahlen*, Vol. 52, pp. 69–79, 1935.

[Prak 01] S. Prakash and C. R. Ethier. "Requirements for Mesh Resolution in 3D Computational Hemodynamics". *Journal of Biomechanical Engineering*, Vol. 123, No. 2, pp. 134–144, April 2001.

[Ragh 05] M. Raghavan, B. Ma, and R. Harbaugh. "Quantified aneurysm shape and rupture risk". *Journal of Neurosurgery*, Vol. 102, No. 2, pp. 355–362, February 2005.

[Rohk 09] C. Rohkohl, G. Lauritsch, M. Prümmer, J. Boese, and J. Hornegger. "Towards 4-D Cardiac Reconstruction without ECG and Motion Periodicity using C-arm CT". In: B. M. W. E. Tsui, Ed., *Proceedings of 10th Fully 3D Meeting and 2nd HPIR Workshop*, pp. 323–326, September 2009.

[Rohk 10a] C. Rohkohl, G. Lauritsch, L. Biller, and J. Hornegger. "ECG-gated interventional cardiac reconstruction for non- periodic motion". In: *Proceedings of the 13th international conference on Medical image computing and computer-assisted intervention: Part I*, pp. 151–158, Springer-Verlag, Berlin, Heidelberg, 2010.

[Rohk 10b] C. Rohkohl, G. Lauritsch, L. Biller, M. Prümmer, J. Boese, and J. Hornegger. "Interventional 4D motion estimation and reconstruction of cardiac vasculature without motion periodicity assumption". *Medical Image Analysis*, Vol. 14, No. 5, pp. 687–694, October 2010.

[Roug 93] A. Rougée, C. Picard, C. Ponchut, and Y. Trousset. "Geometrical calibration of x-ray imaging chains for three-dimensional reconstruction". *Computerized Medical Imaging and Graphics*, Vol. 17, No. 4-5, pp. 295–300, July 1993.

[Sain 94] D. Saint-Felix, Y. Trousset, C. Picard, C. Ponchut, R. Romeas, and A. Rougee. "In vivo evaluation of a new system for 3D computerized angiography". *Physics in Medicine and Biology*, Vol. 39, No. 3, pp. 583–595, March 1994.

[Sang 07] N. Sang, H. Li, W. Peng, and T. Zhang. "Knowledge-based adaptive thresholding segmentation of digital subtraction angiography images". *Image Vision Computing*, Vol. 25, No. 8, pp. 1263–1270, August 2007.

[Schu 11a] D. Schuldhaus, M. Spiegel, T. Redel, M. Polyanskaya, T. Struffert, J. Hornegger, and A. Doerfler. "Classification-based Summation of Cerebral Digital Subtraction Angiography Series for Image Post-Processing Algorithms". *Physics in Medicine and Biology*, Vol. 56, No. 6, pp. 1791–1802, March 2011.

[Schu 11b] D. Schuldhaus, M. Spiegel, T. Redel, M. Polyanskaya, T. Struffert, J. Hornegger, and A. Doerfler. "2-D Vessel Segmentation Using Local Adaptive Contrast Enhancement". In: H. Handels, J. Ehrhardt, T. Deserno, H. Meinzer, and T. Tolxdorff, Eds., *Bildverarbeitung fuer die Medizin*, pp. 109–113, Springer-Verlag, Luebeck, March 2011.

[Seth 99] J. Sethian. *Level Set Methods and Fast Marching Methods: Evolving Interfaces in Computational Geometry, Fluid Mechanics, Computer Vision, and Materials Science*. Cambridge University Press, 1999.

[Sher 90] G. Sherouse, K. Novins, and E. Chaney. "Computation of digitally reconstructed radiographs for use in radiotherapy treatment design". *Int. J. Radiation Oncology Biology Physics*, Vol. 18, No. 3, pp. 651–658, March 1990.

[Shoj 04] M. Shojima, M. Oshima, K. Takagi, R. Torii, M. Hayakawa, K. Katada, A. Morita, and T. Kirino. "Magnitude and Role of Wall Shear Stress on Cerebral Aneurysm ComputationalFluid Dynamic Study of 20 Middle Cerebral Artery Aneurysms". *Stroke*, Vol. 35, No. 11, pp. 2500–2505, November 2004.

[Spie 09] M. Spiegel, M. Pfister, D. Hahn, V. Daum, J. Hornegger, T. Struffer, and A. Doerfler. "Towards Real-time Guidewire Detection and Tracking in the Field of Neuroradiology". In: M. Miga and K. H. Wong, Eds., *SPIE Medical Imaging, Visualization, Image-Guided Procedures, and Modeling*, pp. 7261055–1–7261055–8, 2009.

[Spie 10] M. Spiegel, D. Schuldhaus, and J. Hornegger. "DSA-Summation". Patent number 2010E09348DE/201016994, September 2010.

[Spie 11a] M. Spiegel, T. Redel, and J. Hornegger. "2D getriebene 3D Segmentierung". Patent number 2010E15514DE/201101660, March 2011.

[Spie 11b] M. Spiegel, T. Redel, T. Struffert, J. Hornegger, and A. Doerfler. "2-D Driven 3-D Vessel Segmentation Algorithm for 3-D Digital Subtraction Aniography Data". *Physics in Medicine and Biology*, Vol. –, pp. –, July 2011.

[Spie 11c] M. Spiegel, T. Redel, Y. Zhang, T. Struffert, J. Hornegger, R. Grossman, A. Doerfler, and C. Karmonik. "Tetrahedral vs. Polyhedral Mesh Size Evaluation on Flow Velocity and Wall Shear Stress for Cerebral Hemodynamic Simulation". *Computer Methods in Biomechanics and Biomedical Engineering*, Vol. 14, No. 1, pp. 9–22, January 2011.

[Stei 03] D. Steinman, J. Milner, C. Norley, S. Lownie, and D. Holdsworth. "Image-Based Computational Simulation of Flow Dynamics in a Giant Intracraniel Aneurysm". *American Journal of Neuroradiology*, Vol. 24, No. 4, pp. 559–566, April 2003.

[Stro 09] N. Strobel, O. Meissner, J. Boese, T. Brunner, B. Heigl, M. Hoheisel, G. Lauritsch, M. Nagel, M. Pfister, E.-R. Ruehrnschopf, B. Scholz, B. Schreiber, M. Spahn, M. Zellerhoff, and M. Klingenbeck-Regn. *Multislice CT*. Springer-Verlag, 2009.

[Stru 10] T. Struffert, V. Hertel, Y. Kyriakou, J. Krause, T. Engelhorn, B. Schick, H. Iro, J. Hornung, and A. Doerfler. "Imaging of cochlear implant electrode array with flat-detector CT and conventional multislice CT: comparison of image quality and radiation dose". *Acta Oto-Laryngologica*, Vol. 130, No. 4, pp. 443–452, April 2010.

[Stru 11] T. Struffert, Y. Deuerling-Zheng, S. Kloska, T. Engelhorn, J. Boese, M. Zellerhoff, S. Schwab, and A. Doerfler. "Cerebral blood volume imaging by flat detector computed tomography in comparison to conventional multislice perfusion CT". *European Radiology*, Vol. 21, No. 4, pp. 882–889, April 2011.

[Subr 04] N. Subramanian, T. Kesavadasa, and K. R. Hoffmann. "Geometry-based metrics for planning of neuroendovascular therapy". In: *Proceedings of the 18th International Congress and Exhibition CARS - Computer Assisted Radiology and Surgery*, pp. 718–723, June 2004.

[Sun 10a] Q. Sun, A. Groth, M. Bertram, I. Waechter, T. Bruijns, R. Hermans, and T. Aach. "Phantom-based experimental validation of computational fluid dynamics simulations on cerebral aneurysms". *Medical Physics*, Vol. 37, No. 9, pp. 5054–5065, September 2010.

[Sun 10b] Q. Sun, A. Groth, M. Bertram, I. Waechter, T. Bruijns, R. Hermans, V. M. Pereira, O. Brina, and T. Aach. "Experimental validation and sensitivity analysis for CFD simulations of cerebral aneurysms". In: *Proceedings of the 2010 IEEE international conference on Biomedical imaging: from nano to Macro*, pp. 1049–1052, IEEE Press, 2010.

[Tek 01] H. Tek, D. Comaniciu, and J. Williams. "Vessel detection by mean-shift based ray propagation". In: *IEEE Math. Meth. Biomed. Image Anal.*, p. 228, 2001.

[Tek 05] H. Tek, A. Ayvaci, and D. Comaniciu. "Multi-Scale Vessel Boundary Detection". In: *Computer Vision for Biomedical Image Applications*, pp. 388–398, 2005.

[Toma 98] C. Tomasi and R. Manduchi. "Bilateral Filtering for Gray and Color Images". In: *ICCV '98: Proceedings of the Sixth International Conference on Computer Vision*, pp. 839–846, IEEE Computer Society, Bombay, India, 1998.

[Tyrr 07] J. Tyrrell, E. di Tomaso, D. Fuja, R. Tong, K. Kozak, R. Jain, and B. Roysam. "Robust 3-D Modeling of Vasculature Imagery Using Superellipsoids". *IEEE Transactions on Medical Imaging*, Vol. 26, No. 2, pp. 223–237, February 2007.

[Udup 02] J. Udupa, P. Saha, and R. Lotufo. "Relative fuzzy connectedness and object definition: theory, algorithms, and applications in image segmentation". *IEEE Trans. Pattern Anal. Mach. Intell.*, Vol. 24, No. 11, pp. 1485–1500, November 2002.

[Ujii 01] H. Ujiie, Y. Tamano, K. Sasaki, and T. Hori. "Is the aspect ratio a reliable index for predicting the rupture of a saccular aneurysm?". *Neurosurgery*, Vol. 48, No. 3, pp. 495–502, March 2001.

[Vano 05] E. Vano, B. Geiger, A. Schreiner, C. Back, and J. Beissel. "Dynamic flat panel detector versus image intensifier in cardiac imaging: dose and image quality". *Physics in Medicine and Biology*, Vol. 50, No. 24, pp. 5731–5742, December 2005.

[Venu 06] P. Venugopal, H. Schmitt, G. Duckwiler, and D. Valentino. "Effects of segmentation on patient-specific numerical simulation of cerebral aneurysm hemodynamics". In: A. Manduca and A. Amini, Eds., *Medical Imaging: Physiology, Function, and Structure from Medical Images*,, 2006.

[Venu 07] P. Venugopal, D. Valentino, H. Schmitt, J. Villablanca, F. Vinuela, and G. Duckwiler. "Sensitivity of patient-specific numerical simulation of cerebral aneurysm hemodynamics to inflow boundary conditions". *Journal of Neurosurgery*, Vol. 106, No. 6, pp. 1051–1060, June 2007.

[Wank 02] I. Wanke, A. Doerfler, U. Dietrich, T. Egelhof, B. Schoch, D. Stolke, and M. Forsting. "Endovascular treatment of unruptured Intracranial aneurysms". *American Journal of Neuroradiology*, Vol. 23, No. 5, pp. 756–761, May 2002.

[Woer 07] S. Woerz and K. Rohr. "Segmentation and quantification of human vessels using a 3-d cylindrical intensity model". *IEEE Transactions on Image Processing*, Vol. 16, No. 8, pp. 1994–2004, August 2007.

[Wong 06] W. Wong and A. Chung. "Augmented vessels for quantitative analysis of vascular abnormalities and endovascular treatment planning". *IEEE Transactions on Medical Imaging*, Vol. 25, No. 6, pp. 665–684, June 2006.

[Wong 07] W. Wong and A. Chung. "Probabilistic vessel axis tracing and its application to vessel segmentation with stream surfaces and minimum cost path". *Medical Image Analysis*, Vol. 11, No. 6, pp. 567–587, December 2007.

[Wu 98] Z. Wu and J. Qian. "Real-time tracking of contrast bolus propagation in X-ray peripheral angiography". In: *Proceedings Workshop on Biomedical Image Analysis*, pp. 164–171, Santa Barbara, CA, June 1998.

[Yim 01] P. Yim, J. Cebral, R. Mullick, H. Marcos, and P. Choyke. "Vessel Surface Reconstruction With a Tubular Deformable Model". *IEEE Transactions on Medical Imaging*, Vol. 20, No. 12, pp. 1411–1421, December 2001.

[Yim 03] P. Yim, M. Kayton, W. Miller, S. Libutti, and P. Choyke. "Automated detection of blood vessels using dynamic programming". *Pattern Recognition Letters*, Vol. 24, No. 14, pp. 2471–2478, October 2003.

[Zell 05] M. Zellerhoff, B. Scholz, E.-P. Ruehrnschopf, and T. Brunner. "Low contrast 3D reconstruction from C-arm data". In: M. Flynn, Ed., *Proceedings of the SPIE Medical Imaging*, pp. 646–655, 2005.

Index